

Spring 2018

# Reduced Exhaust Emissions Through Blending n-Butanol with Ultra Low Sulfur Diesel and Synthetic Paraffinic Kerosene in Reactivity Controlled Compression Ignition Combustion

Remi Gaubert

Follow this and additional works at: <https://digitalcommons.georgiasouthern.edu/etd>

 Part of the [Automotive Engineering Commons](#), [Heat Transfer, Combustion Commons](#), and the [Thermodynamics Commons](#)

---

## Recommended Citation

Gaubert, Remi, "Reduced Exhaust Emissions Through Blending n-Butanol with Ultra Low Sulfur Diesel and Synthetic Paraffinic Kerosene in Reactivity Controlled Compression Ignition Combustion" (2018). *Electronic Theses and Dissertations*. 1761.  
<https://digitalcommons.georgiasouthern.edu/etd/1761>

This thesis (open access) is brought to you for free and open access by the Graduate Studies, Jack N. Averitt College of at Digital Commons@Georgia Southern. It has been accepted for inclusion in Electronic Theses and Dissertations by an authorized administrator of Digital Commons@Georgia Southern. For more information, please contact [digitalcommons@georgiasouthern.edu](mailto:digitalcommons@georgiasouthern.edu).

REDUCED EXHAUST EMISSIONS THROUGH BLENDING N-BUTANOL  
WITH ULTRA LOW SULFUR DIESEL AND SYNTHETIC PARAFFINIC KEROSENE  
IN REACTIVITY CONTROLLED COMPRESSION IGNITION COMBUSTION

by

REMI GAUBERT

(Under the Direction of Valentin Sologuie)

ABSTRACT

Increasing restrictions on the emitted exhaust emissions in diesel engines are becoming a more challenging task than in previous years. An electronic common rail fuel injection system and a port fuel injection (PFI) system were developed for an experimental engine to research dual fuel combustion. The experimental research was conducted at 1500 rpm and 4, 5, and 6 bar indicated mean effective pressure (IMEP). n-Butanol was port fuel injected at a 60% by mass fraction coupled with direct injection (DI) of three fuels, including ultra-low sulfur diesel (ULSD RCCI), a 50-50 wt-% blend of ULSD and butanol (ULSD-Bu RCCI), and a 50-50 wt-% blend of Fischer Tropsch synthetic paraffinic kerosene and butanol (S8-Bu RCCI). Split DI events of high reactivity fuels were used to maintain constant combustion phasing. The fuel blends increased pressure rise rates and ringing intensity drastically compared to conventional diesel combustion (CDC) and ULSD RCCI. Both butanol fuel blends had lower ignition quality than ULSD, increasing the mass fraction at the first DI event, increasing heat release rates up to 30%. ULSD-Bu RCCI had the shortest ignition delay and combustion duration due to the low cetane number. NO<sub>x</sub> and soot were simultaneously reduced up to 90% with RCCI compared to CDC. Unburned hydrocarbons were increased for RCCI fuel blends. S8-Bu RCCI resulted in reductions in hydrocarbon emissions compared to ULSD-Bu RCCI. Results display large emission reductions of harmful pollutants, such as NO<sub>x</sub> and soot, with RCCI combustion and the potential of alternative fuels in diesel combustion.

INDEX WORDS: Combustion, Common rail, Emissions, Diesel, Low temperature combustion, Fischer Tropsch, NO<sub>x</sub>, n-Butanol, Reactivity controlled compression ignition, Soot

REDUCED EXHAUST EMISSIONS THROUGH BLENDING N-BUTANOL  
WITH ULTRA LOW SULFUR DIESEL AND SYNTHETIC PARAFFINIC KEROSENE  
IN REACTIVITY CONTROLLED COMPRESSION IGNITION COMBUSTION

by

REMI GAUBERT

B.S., Georgia Southern University, 2016

A Thesis Submitted to the Graduate Faculty of Georgia Southern University

in Partial Fulfillment of the Requirements for the Degree

MASTER OF SCIENCE

STATESBORO, GEORGIA

© 2018

REMI GAUBERT

All Rights Reserved

REDUCED EXHAUST EMISSIONS THROUGH BLENDING N-BUTANOL  
WITH ULTRA LOW SULFUR DIESEL AND SYNTHETIC PARAFFINIC KEROSENE  
IN REACTIVITY CONTROLLED COMPRESSION IGNITION COMBUSTION

by

REMI GAUBERT

Major Professor: Valentin Soloiu  
Committee: Marcel Ilie  
Prakashbhai Bhoi

Electronic Version Approved:  
May 2018

## DEDICATION

To Mom, Papa, Ryan, Patricia, Madalena, Meme Janet, and Meme Carol.

In loving memory of Pepe Gus.

## ACKNOWLEDGMENTS

I would like to acknowledge Dr. Valentin Soloiu for his time and continuous support, my fellow graduate and undergraduate students working with me over the years, Ms. Brenda from the ME department, and the thesis committee for taking the time to review this work and provide additional support for the completion of this research. Without all of their help and support, this research would not be possible. I would also like to acknowledge the National Science Foundation under Grant No. 1609524 for funding needed for equipment and the Air Force Research Laboratory for the experimented fuel.

Sections of this thesis were produced around the work in Gaubert et al. (2017) and Gaubert et al. (2018).

## TABLE OF CONTENTS

|                                                                                               | Page |
|-----------------------------------------------------------------------------------------------|------|
| ACKNOWLEDGMENTS .....                                                                         | 3    |
| LIST OF TABLES .....                                                                          | 8    |
| LIST OF FIGURES .....                                                                         | 9    |
| LIST OF EQUATIONS .....                                                                       | 12   |
| ABBREVIATIONS .....                                                                           | 13   |
| CHAPTER 1 INTRODUCTION .....                                                                  | 17   |
| 1.1 The Beginning of Diesel Engines.....                                                      | 17   |
| 1.2 Modern Diesel Engines .....                                                               | 19   |
| 1.3 Diesel Exhaust Emissions and Aftertreatment Systems.....                                  | 20   |
| 1.5 Purpose of Study .....                                                                    | 24   |
| 1.6 Statement of Hypothesis.....                                                              | 24   |
| CHAPTER 2 LITERATURE REVIEW .....                                                             | 25   |
| 2.1 Low Temperature Combustion Modes.....                                                     | 25   |
| 2.2 Reactivity Controlled Compression Ignition .....                                          | 27   |
| 2.2.1 <i>In-Cylinder Reactivity and Concentration Stratification in RCCI Combustion</i> ..... | 29   |
| 2.3 Alternative Fuels .....                                                                   | 32   |
| 2.3.1 <i>Alcohol Based Fuels: n-Butanol</i> .....                                             | 33   |
| 2.3.2 <i>Fischer-Tropsch Fuels</i> .....                                                      | 36   |
| CHAPTER 3 METHODS .....                                                                       | 39   |
| 3.1 Overview .....                                                                            | 39   |



|                                                                       |    |
|-----------------------------------------------------------------------|----|
| 3.2 Development of the Common Rail Fuel Injection System .....        | 39 |
| 3.2.1 Hydraulic and Mechanical Subsystem Configuration .....          | 40 |
| 3.2.2 Electrical System Components and Sensor I/O .....               | 43 |
| 3.2.3 Rail Pressure Control Tuning .....                              | 44 |
| 3.2.4 Common Rail Fuel Injector Operation .....                       | 45 |
| 3.2.5 Fuel Injector Calibration .....                                 | 48 |
| 3.2.6 Signal Timing Verification .....                                | 49 |
| 3.2.7 Hardware-in-the-Loop Testing .....                              | 51 |
| 3.2.8 Engine Integration and Custom Fuel Injector Nozzle Design ..... | 54 |
| 3.3 Engine Specifications and Instrumentation .....                   | 57 |
| 3.4 Fuel Analysis .....                                               | 61 |
| 3.4.1 Parr 1341 Constant Volume Calorimeter .....                     | 61 |
| 3.4.2 Brookfield DV II Pro Rotational Viscometer .....                | 62 |
| 3.4.3 PAC CID510 CVCC .....                                           | 63 |
| 3.4.4 Shimadzu DTG-60 .....                                           | 64 |
| 3.4.5 Malvern Spraytec He-Ne laser .....                              | 65 |
| 3.5 Engine Operating Procedures .....                                 | 66 |
| 3.6 Measurement Uncertainty .....                                     | 68 |
| 3.7 Metrics for Success .....                                         | 69 |
| CHAPTER 4 ANALYSIS OF RESULTS .....                                   | 70 |

|                                                                                               |     |
|-----------------------------------------------------------------------------------------------|-----|
| 4.1 Fuel Analysis Characteristics .....                                                       | 70  |
| 4.1.1 Fuel Viscosity .....                                                                    | 71  |
| 4.1.2 Ignition Quality and Negative Temperature Coefficient .....                             | 72  |
| 4.1.3 Thermogravimetric and Differential Thermal Analysis .....                               | 73  |
| 4.1.4 MIE Scattering Spray Analysis .....                                                     | 76  |
| 4.2 Thermodynamic Combustion Analysis .....                                                   | 77  |
| 4.2.1 In-Cylinder Combustion Pressure .....                                                   | 79  |
| 4.2.2 Apparent Heat Release Rates .....                                                       | 81  |
| 4.2.3 Mass Fraction Burned .....                                                              | 84  |
| 4.2.4 Instantaneous Volume-Averaged Gas Temperature .....                                     | 86  |
| 4.2.5 Ringing Intensity .....                                                                 | 88  |
| 4.2.6 Heat Flux and Heat Losses .....                                                         | 89  |
| 4.3 Exhaust Emissions and Efficiencies .....                                                  | 93  |
| 4.3.1 Nitrogen Oxides and Soot .....                                                          | 93  |
| 4.3.2 Carbon Monoxide, Unburned Hydrocarbons, & Formaldehydes .....                           | 95  |
| 4.3.3 Engine Efficiencies .....                                                               | 97  |
| CHAPTER 5 CONCLUSION .....                                                                    | 100 |
| 5.1 Conclusion .....                                                                          | 100 |
| 5.2 Future Work .....                                                                         | 102 |
| Appendix A – 3D Model of the Experimental Engine with Common Rail fuel Injection System ..... | 112 |

|                                                                                            |     |
|--------------------------------------------------------------------------------------------|-----|
| Appendix B – Common Rail Fuel Injection Control Interface .....                            | 114 |
| Appendix C – User Interface of the Data Acquisition and Real-Time Monitoring Systems ..... | 118 |

## LIST OF TABLES

|                                                                                              |    |
|----------------------------------------------------------------------------------------------|----|
| Table I: Nonroad Compression Ignition Engines: Exhaust Emission Standards.....               | 20 |
| Table II: Bosch Piezoelectric Injector Operating Specifications .....                        | 48 |
| Table III: Flow Rate and Standard Deviation of Piezoelectric Injector Calibration Curve..... | 49 |
| Table IV: Flow Rate and Standard Deviation of Custom Nozzle Injector Calibration Curve ..... | 57 |
| Table V: Engine Specifications .....                                                         | 58 |
| Table VI: Design of Experiment for ULSD RCCI .....                                           | 67 |
| Table VII: Operating Parameters for CDC and RCCI.....                                        | 68 |
| Table VIII: Measurement Uncertainties .....                                                  | 68 |
| Table IX: Accuracy of Selected Sensor Measurements .....                                     | 69 |
| Table X: Selected Fuel Properties [**].....                                                  | 70 |
| Table XI: Characteristic Vaporization Temperatures .....                                     | 74 |
| Table XII: Particle Size Distribution by Volume ( $\mu\text{m}$ ) .....                      | 77 |
| Table XIII: Injection Duration (ms) and Mass Fraction of the First DI Event (%) .....        | 78 |
| Table XIV: Ignition Delay and Combustion Duration across Engine Loads .....                  | 86 |

## LIST OF FIGURES

|                                                                                                                           |    |
|---------------------------------------------------------------------------------------------------------------------------|----|
| Figure 1 Composition of Diesel Exhaust Gas (Majewski and Khair 2006) .....                                                | 21 |
| Figure 2 Emissions Regimes for Advanced Combustion Modes in T- $\Phi$ space (Neely et al. 2005)<br>.....                  | 25 |
| Figure 3 Reactivity Controlled Compression Ignition.....                                                                  | 27 |
| Figure 4 Verification and Validation Process of the Fuel Injection System (Gaubert et al. 2017)<br>.....                  | 40 |
| Figure 5 Schematic of the Hydraulic and Mechanical Subsystems (Gaubert et al. 2017).....                                  | 41 |
| Figure 6 Image of the Assembled Fuel Injection Test Bench.....                                                            | 42 |
| Figure 7 High Pressure Pump Schematic (Blocking and Wenzlawski 2016).....                                                 | 43 |
| Figure 8 Fuel Rail Pressure Control Feedback Loop (Gaubert et al. 2017) .....                                             | 44 |
| Figure 9 Tuned Rail Pressure Control (Gaubert et al. 2017) .....                                                          | 45 |
| Figure 10 Internal Function of a Piezoelectric Injector (Blocking and Wenzlawski 2016) .....                              | 47 |
| Figure 11 Piezoelectric Injector Calibration Curve (Gaubert et al. 2017).....                                             | 49 |
| Figure 12 Piezoelectric Injector Measurement Probe .....                                                                  | 50 |
| Figure 13 Injection Timing Validation (Gaubert et al. 2017).....                                                          | 51 |
| Figure 14 HIL Testing System Configuration (Gaubert et al. 2017).....                                                     | 52 |
| Figure 15 Constant Speed at Constant Load HIL Results (Gaubert et al. 2017) .....                                         | 53 |
| Figure 16 Transient Load at Constant Speed HIL Results (Gaubert et al. 2017) .....                                        | 53 |
| Figure 17 Fuel Injection System Wiring Schematic .....                                                                    | 54 |
| Figure 18 A 3-D Cross Section of a New Fuel Injector Adapted to the Original Cylinder Head<br>(Gaubert et al. 2017) ..... | 55 |
| Figure 19 Wall Wetting with the Piezoelectric Injector .....                                                              | 56 |

|                                                                                                                          |    |
|--------------------------------------------------------------------------------------------------------------------------|----|
| Figure 20 (Left) Original Injector Spray Pattern; (Right) Custom Injector Spray Pattern (Gaubert et al. 2017) .....      | 56 |
| Figure 21 Custom Nozzle Injector Calibration .....                                                                       | 57 |
| Figure 22 Experimental Engine Setup .....                                                                                | 60 |
| Figure 23 Image of the Engine Test Cell .....                                                                            | 60 |
| Figure 24 Image of the Fuel Flow Meters .....                                                                            | 61 |
| Figure 25 1341 Calorimeter Cross Section ( <i>1341 Plain Jacket Calorimeter Operating Instruction Manual 2014</i> )..... | 62 |
| Figure 26 Rotational Viscometer Schematic .....                                                                          | 63 |
| Figure 27 Constant Volume Combustion Chamber Design .....                                                                | 64 |
| Figure 28 DTG-60 Apparatus (Shimadzu Corporation 2012) .....                                                             | 65 |
| Figure 29 Malvern Mie Scattering Setup.....                                                                              | 66 |
| Figure 30 Dynamic Viscosity Measurements .....                                                                           | 71 |
| Figure 31 Pressure and Heat Release Rates in the CVCC .....                                                              | 72 |
| Figure 32 Negative Temperature Coefficient Region in the CVCC.....                                                       | 73 |
| Figure 33 Thermogravimetric Analysis .....                                                                               | 74 |
| Figure 34 Differential Thermal Analysis.....                                                                             | 75 |
| Figure 35 Sauter Mean Diameter and Droplet Frequency Distribution.....                                                   | 77 |
| Figure 36 Multi-Pulse Injection Pattern.....                                                                             | 78 |
| Figure 37 Global Equivalence Ratio before and after SOI-2.....                                                           | 79 |
| Figure 38 In-Cylinder Combustion Pressures.....                                                                          | 80 |
| Figure 39 In-Cylinder Combustion Pressures at 6 Bar IMEP.....                                                            | 80 |
| Figure 40 $dP/d\alpha$ at 6 Bar IMEP .....                                                                               | 81 |

|                                                                              |    |
|------------------------------------------------------------------------------|----|
| Figure 41 Apparent Heat Release Rates .....                                  | 83 |
| Figure 42 Apparent Heat Release Rates at 6 Bar IMEP .....                    | 84 |
| Figure 43 Mass Burned Across Engine Loads.....                               | 85 |
| Figure 44 Mass Burned at 6 Bar IMEP.....                                     | 86 |
| Figure 45 Instantaneous Volume-Averaged Gas Temperatures .....               | 87 |
| Figure 46 Instantaneous Volume-Averaged Gas Temperatures at 6 Bar IMEP ..... | 88 |
| Figure 47 Combustion Ringing Intensity.....                                  | 89 |
| Figure 48 Heat Flux at 6 Bar IMEP .....                                      | 91 |
| Figure 49 Heat Losses Based on Energy Balance .....                          | 92 |
| Figure 50 NO <sub>x</sub> Emissions across Engine Loads.....                 | 93 |
| Figure 51 Soot Emissions across Engine Loads .....                           | 94 |
| Figure 52 CO and UHC Emissions across Engine Loads .....                     | 96 |
| Figure 53 Formaldehyde Emissions across Engine Loads .....                   | 97 |
| Figure 54 Indicated Thermal and Mechanical Efficiency.....                   | 98 |
| Figure 55 Diesel Equivalent Brake Specific Fuel Consumption .....            | 99 |

## LIST OF EQUATIONS

|                  |    |
|------------------|----|
| Equation 1.....  | 44 |
| Equation 2.....  | 45 |
| Equation 3.....  | 45 |
| Equation 4.....  | 45 |
| Equation 5.....  | 62 |
| Equation 6.....  | 63 |
| Equation 7.....  | 63 |
| Equation 8.....  | 64 |
| Equation 9.....  | 68 |
| Equation 10..... | 82 |
| Equation 11..... | 88 |
| Equation 12..... | 90 |
| Equation 13..... | 90 |



## ABBREVIATIONS

|                 |                                                      |
|-----------------|------------------------------------------------------|
| A               | cylinder area                                        |
| AHRR            | apparent heat release rate                           |
| ATDC            | after top dead center                                |
| BSFC            | brake specific fuel consumption                      |
| BTDC            | before top dead center                               |
| BTL             | biomass-to-liquid                                    |
| CA10            | crank angle for 10% mass fraction burned             |
| CA50            | crank angle for 50% mass fraction burned             |
| CA90            | crank angle for 90% mass fraction burned             |
| CAD             | crank angle degree                                   |
| Cd              | combustion delay                                     |
| CD              | combustion duration                                  |
| CDC             | conventional diesel combustion                       |
| CI              | compression ignition                                 |
| CN              | cetane number                                        |
| CO              | carbon monoxide                                      |
| CO <sub>2</sub> | carbon dioxide                                       |
| COV             | coefficient of variation                             |
| CTL             | coal-to-liquid                                       |
| CVCC            | constant volume combustion chamber                   |
| d               | derivative term                                      |
| D               | cylinder diameter                                    |
| DCN             | derived cetane number                                |
| DI              | direct injection                                     |
| DID             | direction injection driver                           |
| DOC             | diesel oxidation catalyst                            |
| DPF             | diesel particulate filter                            |
| DTA             | differential thermal analysis                        |
| Dv(10)          | largest droplet size of 10% of the fuel spray volume |
| Dv(50)          | largest droplet size of 50% of the fuel spray volume |

|                 |                                                      |
|-----------------|------------------------------------------------------|
| Dv(90)          | largest droplet size of 90% of the fuel spray volume |
| e(t)            | control error                                        |
| EGR             | exhaust gas recirculation                            |
| EPA             | Environmental Protection Agency                      |
| FPGA            | field programmable gate array                        |
| F-T             | Fischer Tropsch                                      |
| GTL             | gas-to-liquid                                        |
| HCCI            | homogeneous charge compression ignition              |
| HCHO            | formaldehyde                                         |
| HPP             | high pressure pump                                   |
| i               | integral term                                        |
| IC              | internal combustion                                  |
| IMEP            | indicated mean effective pressure                    |
| IMV             | inlet metering valve                                 |
| ITE             | indicated thermal efficiency                         |
| K <sub>c</sub>  | proportional gain constant                           |
| L               | length of cylinder (viscometer)                      |
| LHV             | lower heating value                                  |
| LTC             | low temperature combustion                           |
| M               | motor torque (viscometer)                            |
| MPRR            | maximum pressure rise rate                           |
| NG              | natural gas                                          |
| NI              | National Instruments                                 |
| NMHC            | non methane hydrocarbons                             |
| NO <sub>x</sub> | nitrogen oxides                                      |
| NTC             | negative temperature coefficient                     |
| OEM             | original equipment manufacturer                      |
| p               | proportional term                                    |
| P               | combustion pressure                                  |
| PCCI            | premixed charge compression ignition                 |
| PFI             | port fuel injection                                  |

|              |                                                                             |
|--------------|-----------------------------------------------------------------------------|
| PM           | particulate matter                                                          |
| PV           | process variable                                                            |
| PWM          | pulse width modulation                                                      |
| Q            | heat release                                                                |
| R            | ideal gas constant                                                          |
| $R_c$        | container radius (viscometer)                                               |
| $R_s$        | spindle radius (viscometer)                                                 |
| RCCI         | reactivity controlled compression ignition                                  |
| Re           | Reynolds number                                                             |
| RI           | ringing intensity                                                           |
| rpm          | rotations per minute                                                        |
| SCR          | selective catalytic reduction                                               |
| SI           | spark ignition                                                              |
| SMD          | Sauter mean diameter                                                        |
| SOI-1        | start of the first injection                                                |
| SOI-2        | start of the second injection                                               |
| S8-Bu RCCI   | dual fuel combustion with 60% butanol PFI and 40% S8 and butanol blend DI   |
| $T_A$        | in-cylinder temperature                                                     |
| $T_d$        | derivative time constant                                                    |
| $T_i$        | integral time constant                                                      |
| $T_w$        | wall temperature                                                            |
| TA10         | temperature at which 10% of the fuel vaporized                              |
| TA50         | temperature at which 50% of the fuel vaporized                              |
| TA90         | temperature at which 90% of the fuel vaporized                              |
| TDC          | top dead center                                                             |
| TGA          | thermogravimetric analysis                                                  |
| $u_c$        | combined error                                                              |
| ULSD-Bu RCCI | dual fuel combustion with 60% butanol PFI and 40% ULSD and butanol blend DI |
| ULSD RCCI    | dual fuel combustion with 60% butanol PFI and 40% neat ULSD DI              |
| UHC          | unburned hydrocarbons                                                       |
| ULSD         | ultra-low sulfur diesel                                                     |

|               |                             |
|---------------|-----------------------------|
| $V$           | cylinder volume             |
| $x$           | calculation parameter       |
| $\beta$       | ringing intensity constant  |
| $\varepsilon$ | emissivity                  |
| $\gamma$      | specific heat of air        |
| $\lambda_A$   | thermal conductivity of air |
| $\sigma$      | Stefan-Boltzmann constant   |
| $\tau$        | shear stress                |
| $\dot{\tau}$  | shear rate                  |
| $q$           | heat flux                   |
| $\omega$      | angular velocity            |
| $\rho$        | gas density                 |
| $\theta$      | crank angle degree          |

## **CHAPTER 1 INTRODUCTION**

### **1.1 The Beginning of Diesel Engines**

Internal combustion (IC) engines were designed in the late 1800s to produce mechanical power from chemical energy in hydrocarbon based fuels for smaller, more efficient power generation units compared to the average steam engine (Norman 2016). Two engine design concepts that lead today's engine market are compression ignition (CI) and spark ignition (SI) engines because of their simplicity, ruggedness, and high power/weight ratios.

Successful developments of practical IC engines were introduced in the 1860s, beginning with J.J. E. Lenoir's (1822-1900), which burned coal-gas air mixtures. The first half of the piston stroke charged the cylinder with gas and air, where the spark then initiated a pressure rise to produce power during the second half of the stroke (Cummins 1976). These engines, however, only achieved 5% efficiency and were surpassed by Nicolaus A. Otto's (1832-1891) and Eugen Langen's (1833-1895) atmospheric engine design in 1867, reaching efficiencies of 11%. Otto and Langen's engine used the pressure rise in the inward stroke to accelerate a free piston and rack assembly, generating a vacuum in the cylinder with atmospheric air on the opposite side of the piston. The piston, connected to the output shaft, then moved outward due to the atmospheric pressure producing mechanical power. In 1876, Otto proposed the four-stroke Otto cycle: intake, compression, expansion or power, and exhaust; to overcome the low thermal efficiency and unnecessary weight and volume of its predecessor. These SI engine concepts were followed by Rudolf Diesel (1858-1913) in 1892, proposing a compression ignition concept in search for a safer (in terms of fuel storage) and more efficient engine. In CI engines, liquid fuel is introduced to the cylinder at high pressures and temperatures, which in turn, initiate combustion. These engines had double the efficiency, up to 30%, compared to earlier designs and were capable of producing more power (Heywood 1988). Otto and Diesel were credited for the invention of their engine concepts and designs; however, both faced challenges regarding patents, where others claimed that the ideas were influenced by previous work.

Rudolph Diesel was inspired by Carnot's theory of a perfectly efficient engine and his belief that the Otto cycle was an inefficient method due to the nearly equal mixture of air and fuel required. Diesel's original design proposed using nine times more air than fuel, which would absorb the heat generated by the burning fuel through the expanding combustion gases and result

in constant temperature combustion with a theoretical efficiency of 72%. It was soon found that this proposal would be unsuccessful, and he redrafted his design with reduced compression levels and eight times more fuel. The first production diesel engines were manufactured at Augsburg Engine Works from 1892 to 1897, where leaking valves and gaskets and the ability to vaporize fuel caused numerous problems and setbacks. After redesign of the combustion chamber and fueling system, the engine reached 30% efficiency and fuel consumption results that were half that of a gasoline engine (Norman 2016).

Worldwide interest in diesel engines grew after Diesel presented the first commercial 60 horsepower engine to the public in Munich, Germany. These engines were not introduced into the automotive industry at this time due to the size and auxiliary system requirements; however, they appeared in marine applications. The Danish ocean ship, *Seelandia*, was the first diesel-powered ship towing over 7000 tons and powered by two eight-cylinder, four-stroke engines with 1000 horsepower. Increased attention to the potential of diesel engines arose after its arrival to England and there was no smoke stack, such as a steam engine powered ship. *Seelandia* then continued to travel from England to Bangkok in 1912 (Norman 2016).

Interest continued to grow in diesel-power for warships and submarines, as World War I was about to erupt. Diesel engine fuel injection was improved significantly after the war. In the 1920s, solid fuel injection was developed, removing the need of an air compressor for fuel atomization, along with a new compact fuel injection pump designed by Bosch in Stuttgart, Germany. These advancements were followed by the introduction of diesel engines into the automotive market, starting with Daimler-Benz Company, releasing the first production diesel-powered model in 1936. Diesel engines were brought to the American market from General Motors (Detroit Diesel), Caterpillar, Allis-Chalmers, and Worthington by the late 1930s. The production of diesel engines in America began after Clessie Cummins, the founder of the Cummins Engine Company, modified the front end of a Packard automobile to fit a diesel marine engine and drove over 800 miles on \$1.38 of fuel. Cummins also drove the first diesel-powered vehicle in the Indianapolis 500, completing the race on one tank of fuel. The evolution of the diesel engine then grew through World War II, where these engines started to replace locomotive steam engines after the war. Steam powered locomotives were obsolete by the 1950s (Norman 2016).

## 1.2 Modern Diesel Engines

Progressions in technological advancements have evolved into conventional diesel engines that achieve 40% efficiency, where its spark ignition counterpart only reaches efficiencies around 25%. The higher efficiencies for diesel engines are attributed to the fueling system, fuel grade, higher compression ratios, and the robustness of the engine components. The disadvantages of diesel engines compared to gasoline engines include higher costs to build, due to the component characteristics that make them more durable, a lower range of engine speeds, requiring more gears, and the current challenge of meeting the increasingly strict emissions regulations on diesel engines. However, despite these drawbacks, diesel engines have a large presence in mobile and stationary applications including on and off-highway vehicles, generator sets, and marine and locomotive sectors (Norman 2016).

Emissions regulations are placed on CI engines due to the nature of the combustion process that converts chemical energy into mechanical power. In a “perfect” combustion, the reaction of hydrocarbon fuels with air produces products of only carbon dioxide ( $\text{CO}_2$ ), water ( $\text{H}_2\text{O}$ ), and nitrogen ( $\text{N}_2$ ). However, in reality there are incomplete combustion products that reduce engine efficiencies and are the source of pollutants that are harmful to the environment and mankind, creating widespread concern. Government regulated combustion emissions include carbon monoxide ( $\text{CO}$ ), unburned hydrocarbons (UHC), nitrogen oxides ( $\text{NO}_x$ ), and particulate matter (PM), where consistently stricter stipulations are placed causing increased challenges for diesel engines (Environmental Protection Agency 2016). The evolution of emissions regulations are described by DieselNet (1997).

To address government regulations on engine efficiencies and exhaust emissions, technological advancements in fuel injection, aftertreatment systems, and combustion chamber designs have been developed. Improvements in fuel injection systems are one of the most effective methods to minimize in-cylinder formation of exhaust emissions. Common rail (CR) fuel injection is the most widely accepted fueling system used in both diesel and gasoline engines. These systems are composed of a high pressure fuel rail accumulator distributing fuel to each injector, which is fed by a high pressure fuel pump. Benefits of CR systems have been acknowledged since the beginning of diesel engines, however it wasn't until 1997 when collaboration between Fiat Auto and Robert Bosch Company introduced the first electronic common rail fuel injection systems to

the market on the Alfa Romeo 156 (Buratti et al. 2004). CR systems implement a direct injection method, replacing indirect injection (IDI) systems, due to the improvements in fuel economy and increases in power density. Further developments have been aimed at reaching future emissions regulations, noise levels, and fuel consumption. This is achieved through the flexibility of controlling fuel pressure, independent of engine operating conditions, higher injection pressures for improved atomization, and the capability of multiple injection pulses per cycle for reduced noise and NO<sub>x</sub> emissions (Jääskeläinen and Khair 2015).

### 1.3 Diesel Exhaust Emissions and Aftertreatment Systems

The driving force for improvements in IC engines is the effect that exhaust emissions have on the environment. Environmental protection, climate change, and air pollution are subjects that have established many organizations such the Environmental Protection Agency (EPA), Organization for Economic Cooperation and Development (OECD), International Energy Agency (IEA), California Air Resources Board (CARB), and many more with the aim of preventing air pollution and climate change. It has been reported that emissions from the transportation sector emit 20-30% of total air pollution (Resitoğlu and Altinisik 2015). EPA regulations for nonroad compression-ignition engines in the rated power range of the experimental engine used for this thesis are provided in Table I below.

**Table I:** Nonroad Compression Ignition Engines: Exhaust Emission Standards  
(Environmental Protection Agency 2016)

| Rated Power (kW)           | Tier | Model Year | NMHC + NO <sub>x</sub> (g/kWh) | PM (g/kWh) | CO (g/kWh) |
|----------------------------|------|------------|--------------------------------|------------|------------|
| $8 \leq \text{kW} \leq 19$ | 1    | 2000-2004  | 9.5                            | 0.8        | 6.6        |
|                            | 2    | 2005-2007  | 7.5                            | 0.8        | 6.6        |
|                            | 4    | 2008+      | 7.5                            | 0.4        | 6.6        |

The approximate composition of diesel exhaust gasses is displayed in Figure 1. These concentrations are dependent on engine speed and load, where CO<sub>2</sub> and H<sub>2</sub>O increase with increasing engine loads due to increased fuel demand, decreasing the oxygen fraction of the mixture. Of these principle diesel exhaust emissions, CO<sub>2</sub> is the main concern due to its environmentally harmful effects, as it is a greenhouse gas. Approximately 1% of the exhaust gas composition contains pollutants that cause adverse health effects and environmental harm. Diesel



pollutant emissions are primarily composed of  $\text{NO}_x$  and PM, with about 50% being  $\text{NO}_x$ . Diesel combustion is a lean burn operation, meaning high air-fuel ratios, which minimizes HC and CO emissions in conventional combustion modes. Sulfur dioxide ( $\text{SO}_2$ ) is minimal with the introduction of ultra-low sulfur diesel (ULSD) (Majewski and Khair 2006).

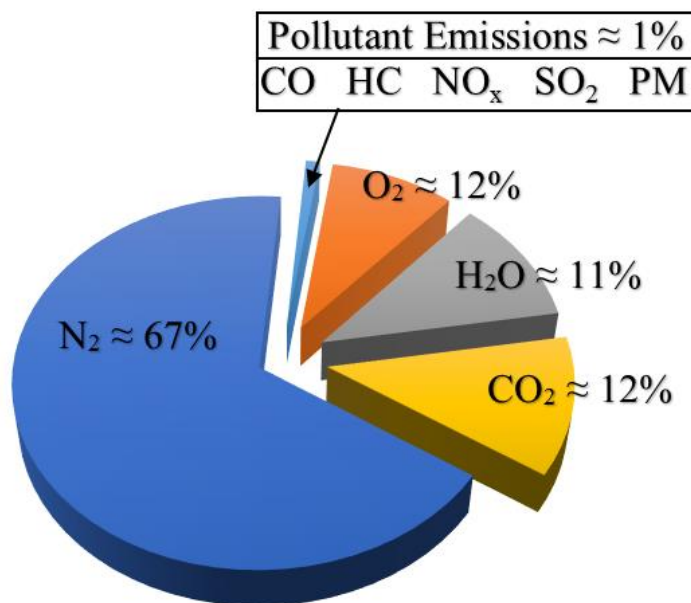


**Figure 1** Composition of Diesel Exhaust Gas (Majewski and Khair 2006)

Nitrogen oxides are composed of nitrogen oxide ( $\text{NO}$ ) and nitrogen dioxide ( $\text{NO}_2$ ), where  $\text{NO}$  is the dominant oxide pertaining to about 90% of the  $\text{NO}_x$  formation.  $\text{NO}$  formation occurs from the oxidation of both atmospheric and fuel nitrogen. Production of  $\text{NO}$  from atmospheric nitrogen is the primary source and is a temperature dependent reaction occurring at temperatures above  $1,600^\circ\text{C}$ , described by the Zeldovich mechanism (Resitoğlu and Altinisik 2015). The highest rates of  $\text{NO}_x$  from atmospheric nitrogen are produced near top dead center (TDC) where the flame temperature and cylinder pressure is highest.  $\text{NO}_x$  formation due to fuel nitrogen is a less understood reaction mechanism. This reaction is weakly dependent on temperature, is sensitive to the air-fuel ratio, and increases with increased air fractions. These pollutants are an environmental hazard due to their contribution to acid rain, ozone formation at the atmospheric level, and smog formation. Regarding living beings,  $\text{NO}_x$  emissions also cause adverse health effects, as they can cause irritations in the lungs, resulting in lung disease (Environmental Protection Agency 1999).

Diesel particulate matter is a carbonaceous material known as soot. PM mainly originates from incomplete combustion products of the hydrocarbon fuel and a small portion from the engine lubricating oil. The agglomeration of small particles produces spherules that are typically in the range of 15 to 30 nm (Heywood 1988). The formation process is dependent on many factors such as the combustion process, fuel quality, lubrication oil, combustion temperature, and exhaust gas cooling (Burtcher 2005). PM emissions range in size, where the smaller particulate matter is of greater concern, due to their 2.5 micrometer size and ability to enter deep into the lungs and the bloodstream. Larger PM are less damaging, however they can still irritate the eyes, nose, and throat. Exposure to PM has been found to cause premature death in people with heart and lung disease, nonfatal heart attacks, aggravated asthma, and respiratory problems. Environmental damage includes increases in acidity levels in lakes and streams, unbalanced nutrients in coastal waters, damaged forests and farm crops, and its contribution to acid rain (Environmental Protection Agency 2003).

Carbon monoxide is an incomplete combustion product that is primarily controlled by the air-fuel ratio. CO concentrations increase greatly in fuel rich combustion because there is an oxygen deficiency and all the carbon cannot be converted to CO<sub>2</sub>, making CO a concern in spark ignition engines. Diesel combustion is a lean operation, where CO is generally not a concern, however in dual fuel combustion modes, CO increases due its dependence on chemical kinetics. For diesel engines, the formation of CO emissions is a result of insufficient or too much turbulence inside the cylinder resulting in undermixing or overmixing of the air and fuel (Heywood 1988). The danger with CO emissions is that it is an odorless toxin that is emitted from burning any carbon based fuel. Inhaling low levels CO causes headaches, dizziness, vomiting, and nausea, but high levels of CO can cause one to become unconscious or be fatal. Long term effects of CO are not well known, however exposure to moderate levels of CO have been linked to increased risks for heart disease (Centers for Disease Control and Prevention 2017).

Unburned hydrocarbon emissions, or more specifically organic emissions, are another product of incomplete combustion, due to insufficient combustion temperatures surrounding the combustion chamber. The highest levels of UHC emissions occur at engine idling and light load operating conditions, at which point the air-fuel mixture is much leaner compared to full load conditions. The main sources of UHC emissions are due to overmixing (lean), undermixing (rich),

quenching, and misfire, with the overmixing lean path being the predominant cause (Heywood 1988). Diesel hydrocarbon emissions are composed of a wide range of molecular weights resulting in various levels of toxicity to the environment. Ingestion of these chemicals has damaging effects on the human body, causing problems regarding the nervous, respiratory, circulatory, and immune systems. UHC emissions emitted to the atmosphere also have a harmful influence on the formation of ground-level ozone layer (Resitoğlu and Altinisik 2015).

Extensive work in diesel exhaust aftertreatment systems for  $\text{NO}_x$  and PM reduction began in the 1990s after the Energy Policy Act of 1992, Section 2027. This Act authorized the Department of Energy to aid diesel engine manufacturers in the U.S. to meet the emissions standards without sacrificing diesels inherently high thermal efficiency (Ronald L. Graves 1999). Previously, improvements to engine design, fuel injection systems, and fuel properties were the focus, however, these were incapable of reducing emissions to the level of new regulations. Emission control systems eliminate the exhaust pollutants at the tail pipe, prior to being released into the atmosphere. Exhaust gas recirculation (EGR) is a common method for reducing  $\text{NO}_x$  emissions, but due to reallocating a portion of the fresh air with exhaust, efficiencies reduce and HC and CO emissions rise. Lean  $\text{NO}_x$  traps (LNT) have also been utilized, however are not efficient enough to meet the current regulations (Resitoğlu and Altinisik 2015).

Emission control systems that are effective at achieving the desired levels include diesel oxidation catalysts (DOC), diesel particulate filters (DPF), and selective catalytic reduction technology (SCR). DOCs are composed of honeycombs of ceramic or metal as a substrate for the aluminum oxide ( $\text{Al}_2\text{O}_3$ ) thermal coating, and precious metals as catalytically active centers. These devices are used for oxidizing HC and CO emissions into  $\text{H}_2\text{O}$  and  $\text{CO}_2$  and are placed upstream of the DPF and SCR, as it oxidizes NO to form  $\text{NO}_2$ . Increasing the  $\text{NO}_2$  concentration increases the efficiency of the other components. Controlling the exhaust temperature out of the DOC is also used as a catalytic heater to induce DPF regeneration from the increased temperatures of CO and HC oxidation. There are many materials used for particulate filtering such as ceramic monolithic filters, metal sintered filters, fiber-wound, fiber-knit, and fiber-woven filters. These DPF systems must overcome the challenges of high temperatures of  $1400^\circ\text{C}$  for regeneration, resistance to damage from lubricating oil, pressure losses induced, low-thermal mass, vibration resistant. Along

with the emission control challenge, these components must also have a small installation volume, a service life comparable to the engine, and cost effective (Scherm et al. (2016).

### **1.5 Purpose of Study**

Challenges for today's diesel engines arise from the difficulty to control the engine out emissions and adhere to Federal regulations. Dual fuel combustion modes have been developed to operate in low temperature combustion regimes, which is desirable for its inherent behavior to produce low NO<sub>x</sub> and soot. Depleting petroleum oil reserves has also created a second challenge regarding energy security. Alternative fuels produced from the Fischer Tropsch process have the potential to lessen this concern by deriving hydrocarbon fuels from non-petroleum sources, reducing the demand for petroleum oil. Bio-derived fuels, such as alcohols, are also of interest to address the matter. This research investigates compression ignition combustion in RCCI, coupling the alternative fuels: Fischer Tropsch S8 and bio-derived n-butanol, to understand the combustion characteristics that relate to low emission levels to potentially find a replacement for diesel fuel in the future.

### **1.6 Statement of Hypothesis**

If fuel reactivity gradients with two fuels of low and high reactivity, are created in-cylinder in a Tier 0 diesel engine, then the engine out emissions can meet EPA Tier 4 levels for medium duty off-road diesel engines using reactivity controlled compression ignition modes.

## CHAPTER 2 LITERATURE REVIEW

### 2.1 Low Temperature Combustion Modes

To address the packaging issues and the increased cost of engine production with exhaust aftertreatment systems, advanced combustion modes have been developed to reduce emissions formation directly in-cylinder. These strategies are characterized as low temperature combustion modes aiming to optimize the air-fuel mixture in-cylinder prior to the start of ignition by promoting leaner local in-cylinder regions. Common LTC strategies include homogeneous charge compression ignition (HCCI), premixed charge compression ignition (PCCI), and reactivity controlled compression ignition in the effort of simultaneously reducing emissions and increasing efficiencies. Compared to conventional diesel combustion (CDC), these combustion strategies aim to produce a homogeneous charge prior to ignition, where CDC ignites almost immediately after fuel injection, known as the premixed phase. Low temperature combustion modes are desirable for their potential to simultaneously reduce both  $\text{NO}_x$  and soot, while maintaining diesel efficiencies. However, LTC strategies have negative effects on pressure rise rate, stability, HC, and CO (Kokjohn et al. 2009). Neely et al. (2005) has illustrated the effect of local temperature (Kelvin) and equivalence ratio ( $\Phi$ ) on soot and  $\text{NO}_x$  emissions in the various combustion modes as displayed in Figure 2. The difficulties behind LTC are that they are typically limited to a narrow range of engine speed and load.

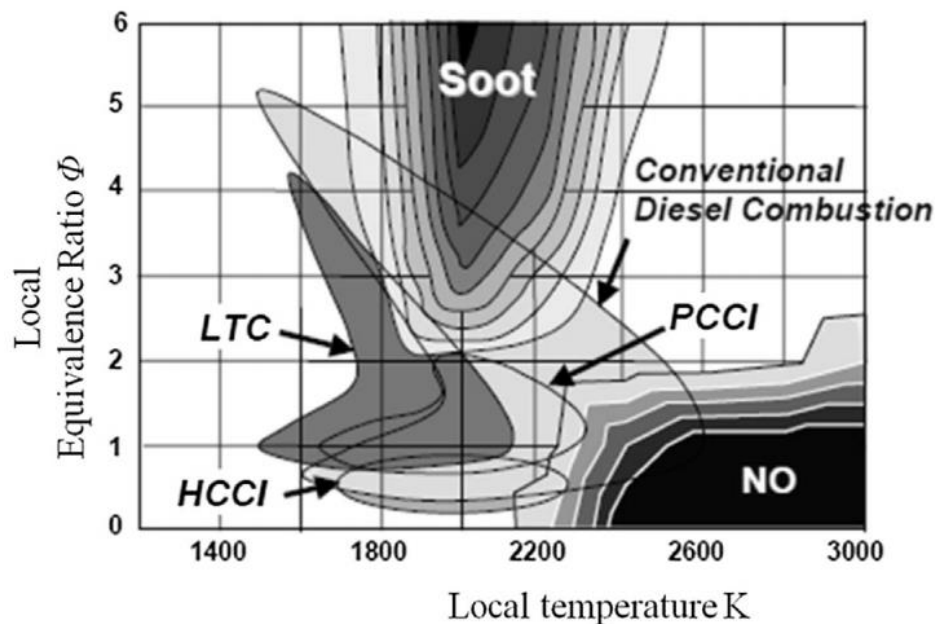


**Figure 2** Emissions Regimes for Advanced Combustion Modes in T- $\Phi$  space (Neely et al. 2005)

HCCI combustion is generally characterized as a method with early port fuel injection, while the inlet valve is open to induce a homogeneous air/fuel mixture. Without control of injection timing, stability and knock problems arise as load increases due to higher cylinder pressures and local equivalence ratios (Bression et al. 2008; Ekholm et al. 2008; Kokjohn et al. 2009). To minimize the corresponding high pressure rise rates, prolonged combustion durations or increased ignition delay is required through high rates of exhaust gas recirculation. The issue with very high EGR rates to control pressure rise rates and NO<sub>x</sub> emissions is that maintaining high relative air/fuel ratios ( $\lambda$ ) is difficult and pumping losses increase. As reported by Chadwell et al. (2011), high levels of EGR increase the demand from boosting systems to maintain volumetric flow rates in the intake, compromising the benefits of low temperature combustion.

PCCI is a direct injection strategy capable of the same emissions benefits as HCCI; however offers increased control of combustion phasing through optimizing injection timing. Compared to CDC, PCCI implements early low pressure injections resulting in longer injection durations for a more premixed charge, in which combustion starts after the end of injection. Difficulties with PCCI are higher levels of pressure rise rates and combustion noise compared to conventional diesel combustion, requiring high EGR rates in excess of 50% (Ming et al. 2015; Okude et al. 2004; Torregrosa et al. 2013) and can result in combustion efficiencies below 90% (Nieman et al. 2012).

Sjöberg et al. and Yang et al. investigated fuels with various ignition qualities in HCCI combustion and found that the overall fuel reactivity that governs equivalence ratio sensitivity and performance rather than the fuel composition. Optimized fuel blends for HCCI combustion increased the operable engine load range; however these results are dependent on environmental conditions (Splitter 2012). Inagaki et al. (2006) researched a dual fuel concept they called premixed compression ignition, in which two fuels were blended internally through two separate injection systems. Iso-octane was port fuel injected, simulating high octane gasoline, and diesel fuel was direct injected. Results extended the engine load range through reactivity stratification, rather than stratification of equivalence ratio, without EGR, preventing simultaneous ignition throughout the cylinder. Kokjohn et al. (2011) proposed this strategy as Reactivity Controlled Compression Ignition based on the concept of blending of two fuels with different reactivities. This method creates reactivity gradients throughout the combustion chamber, providing improved control over

combustion phasing by varying fuel ratios. Figure 3 illustrates the dual fuel strategy with two fuel injectors: a port fuel injector (left) introducing the low-reactivity fuel during the intake stroke and the direct injector (right) supplying the high reactivity fuel during the compression stroke.

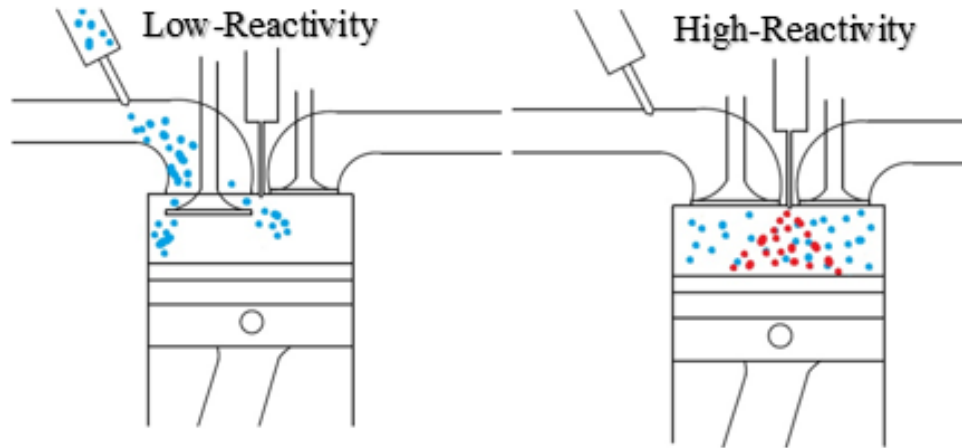


**Figure 3** Reactivity Controlled Compression Ignition

## 2.2 Reactivity Controlled Compression Ignition

In order to control combustion in RCCI mode, a double direct injection strategy must be implemented to create the reactivity gradients in-cylinder. An early injection is required between  $80^\circ$  and  $50^\circ$  before top dead center (BTDC) conditioning the squish region and a secondary injection as the ignition source, increasing local fuel/air ratios to a flammability point. Many studies on RCCI have been conducted with port fuel injection of low reactivity fuels such as gasoline, ethanol, methanol, and natural gas with diesel fuel as the high reactivity fuel.

Li et al. (2018) investigated both gasoline and methanol in RCCI mode to determine the influence of the different fuel properties. The engine was a 0.5L four-cylinder engine with a low pressure PFI system and high pressure solenoid common rail system. Optimization of injection strategy and the intake charge variables for both fuels were achieved based on Pareto Front cases at an engine load was run at 5 bar IMEP at 1500 rpm. The optimized cases resulted in NO<sub>x</sub> levels below the Euro VI standard, equivalent indicated specific fuel consumption (EISFC) below 190 g/kWh, and ringing intensity (RI) below 5 MW/m<sup>2</sup>. Both EISFC and RI were directly related to combustion phasing (CA<sub>50</sub>), with the most efficient location before  $4^\circ$  after top dead center (ATDC) for the gasoline/diesel case and after  $4^\circ$  ATDC for the methanol/diesel case. Later combustion phasing for methanol is due to the high rate of heat release as a result of the lower

ignition quality of methanol compared to gasoline, requiring the cooling effect of the expansion stroke. Both fuel cases were best with high intake temperatures.

Walker et al. (2013) studied fuel mixing of a common rail fuel injected 1.9L single-cylinder engine at swept SOI timings. Fuel injection timing was researched from 35° to 115° BTDC at injection pressures of 250 bar and 500 bar, and intake temperature of 45°C, and PFI ratio of 0.85. NO<sub>x</sub> emissions were below the US EPA 2010 On-Highway standard for all SOI at 500 bar injection pressure, however at 250 bar, the NO<sub>x</sub> limit was reached when injection timing was later than 55° BTDC due to near-stoichiometric diesel regions in the cylinder. Soot levels were all below regulated levels, however at the lower injection pressure and later injection timings, soot levels were highest, at which the cylinder density is relatively high, creating rich pockets of fuel. CO and UHC emissions were found to be lowest at later injection timings where ignition delay is shortest and heat release rates are more rapid.

RCCI research by Gross and Reitz (2017) investigated a 1.9L four-cylinder engine with port fuel injection of gasoline and direct injection of various diesel-gasoline blends. Two engine operating conditions were tested, including 1500 rpm. At this operating condition, brake efficiencies increased with reductions in fuel consumption for the dieseline mixtures compared to ULSD. This is attributed to the optimization of CA50 and best ratio between frictional losses and decreased heat transfer. Maximum pressure rise rates (MPRR) increased for the dieseline mixtures due to longer mixing times, however were maintained below 10 bar/deg. With low fractions of ULSD in the DI fuel, 20%, only a narrow range of PFI fraction was stable. A wider range of stable engine operation was found for higher ULSD ratios. UHC and CO emissions increased in RCCI, however slight reductions were found for the dieseline cases. NO<sub>x</sub> was also reduced in RCCI, and even further reduced with later combustion phasing. Dieseline cases increased NO<sub>x</sub> compared to ULSD as a result of increased heat transfer losses and higher combustion temperatures. This is the result of longer injection durations with the dieseline fuels due to the lower reactivity of gasoline.

Splitter et al. (2011) researched RCCI with DI of diesel and PFI of both gasoline and ethanol in a 2.44 L single-cylinder engine. Test cases for both fuels were at a load range from 5.6 to 14.5 bar IMEP with varying CA50 in order to retain the maximum pressure rise rate of 10 bar/deg and maximum pressure of 150 bar. Low temperature heat release was observed for both fuels, with diesel being the dominating factor. Combustion simulation results suggest that ethanol



inhibits the low temperature heat release compared to gasoline, however initiates high temperature heat release quickly as a result of shorter ignition delay and longer combustion duration. This trend is interesting because the diesel fuel mass for the ethanol cases is nearly twice that of the gasoline test cases. Across loads, both fuel RCCI cases maintained EPA 2010 Heavy Duty standards without aftertreatment systems. UHC and CO emissions and the coefficient of variation (COV) decrease as load is increased, insisting that the bulk gas temperature is the direct influence of this trend. Indicated thermal efficiencies reached 59% for the ethanol cases, which is higher than that for gasoline as a result of the reduced EGR requirements. This efficiency gain is attributed to the higher specific heat ratio of the intake charge with less EGR.

Dempsey et al. (2015) conducted RCCI research in a 1.9L four-cylinder engine with port fuel injected gasoline and direct injection of gasoline with varying percentages of cetane improver. The engine operating condition was run at 2300 rpm at 4.2 bar BMEP and found that regardless of the ignition quality of the fuel, combustion phasing was able to be controlled by varying the DI timing. This research claims that DI of diesel fuel will induce higher stratification compared to the gasoline blends due to the volatility differences, however combustion phasing in RCCI is determined by global parameters, and fuel stratification is a secondary effect. CA50 was also found to be more sensitive for the lower cetane fuels, in which the change in combustion phasing with varied DI timing is larger for the gasoline with the least cetane improver. NO<sub>x</sub> emissions were low across operating points, however with DI of gasoline, NO<sub>2</sub> emissions were constant across combustion phasing and NO decreased significantly.

### ***2.2.1 In-Cylinder Reactivity and Concentration Stratification in RCCI Combustion***

Reactivity gradients in RCCI were investigated at various operating conditions in a 0.5 L single-cylinder engine by Li et al. (2015) and validated through simulation. Two cases were compared including dual fueling with case A: PFI of gasoline and DI of diesel and case B: PFI and DI of the same gasoline-diesel blend. For case B, ignition delay and pressure rise rates were uncontrollable due to the absence of reactivity gradients. Pressure rise rates for case B reached 17 bar/deg and case A was controlled below 10 bar/deg. Both cases A and B operate under high peak pressures with acceptable levels of NO<sub>x</sub> as a result of reduced local temperatures from the homogeneous premixed fuel. From the simulations, case B exhibits higher local equivalence ratios

near the cylinder wall compared to case A, resulting in increased soot levels. Reductions in soot is also claimed to be a result of longer mixing time and less rapid heat release rates.

Nazemi and Shahbakhti (2016) modeled a 1.9 L four-cylinder engine for gasoline-diesel RCCI combustion to determine the controlling fuel injection parameters. The performance and emissions results were most strongly influenced by the spray angle of the direct injector. The base injector was at a  $74^\circ$  degree angle with respect to the injector axis and reduced down to  $25^\circ$ . Reductions in the spray angle increase peak pressures as a result of spray targeting on the hot piston bowl compared to the cooler squish regions. Heat release rates, however, decreased with narrower spray angles, in which the liquid jet would build up in the piston bowl and result in undermixing. With the less homogeneous mixture in-cylinder, increases in high temperature pockets were found, increasing NO<sub>x</sub> emissions. The disadvantage of wider spray angles were increases in peak pressure rise rates and ringing intensity. The start of injection (SOI) for the direct injected diesel was also studied, displaying a lower overall equivalence ratio and a slight reduction in peak pressures as SOI is delayed. Heat release was strongly affected by delaying SOI, due to the distribution of diesel fuel being the source of ignition. When the flame propagates from the cylinder liner, it is difficult to ignite the gasoline fuel exhibiting a weaker combustion. Small advancements of SOI compared to the base condition caused decreases in HC, CO, and soot levels, but increases in NO<sub>x</sub>. Further advancements resulted in lower UHC, CO, and soot, but higher NO<sub>x</sub> as a result of the increased cylinder gas temperatures. A large advancement in injection timing reduces the time for diesel to mix and reduces combustion temperatures. This causes increases in locally rich regions, NO<sub>x</sub>, and soot.

The effects of reactivity stratification and concentration stratification on RCCI combustion was researched in a 0.5L engine with n-butanol and diesel by Xiao et al. (2018). RCCI involves both reactivity and concentration stratification, however reactivity stratification is the predominant factor in RCCI. Xiao et al. (2018) found that in-cylinder reactivity and concentration stratification increases with lower PFI fractions and delayed SOI timing. At high butanol fractions (96.3%) and early SOI ( $50.6^\circ$  BTDC), combustion rates increase as a result of the homogeneous air/fuel distribution. This is advantageous because it reduces local temperatures at the cylinder walls, which lowers the heat transfer losses. This results in increased work output, however it also induces elevated pressure rise rates and ringing intensities. In order to reduce ringing intensities, increased

reactivity and concentration stratification can be achieved by lower PFI fractions or delayed SOI timing. For cases with lower butanol fractions (89.7%) and delayed SOI (47° BTDC), combustion was advanced as a result of the higher amount of high reactivity diesel. This increased local combustion temperatures, pressure rise rates, and ringing. To address the increased NO<sub>x</sub> emissions from more regions of locally rich diesel concentrations, elevated EGR rates can be used. By delaying SOI near TDC (14.1° BTDC) at high PFI fractions (96.5%), equivalence ratio stratification is increased at CA50, contributing to slow heat release rates, but NO<sub>x</sub> increases from the locally high temperatures. The high PFI fraction RCCI mode restricts load range due to the HCCI like combustion event. This is beneficial for fuel consumption and lower heat transfer losses, however if the PFI fraction is too high, incomplete combustion products and fuel consumption increase.

Fuel stratification was researched by Mikulski and Bekdemir (2017) with port fuel injected natural gas (NG) and direct injected diesel in a heavy duty RCCI engine. Simulations were conducted taking into account the knowledge that the majority of the direct injected fuel accumulates near the cylinder walls with decreasing concentrations near the center of the cylinder. At low loads (3.2 bar IMEP), significant improvements in combustion efficiency and overall indicated efficiencies were found with small fuel gradients. This result is due to the diesel fuel enriching the zones of the low reactivity natural gas, which promotes a more complete combustion with increased ignition delay and a shorter combustion duration. Longer ignition delay is caused by the lack of oxygen and lower local temperatures at the most reactive zones. Increased NG distribution also enhanced flame propagation towards the region below the direct injector tip, which is typically difficult. Increasing combustion efficiency through fuel stratification reaches a limit however, by over-rich zones at the cylinder liner. This is due to the lack of oxygen, which increases CO emissions. NO<sub>x</sub> emissions increase when there is a lack of fuel stratification because the rich zones combustion with high heat release rates, leading to higher local temperatures. The high heat release rates and high local temperatures are the main contributors for heat transfer losses. Mid load cases (6.9 bar IMEP) had similar trends to that of the low load cases. Compared to HCCI, NO<sub>x</sub> emissions are slightly reduced in RCCI with the fuel stratification. Rich zones are increased in RCCI inducing higher NO<sub>x</sub> production compared to a homogeneous mixture, however, the cold zones with fuel stratification is the compensating factor.

Tang et al. (2017) investigated reactivity controlled compression ignition in a 0.66L light-duty optical engine with varying levels of fuel stratification. This was achieved through changing the direct injection timing of n-heptane from 90° to 10° BTDC, and maintaining a constant port fuel injection timing for iso-octane. The engine was run at 1200 rpm and across loads. At higher loads, DI timing was delayed to reduce peak pressure rise rates, however this resulted in problems with soot levels. Under non-fired conditions (no direct injection), the fuel stratification levels were evaluated at the various DI timings. For the SOI case at 90° BTDC, the air/fuel mixture was well mixed with local equivalence ratios below 1.2. At the later DI timings, the fuel stratification was increased with a maximum equivalence ratio around 1.5. For firing conditions, the ignition kernel was consistently located in the fuel rich regions for all three RCCI cases. At early injection timings, combustion results are similar to that of HCCI. The positions of the soot radiating regions after TDC are at the same location as the fuel rich locations for all cases, however are much weaker than those for later injection timing. Images for RCCI showed that the reactivity progressively reduced from the combustion chamber wall to the center part of the combustion chamber. The high temperature heat release rate for RCCI also showed that the heat release could spread to the central parts of the combustion chamber, where unburned hydrocarbons are produced in conventional diesel combustion.

### **2.3 Alternative Fuels**

The combustion process has a wide range of application regarding passenger and commercial vehicles, electrical power generation, agriculture, etc. Gasoline and diesel are the primary fuels utilized in IC engines; however, the depletion rate of these fuels is faster than the rate at which they are naturally produced. This has created a search for alternative fuels, beginning in the 1980s (J.B. Hewood 1981). Although the petroleum source of gasoline and diesel is “renewable”, alternative fuels as defined by the Energy Policy Act (EPAAct), cover alcohols, natural gas and liquefied petroleum gas (LPG), propane, coal to liquid (CTL) fuels, hydrogen, biodiesel, and fuel that is substantially non-petroleum with the potential of securing energy security, while providing environmental benefits (U.S. Department of Energy). Along with energy security, increasing concern to reduce CO<sub>2</sub> emissions is a driving factor. Bio-derived fuels have the potential to form a CO<sub>2</sub> life cycle, mitigating the pollutant by emitting CO<sub>2</sub> through a useful energy conversion that would otherwise occur naturally.

In order for an alternative fuel to be considered as a viable replacement to petroleum derived gasoline and diesel, a few aspects must be considered. These include the fuels combustion properties such as octane and cetane, its physical properties, fuel system compatibility, energy density (or lower heating value), and manufacturing/infrastructure cost (Bae and Kim 2016). The chemical properties regarding its combustion characteristics determine whether the fuel is compatible with SI or CI engines for stable operation. A fuel must have high octane, or high resistance to auto ignition, for spark ignition engines and a high cetane, or high ignition qualities, due to the concept behind the combustion process of these engines. Physical properties, which also closely pertain to fuel system compatibility, consist of the viscosity, density, lubricity, oxidation stability, etc, which affect the ability of the fuel system to atomize and create a combustible mixture, and withstand corrosive properties. Lubricity is a common concern for alternative fuels, which cause high wear to mechanical components such as valves and pumps requiring additional additives. The lower heating value is important, as it is directly related to the fuels efficiency to convert chemical energy to mechanical energy. Manufacturing and infrastructure must also be considered, which has become less of a problem with technological advancements, easing the production of alternative fuels. Manufacturing and infrastructure are however dependent on region and market.

### ***2.3.1 Alcohol Based Fuels: n-Butanol***

Interest in alcohols as fuel has grown due to their environmental friendliness, local abundance, and ease of production. Alcohol based fuels are able to be produced from a range of renewable sources such as non-food crops and agricultural waste. Food processing produces large quantities of waste that contain high levels of nutrients, with the majority of these byproducts being discarded. Food processing waste (FPW) is separated into the desired and undesired byproducts, which are product specific, with little variances in quality. Both solid and liquid FPW are prospective sources for alcohol production, however they must be abundant and non-competing with human and animal food resources (Hedge et al. 2018). With a growing population, food production and waste is increasing, and raising concern regarding greenhouse gas emissions, the water footprint, land conversion, and economics. Food waste byproducts are rich with microbes such as carbohydrates and amino acids that can be fermented into different alcohols such as ethanol, butanol, and propanol.

Several physical and chemical properties of waste govern the production of alcohols such as its pH, chemical oxygen demand (COD), total solids, carbohydrates, proteins, lipids, and ash content. The pH must be controlled during fermentation because this property can change the shape or charge of a substrate, enabling or disabling the fermentation process (Worthington Biochemical Corporation 1972). COD is a quality index of the waste regarding the total organic compounds present. Higher COD values indicate higher nutritional value regarding alcohol production as this can increase the alcohol yield. Total solids measurement is the amount of solids in a waste product after being heated to 100°C, achieving a constant weight. High concentrations of solids serve as toxin carriers, which adhere to suspended particles. The ash content refers to the inorganic matter, which is important in the fermentation process, acting as a catalyst for alcohol production from enzymes.

Methanol ( $\text{CH}_3\text{OH}$ ) and ethanol ( $\text{C}_2\text{H}_5\text{OH}$ ) have been widely investigated for use in CI engines due to their local availability and clean burning characteristics. Methanol is derived from various sources of carbon including biomass, coke oven gas, syngas, coal, and natural gas. Ethanol is produced from lignocellulosic materials such as starch and corn feedstock, sugar cane residue, and waste and forestry biomass (Babu et al. 2017). Of the two, ethanol is the predominate biofuel because of the environmental advantage of ethanol production through renewable sources rather than petroleum.

Alcohol based fuels have gained acceptance in spark ignition engines; however, their fuel properties have potential to improve compression ignition combustion through dual fuel strategies as well. Alcohols are defined by their molecular structure, which contain a hydroxyl group ( $-\text{OH}$ ). The additional oxygen molecule is beneficial for increased soot oxidation. Fuels with low ignition quality, such as alcohols, are typically not suitable for CI engines, but when port fuel injected for RCCI or blended with diesel, combustion phasing can be delayed to increase mixing time for further reductions in soot. These fuels also have high volatility compared to diesel, increasing the homogeneity of the air/fuel mixture in-cylinder, where mixing does not occur until the fuel is in its vapor phase. Alcohols have a higher flash point and higher latent heat of vaporization properties compared to diesel. Higher flash points are beneficial for storage and transportation safety and high latent heats are useful for decreasing the combustion temperature due to the cooling effect, reducing  $\text{NO}_x$  formation in-cylinder. Disadvantages that arise from alcohols include lower energy

densities, increasing fuel consumption, poor miscibility with diesel, and poor lubricity properties (Bae and Kim 2016).

Butanol ( $C_4H_9OH$ ) is another alcohol that has gained interest for combustion researchers. There are several isomers of butanol including 1-butanol, 2-butanol, tert-butanol, and iso-butanol, creating either straight-chain or branched carbon structures. All of which, can be produced from fossil fuels, however, n-butanol is derived from biomass and assumes a straight-chain molecular structure. Butanol is a long chain alcohol (exceeding three carbon atoms) with a higher cetane number and energy density, is non-hygroscopic in nature, has better miscibility characteristics with diesel, and is less corrosive compared to methanol and ethanol. The volatility of butanol is also lower because of the additional carbon atoms. Lower volatility reduces the risk of cavitation problems and vapor lock, improving the fuels properties at extreme high and low temperatures. Less ignition problems are found with butanol because of the lower heat of vaporization and lower autoignition temperature, improving cold start and low load conditions. Butanol also has a higher viscosity than methanol and ethanol, with less risk of pump or valve failure. However, the disadvantage of biobutanol is that its yields are 10-30 times less than that for ethanol (Jin et al. 2011).

The majority of RCCI literature utilize gasoline, natural gas, methanol, and ethanol, however research conducted with n-butanol has been found to achieve reductions in  $NO_x$  and soot. Han et al. (2015) researched butanol-diesel RCCI in a 0.5L single-cylinder diesel engine at 1500 rpm and 8 bar IMEP. Late SOI timings were used from  $5^\circ$  BTDC to  $3^\circ$  ATDC, which delayed ignition timing and reduced peak pressure rise rates. A two stage heat release is exhibited with a low temperature heat release from the butanol prior to the diesel injection when n-Butanol was port fuel injected contributing to 40% of the total fuel energy. With increasing butanol levels however, the LTHR increases to be high temperature heat release, resulting in a long diffusion phase increasing soot levels.

Mohebbi et al. (2018) investigated RCCI with diesel-butanol blends (20% and 40% butanol) direct injected with port fuel injected gasoline in a 0.29L single cylinder engine. The study found that increasing the butanol fraction increased the premixed combustion phase and reduces the combustion duration considerably. With a constant combustion timing, SOI of the diesel-butanol blends was delayed compared to RCCI with neat ULSD, inducing higher local

equivalence ratios prior to combustion, which resulted in increased pressure rise rates and reduced combustion durations. From the increased pressures and apparent heat release rates for the butanol blends, it was deduced that the fuel's cetane number, latent heat of vaporization, and auto ignition temperature are the controlling factors regarding ignition delay in a direct injected engine.

### ***2.3.2 Fischer-Tropsch Fuels***

Fischer-Tropsch (F-T) diesel fuels are promising alternatives to traditional diesel with desirable properties that are based on their production process. The Fischer-Tropsch process is a method for producing synthetic liquid hydrocarbon fuel from coal (CTL), natural gas (GTL), or biomass (BTL). It was developed by Franz Fischer and Hans Tropsch in the 1920s during World War II, addressing the shortage of petroleum fuels with the abundant supplies of coal to aid the German war effort. The F-T diesel produced at this time was obtained by distillation of light hydrocarbons, without hydroprocessing, resulting in fuels that contained olefins and oxygenates. The diesel oil was sulfur free and had exceptionally high cetane numbers (between 90 and 100 CN), however, this was not considered reason enough to develop an engine to exploit these properties. Instead, the diesel oil was blended with coal tar to increase the cetane number from 10-15 to 40-50 (Dieter 2009).

Multiple plants have been commissioned utilizing Fischer Tropsch technology over the years beginning in 1934, when F-T technology became commercialized by the German chemical company Ruhrchemie AG, using coal as the syngas source in a low-temperature Fischer-Tropsch (LTFT) process. In the United States, the Carthage Hydrocol Fischer-Tropsch plant was established in the 1940-1950s, implementing an iron-based high temperature (HTFT) method. The first coal based Sasol F-T (Sasol 1) plant began in 1952 in Sasolburg, South Africa, after an international boycott, restricting the importation of petroleum fuels (Alleman and McCormick 2003). Sasol 1 was made up of four refineries; tar workup, HTFT oil workup, LTFT oil workup, and chemical workup. Over the years, this plant has progressed and has reverted from coal-to-liquid to gas-to-liquid products. Sasol opened a second HTFT plant (Sasol 2) in Secunda, South Africa after being pressed by the Organization of the Petroleum Exporting Countries (OPEC), which was formed in the 1970s during the oil crisis. At the time, oil prices were on the rise, and Sasol began the construction of a third site (Sasol 3), which was commissioned in 1983. Sasol iron-catalyzed HTFT opened in 1993 in Bintulu, Malaysia producing naphtha, kerosene, and



distillates. Sasol Oryx GTL plant was then commissioned in 2006 in Las Raffan, Qatar, using Sasol's proprietary cobalt catalyst-based LTFT technology (Dieter 2009).

F-T fuel properties are typically composed of very high cetane numbers ( $>74$ ), zero aromatics, and poor cold flow characteristics, or moderately high cetane numbers ( $\sim 60$ ), low aromatics ( $\leq 15\%$ ), and cold flow properties similar to that of diesel. The production process can be separated into three steps: the formation of synthesis gas (syngas), Fischer-Tropsch catalysis, and post-processing. There are multiple methods of forming syngas depending on the source. Syngas from natural gas can be produced through auto-thermal reforming, steam reforming, and partial oxidation, whereas the formation of syngas from coal or biomass is from the gasification of the feedstock with steam and oxygen to produce carbon monoxide, carbon dioxide, and hydrogen. Syngas is then converted into hydrocarbons from Fischer-Tropsch catalysis through either a low or high temperature reaction. High temperature reactions occur between  $300\text{--}350^\circ\text{C}$  with an iron-based catalyst, resulting in highly branched molecules of relatively low molecular weight. Either iron or cobalt based catalysts are used for low temperature reactions between  $200\text{--}240^\circ\text{C}$ . The high temperature process is generally more applicable to gasoline production, whereas the products of low temperature methods are more suitable for diesel fuels. Post processing is then performed through hydrocracking and hydrotreating to remove oxygenates, creating fuels with physical and chemical properties resembling those of petroleum diesel (Alleman and McCormick 2003).

Depending on the temperature, catalyst selection, and syngas production method used to produce F-T diesel fuels, the paraffinic content can be optimized to produce n-paraffins, iso-paraffins, and sometimes cyclo-paraffins (or naphthenes) in various distributions, which determines the cetane number of the fuel. Paraffins are major components of petroleum and natural gas, with properties that promote clean combustion in compression ignition engines. Diesel fuels contain paraffins, along with naphthenes and aromatics, which are not desirable due to their influence on carbon monoxide and particulate matter emissions. Fischer Tropsch diesel fuels are paraffinic in nature, where low temperature processes maximize paraffinic middle distillates, and high temperature processes result in different hydrocarbon mixtures. Specifications of paraffinic diesel fuels are based on the standard EN 15940:2016, containing at least 98.5% paraffins by

weight. Paraffinic content is controlled by limiting aromatics and olefins to near zero (International Energy Agency – Advanced Motor Fuels).

One common fuel property that both Fischer Tropsch and conventional diesel fuels have is the near zero sulfur content. Allowable sulfur content in conventional diesel has been continuously reduced due to the improvements in particulate matter emissions. For F-T fuels, sulfur is nearly completely removed during syngas production, as it is a poison for the catalysts used in F-T synthesis. However, F-T and conventional diesel fuels do have differences in fuel density, energy density, cetane number, lubricity, and distillation curves. The density of paraffinic diesel fuels is lower than conventional diesel, which increases volumetric fuel consumption to maintain engine performance. This shortcoming is slightly offset due to the higher concentration of hydrogen that increases the energy density of these fuels slightly above that of conventional diesel. The cetane number for F-T fuels is very high because of the n-paraffin content associated with these fuels. Benefits of increased cetane number for conventional diesel combustion include improved cold start characteristics, increased combustion efficiency, and reductions in exhaust emissions. Lubricity properties of paraffinic fuels is poor as a result of the near zero sulfur and low aromatic content, requiring lubricity additives. Distillation curves are informative for assessing cold flow and boiling point properties in complex liquids, such as hydrocarbon fuels (International Energy Agency – Advanced Motor Fuels; Clifford A. Moses 2008). Higher boiling points in fuels are related to increases in the carbon number. Increases in a compound's boiling point of the same carbon number increase in order of whether it is an iso-paraffin, n-paraffin, naphthenes, or aromatic. As a result of the chemical composition, the boiling points of paraffinic fuels are lower than conventional diesel. The freezing point for paraffinic fuels is lower however, improving cold weather suitability (Chevron Products Company 2007).

## **CHAPTER 3 METHODS**

### **3.1 Overview**

The methods for common rail system development, engine instrumentation and data collection, and fuel analysis are presented in this section. For reactivity controlled compression ignition combustion, an electronic common rail fuel injection system was developed to replace the original hydraulic injection system on a single-cylinder Yanmar TS230 medium-duty engine, in order to optimize the fuel injection strategy depending on engine speed, load, and fuel being researched. The CR system allows control of the fuel rail pressure independent of engine operating conditions and multi-pulse direct injection control. This is a requirement for the experimental design to create reactivity gradients of fuel and air in-cylinder, in order to control combustion phasing and reduce exhaust emissions. The criteria for success of this research are to achieve stable engine operation and reduced exhaust emissions with alternative fuels in dual fuel combustion.

### **3.2 Development of the Common Rail Fuel Injection System**

Based on the design objectives, the verification and validation process, known as the V-model, was used for fabrication and testing of the electronic fuel injection system as displayed in the flow diagram in Figure 4. A fuel injection test bench was initially built including hydraulic, mechanical, and electronic subsystems. Mechanical components were acquired from Robert Bosch GmbH and the electronic hardware was from National Instrument Corp. – Powertrain Controls.

System requirements were based on those described by Burrati et al. (2004), including electronically controlled fuel injection, adjustable rail pressure, and modular injection timing and quantity with multi-pulse capability. As displayed by the arrows in the flow diagram below, the V-model approach begins by identifying design requirements based on a full system level, such as those stated above for a CR fuel injection system, then breaks down into the subsystem level, and then into the individual components and their respective inputs and outputs. The progression moves back up the flow diagram sequentially with verification testing at the component level, subsystem level, and full system verification based on the specifications that drove the initial development stages.

The following sections present this process in detail including common rail system configuration, component and subsystem testing including rail pressure control, fuel injector calibration, and signal verification, followed by full system verification in a hardware-in-the-loop environment (HIL).

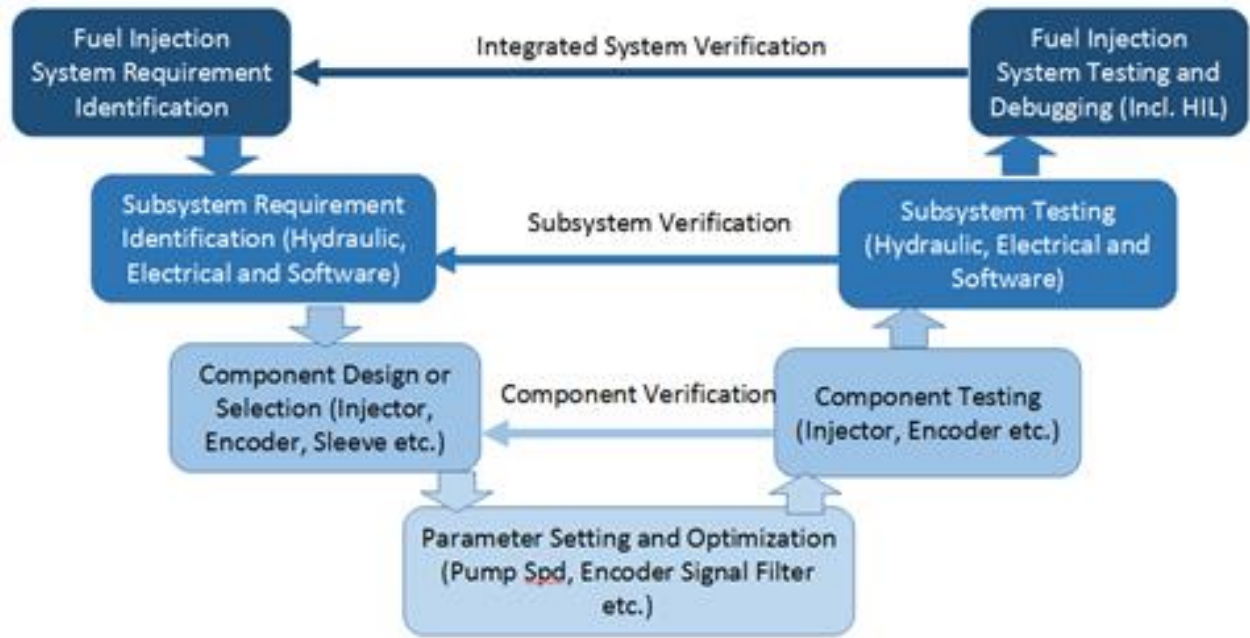
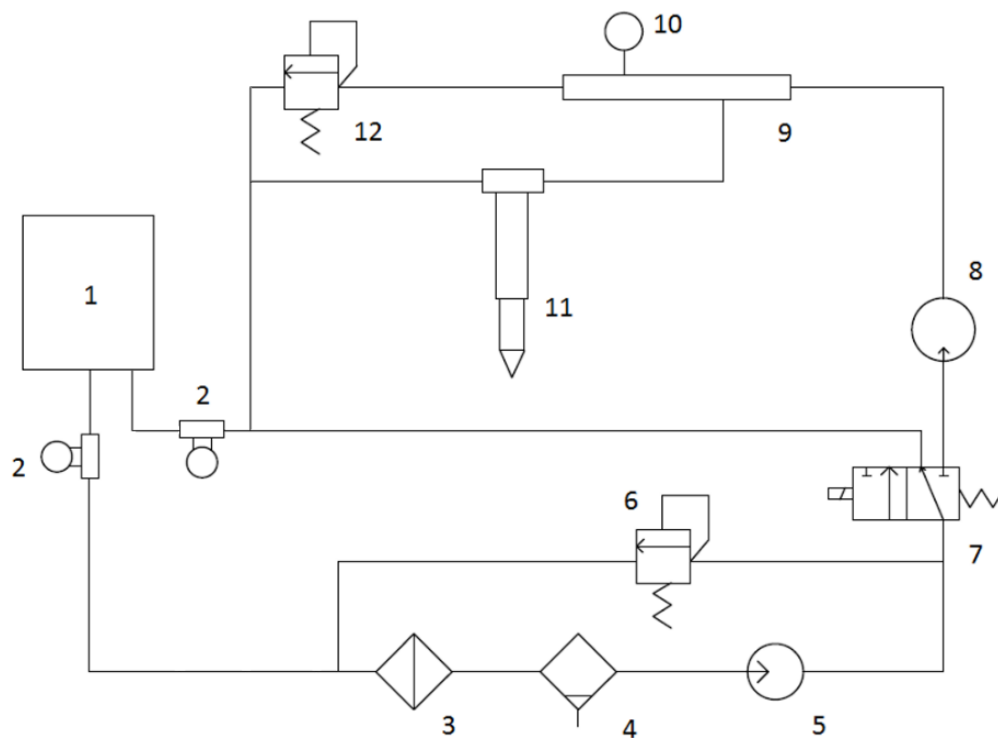


**Figure 4** Verification and Validation Process of the Fuel Injection System (Gaubert et al. 2017)

### 3.2.1 Hydraulic and Mechanical Subsystem Configuration

A schematic of the hydraulic and mechanical subsystem is displayed in Figure 5 and an image of the assembled test bench is displayed in Figure 6. The principle components include an AirDog Fuel Air Separation System FP-100 GPH, Bosch CP3 high pressure pump (HPP), Max Machinery P213 flowmeters (inlet and return), Bosch fuel rail, and Bosch piezoelectric fuel injector.



- |                           |                          |
|---------------------------|--------------------------|
| 1. Fuel Tank              | 7. Inlet Metering Valve  |
| 2. Flow Meter             | 8. High Pressure Pump    |
| 3. Fine Fuel Filter       | 9. Fuel Rail Accumulator |
| 4. Water Separator        | 10. Rail Pressure Sensor |
| 5. Low Pressure Pump      | 11. Fuel Injector        |
| 6. Low Pressure Regulator | 12. High Pressure Valve  |

**Figure 5** Schematic of the Hydraulic and Mechanical Subsystems (Gaubert et al. 2017)

The AirDog lift pump (components 3-6) is a gear rotor pump with a water separator and a 5 micron fuel filter, acting to preserve the integrity of the parts downstream, as diesel fuel is prone to water absorption, which can cause cavitation in tight tolerance parts damaging the high pressure pump and fuel injector. Fuel is sent from the lift pump at a constant pressure at 12 psi to the Bosch CP3 pump (components 7 & 8), which pressurizes the fuel in the fuel rail accumulator to pressures up to 2000 bar (29,000 psi). This pump is a rotary plunger pump driven by an AC motor through a belt and pulley system. A solenoid inlet metering valve (IMV) is connected to the outlet of the HPP to control the fuel rail pressure, which is controlled through pulse width modulation (PWM). The IMV is a normally closed, sending high pressure fuel to the fuel rail when not actuated. The

Bosch fuel rail accumulator contains the high pressure fuel sent to the fuel injector. Connected to the fuel rail is also a high pressure valve (HPV), which is a mechanical safety valve that opens when rail pressure surpasses the maximum 1800 bar rating of the components. Two Max Machinery P213 piston type fuel flow meters are configured in the system measuring the inlet flow from the lift pump to the HPP and the fuel return from the HPP and high pressure relief valve on the fuel rail. The labeled components in Figure 6 include A: Bosch CP3 pump, B: inlet metering valve, C: Bosch fuel rail, D: Bosch fuel injector, E: custom mounting bracket, F: AC motor, G: pressure sensor, H: high pressure relief valve.

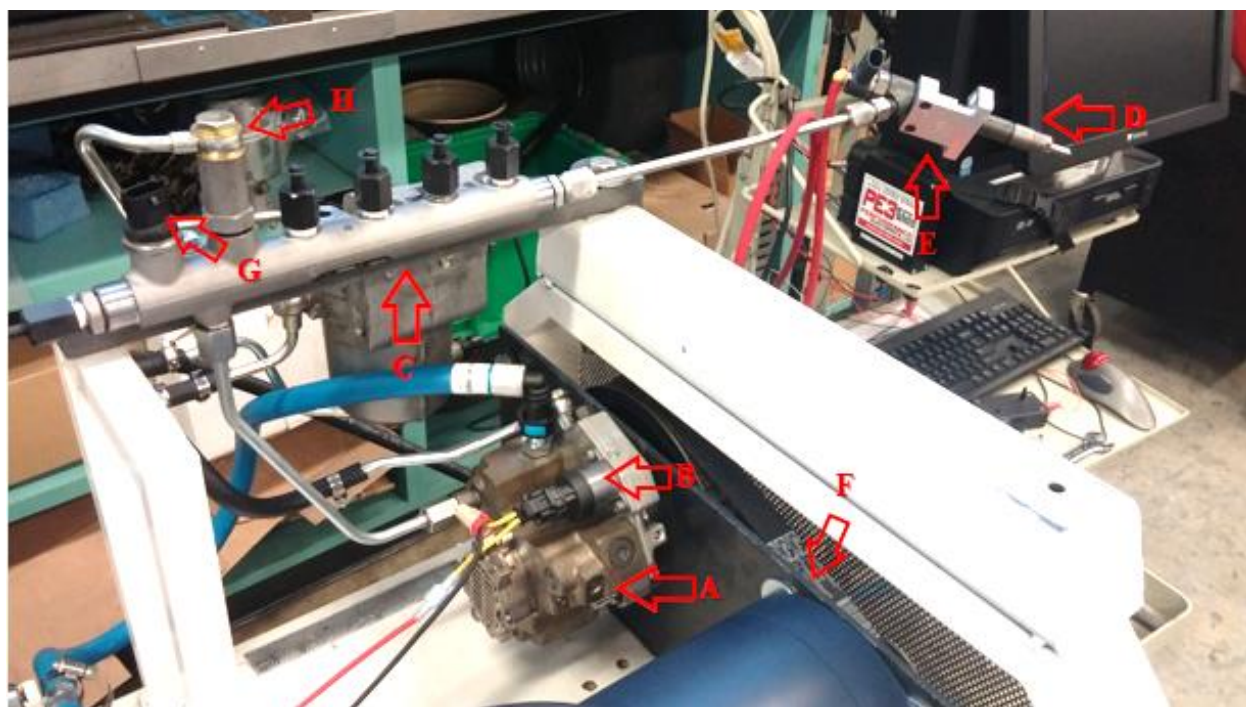


**Figure 6** Image of the Assembled Fuel Injection Test Bench

The inlet metering valve on the HPP, displayed in Figure 7, regulates rail pressure by actuating a solenoid through pulse width modulation depending on the pressure feedback signal. This solenoid valve operates at a frequency range of 120-200 Hz and should be adjusted in order to avoid harmonics with the pumping frequency. The three plunger pump rotates at a constant 2000 rpm equating to a pumping frequency of 100 Hz, avoiding the need for flex control parameters to adjust the solenoid frequency throughout operation. The second actuator is the fuel injector with custom rate shaping, timing, and duration commands depending on the tests being conducted.

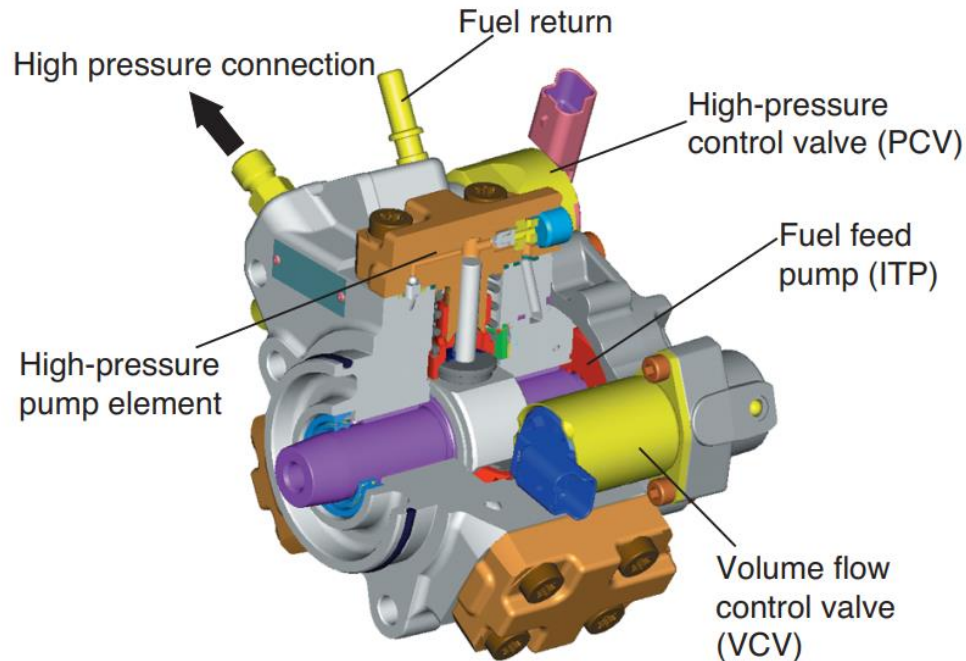


**Figure 7** High Pressure Pump Schematic (Blocking and Wenzlawski 2016)

### ***3.2.2 Electrical System Components and Sensor I/O***

The major functions of the electrical system include: controlling the fuel rail pressure, custom injection rate and shaping, engine synchronization for precise injection timing commands, and engine speed control. The electrical hardware managing these functions is National Instruments Direct Injection Driver System (NI DID), which is configured with four I/O modules. The module chassis is National Instruments CompactRIO 9076, which is a field programmable gate array (FPGA) real-time control system, operating at 400 MHz. Due to the precision required for engine synchronization and fuel injection commands, the FPGA is a necessity for engine research. The cRIO 9076 is a 4-slot chassis consisting of a Direct Injection Driver Module (NI 9751), PFI Driver Module (NI 9758), 4-Channel Analog Input Module (NI 9215), and 6-Channel Digital Input Module (NI 9411). Images of the NI DID interface are provided in the appendix, including the primary controller and troubleshooting windows.

Three analog sensors are implemented in the fuel injection system including the Bosch fuel rail pressure sensor as the input for the IMV, and two wire-wound linear potentiometers independently controlling the fuel injection duration of both the piezoelectric injector and port fuel injector. The pressure sensor on the fuel rail is a strain gauge type, oriented in a Wheatstone bridge configuration with an internal amplifier circuit in order to operate at high temperatures. A rotary

encoder is connected to the digital input module for engine synchronization. The DID interface includes filtering functions of the sensor inputs for signal integrity and stable control functions.

### 3.2.3 Rail Pressure Control Tuning

In order to calibrate the piezoelectric injector, the rail pressure control system was first tuned for stable fuel flow measurements across various rail pressures. This was completed through an open loop step input analysis on the rail pressure control loop to determine the control parameters. Figure 8 represents the fuel rail pressure control loop, in which the pressure sensor sends a feedback signal to the controller, and the error calculated is the difference from the setpoint value and the feedback value in order to adjust the IMV duty cycle based on Equation 1. The PID (proportional, derivative, and integral) output varies the duty cycle of the IMV, where  $e(t)$  is the error as a function of time, PV is the process variable,  $K_c$  is the proportional gain constant,  $T_i$  is the integral time constant, and  $T_d$  is the derivative time constant. The IMV is normally closed, which pertains to an indirect relationship between the rail pressure and duty cycle.

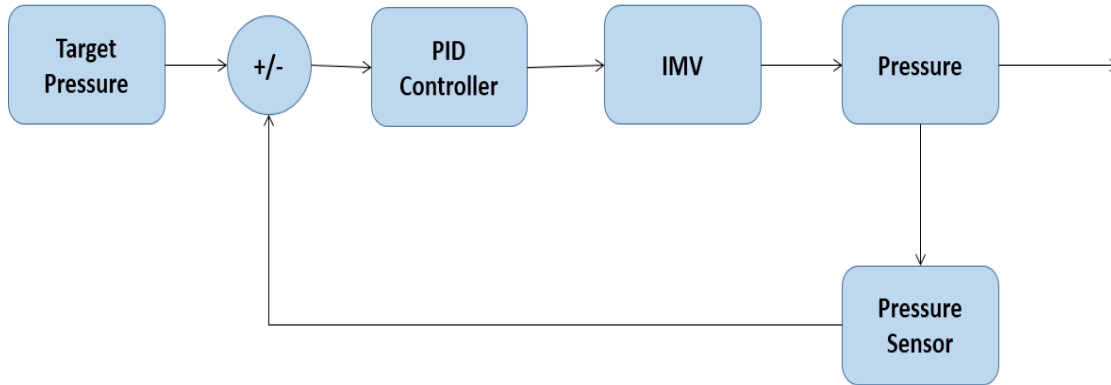


**Figure 8** Fuel Rail Pressure Control Feedback Loop (Gaubert et al. 2017)

$$\text{PID Output} = [K_c * e(t)] + \left[ \left( \frac{K_c}{T_i} \right) * \int e(t) dt \right] + [(K_c * T_d) * \frac{dPV}{dt}] \quad \text{Equation 1}$$

Open loop testing was conducted by manually inputting a constant duty cycle to the IMV in the NI DID interface and pressurizing the fuel rail until the pressure output stabilized, at which point the output was saturated for the given input. This step response was recorded in the DID interface and extracted into Excel to determine the model gain, deadtime, and time constant of the pressure response. Based on these values, initial p, i, and d values were determined through Equations 2, 3, and 4 respectively (Control Soft Inc. 2016).



$$p = 2 * (\text{Deadtime} + \text{Time constant}) / \text{Model Gain} \quad \text{Equation 2}$$

$$i = \text{Deadtime} + \text{Time Constant} \quad \text{Equation 3}$$

$$d = \text{Time Constant} / 6 \quad \text{Equation 4}$$

After defining the p, i, and d terms, closed loop control was investigated in order to tune these values according to PID theory for optimized response across rail pressure inputs and injector flow rates. This required filtering the pressure sensor signal with a low-pass filter in order to maintain stable output from the controller. Figure 9 displays the tuned control response. The initial overshoot occurs during startup, when the high pressure pump is started before the engine is cranked independently.

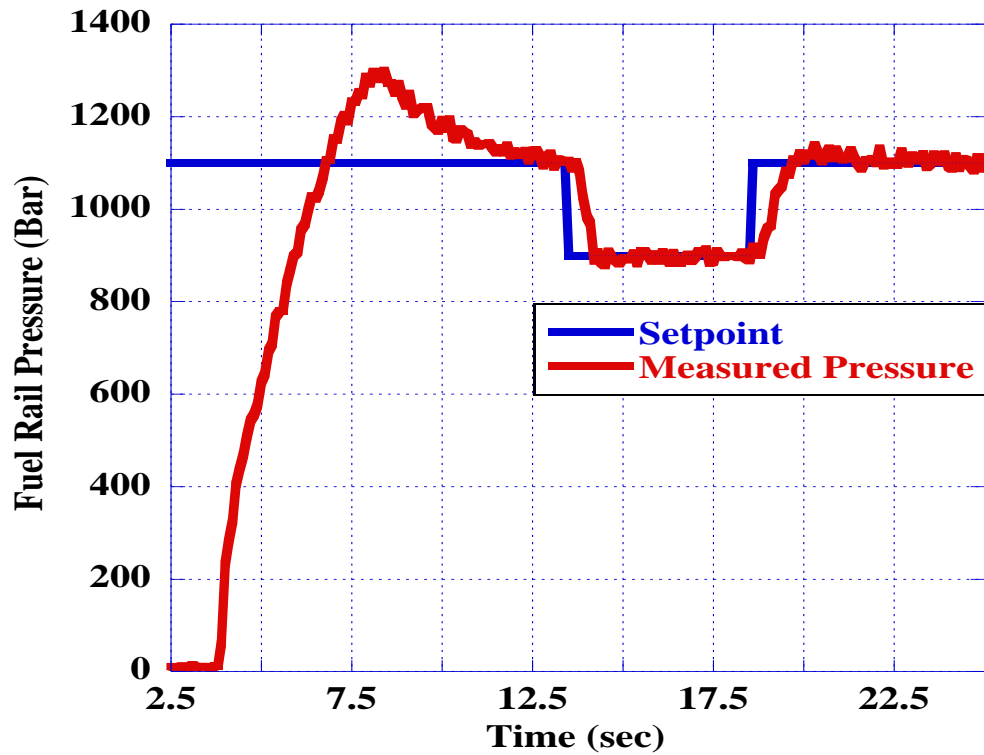


**Figure 9** Tuned Rail Pressure Control (Gaubert et al. 2017)

### 3.2.4 Common Rail Fuel Injector Operation

The CR fuel injector is a piezoelectric type with high pressure capabilities (up to 1800 bar), precise actuation timing, needle lift with nearly zero response time, and up to six injection pulses per cycle. Piezoelectric injectors are composed of a piezo actuator stack and operate based on the

inverse of the piezoelectric effect. The inverse piezoelectric effect implements an applied voltage to expand piezo stack, creating a large force on the internal flow control valve to open a low-pressure channel. The piezo stack is a longitudinal series of numerous ceramic platelets inside the injector body that is designed to handle a wide range of temperatures from  $-30^{\circ}\text{C}$  to over  $140^{\circ}\text{C}$  through proper insulation materials, a pretension spring, and proper design of the empty displacement of the actuator (Wolfgang and Wenzlawski 2016).

The internal functionality of a piezo type fuel injector is displayed in Figure 10. In the left image, the injector is unactuated; component (4) is seated closed, and high pressure fuel is present in both the control chamber (2) and the high-pressure chamber (3). In this state, the return flow outlet is closed and the nozzle needle is seated in the nozzle sac due to the pressure difference between the control chamber and the nozzle tip. The larger area of the control chamber compared to the free area under the nozzle tip creates a larger force at (F1) than (F2). When the piezo stack is actuated, as in the right side image, the valve plunger (8) opens the orifice between the control chamber and the fuel return. This creates a larger force at (F2) than at (F1), causing the nozzle needle to lift and inject fuel through the injector orifices into the combustion chamber (Wolfgang and Wenzlawski 2016).

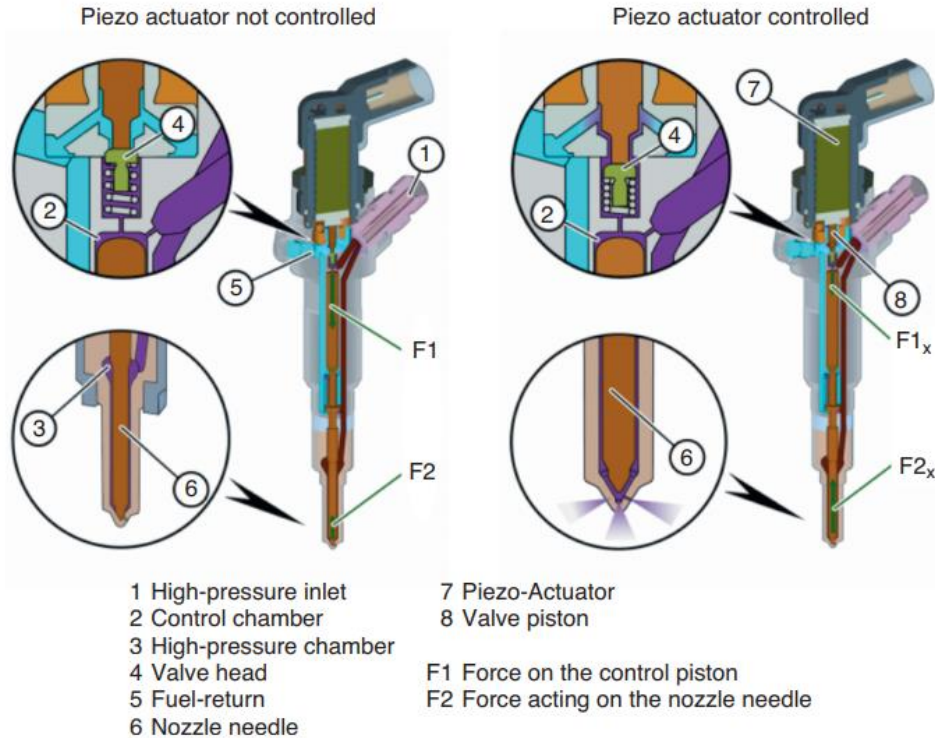


**Figure 10** Internal Function of a Piezoelectric Injector (Blocking and Wenzlawski 2016)

In order to determine the required maximum flow rate of the fuel injector for calibration, the brake specific fuel consumption (BSFC) of the experimental engine with the original fuel injection system was mapped across operating speeds and loads. Engine operating conditions included speeds up to 1700 rpm and loads up to 8 bar indicated mean effective pressure. The common rail system was required to reach a maximum flow rate of 50 mm<sup>3</sup> per injection at all rail pressures. The Bosch piezoelectric injector (model #: 0 445 116 010) has a 120° symmetric spray patten with 8 nozzle orifices with diameters of 0.115 mm. The minimum injection duration of the injector is 0.15 ms and the maximum injection pressure is 1800 bar. Operating specifications for this injector are listed in Table II, in which the actuation voltage increases linearly from 200 to 1200 bar and from 1200 to 1800 bar. The piezo stack inside the injector acts similar to that of a capacitor and requires both charging and discharging of the applied current for each injection. The “IPhase Array” in the DID interface contains four elements for charging and four elements for discharging. These elements specify the charging/discharging current at the injector providing proprietary rate shaping such as square, ramped, and boot shaped. For the research conducted, a

boot shaped profile was implemented with an initial high current level for quick opening and reduced amperage to hold the injector open (10A peak and 9A hold).

**Table II:** Bosch Piezoelectric Injector Operating Specifications

| <b>Operating Voltage</b>                                                   |  |
|----------------------------------------------------------------------------|--|
| Voltage at p_Rail: $\leq 200$ Bar - 110 V Nominal                          |  |
| Voltage at p_Rail: 1200 Bar - 118 V <sub>min</sub> to 133 V <sub>max</sub> |  |
| Voltage at p_Rail: 1800 Bar - 127 V <sub>min</sub> to 156 V <sub>max</sub> |  |
| <b>Charging &amp; Discharging Current/Duration</b>                         |  |
| 100 - 200 $\mu$ s                                                          |  |
| 17 A Peak                                                                  |  |

### 3.2.5 Fuel Injector Calibration

Injector calibration testing was conducted at pressure ranges from 400 bar to 800 bar and injection durations beginning at 0.5 ms until the maximum required flow rate was reached, at 50 mm<sup>3</sup>. Flow measurements were conducted in a gravimetric procedure, in which 1000 consecutive injection pulses were given at intervals of 100 ms into a beaker. The beaker was then weighed to determine the total mass, divided by 1000, and divided by fuel density for the volumetric flow per injection. Figure 11 displays the injector calibration curves across rail pressures. Table III displays the respective average volumetric fuel output and standard deviation at their respective experimental test conditions. Each test condition was repeated three times to improve flow measurement accuracies. However, at high pressures such as those used in common rail injection systems, both liquid jets and vapors are produced. Escaping vapors induced small errors in the measurements. From the calibration curve, each rail pressure resulted in two sections of linear relationships between output and injection duration. The percent standard deviation was below 1.0% for each test condition except for at 400 bar and 0.5 ms duration, at which the standard deviation was 3.3%.

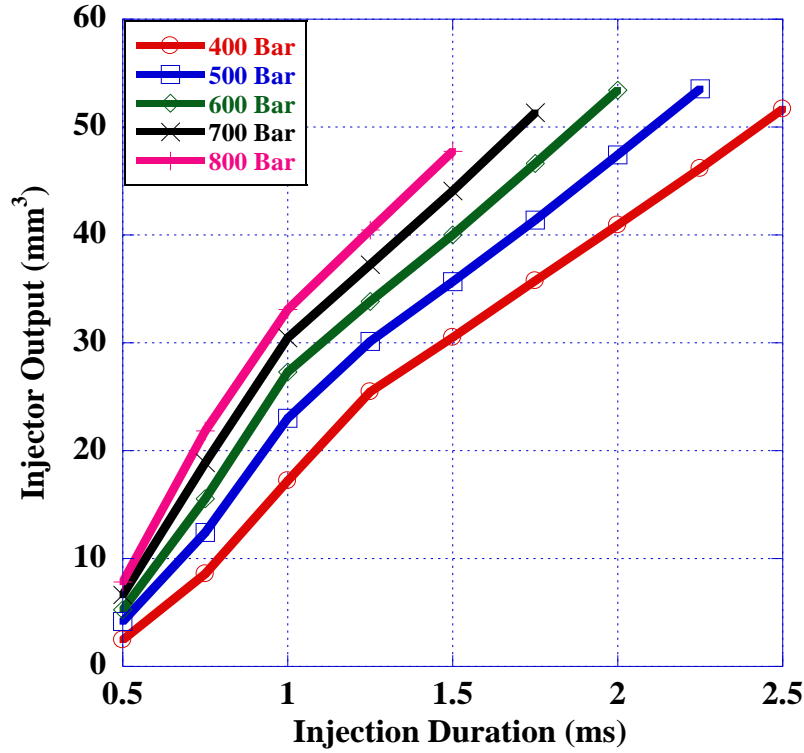


**Figure 11** Piezoelectric Injector Calibration Curve (Gaubert et al. 2017)

**Table III:** Flow Rate and Standard Deviation of Piezoelectric Injector Calibration Curve

|         | 400 Bar                   |         | 500 Bar                   |         | 600 Bar                   |         | 700 Bar                   |         | 800 Bar                   |         |
|---------|---------------------------|---------|---------------------------|---------|---------------------------|---------|---------------------------|---------|---------------------------|---------|
| PW (ms) | Output (mm <sup>3</sup> ) | STD (%) | Output (mm <sup>3</sup> ) | STD (%) | Output (mm <sup>3</sup> ) | STD (%) | Output (mm <sup>3</sup> ) | STD (%) | Output (mm <sup>3</sup> ) | STD (%) |
| 0.5     | 2.48                      | 3.30%   | 4.165                     | 0.12%   | 5.26                      | 0.38%   | 6.61                      | 0.45%   | 7.82                      | 0.26%   |
| 0.75    | 8.595                     | 0.64%   | 12.43                     | 0.08%   | 15.54                     | 0.10%   | 18.9                      | 0.11%   | 21.83                     | 0.16%   |
| 1       | 17.23                     | 0.61%   | 23.025                    | 0.28%   | 27.295                    | 0.05%   | 30.455                    | 0.05%   | 33.08                     | 0.17%   |
| 1.25    | 25.45                     | 0.12%   | 30.11                     | 0.17%   | 33.825                    | 0.01%   | 37.26                     | 0.24%   | 40.47                     | 0.10%   |
| 1.5     | 30.49                     | 0.30%   | 35.67                     | 0.14%   | 39.995                    | 0.09%   | 44.105                    | 0.12%   | 47.75                     | 0.40%   |
| 1.75    | 35.76                     | 0.07%   | 41.365                    | 0.40%   | 46.62                     | 0.21%   | 51.35                     | 0.20%   | -                         | -       |
| 2       | 40.93                     | 0.06%   | 47.415                    | 0.03%   | 53.435                    | 0.01%   | -                         | -       | -                         | -       |
| 2.25    | 46.17                     | 0.22%   | 53.575                    | 0.14%   | -                         | -       | -                         | -       | -                         | -       |
| 2.5     | 51.67                     | 0.13%   | -                         | -       | -                         | -       | -                         | -       | -                         | -       |

### 3.2.6 Signal Timing Verification

Injection timing precision is essential for engine research to maintain experimental repeatability and accuracy, especially when implementing multiple pulses in an interval of less than 20 ms. Signal verification of the actuation signal from the engine controller to the fuel injector

was conducted to compare the injection timing (crank angle basis) input into the engine control interface and the output voltage/current with respect to a rotary encoder signal.

The pulse width modulated actuation signal for the piezoelectric injector operates at high frequencies and voltages that are unmeasurable with the data acquisition system used in this experiment. A circuit was designed, as displayed in Figure 12, to convert this high voltage signal to a single square wave in a measurable range. This circuit consists of an inductor coil, current divider, and capacitor for a stable voltage signal to be read by an oscilloscope along with the rotary encoder signal.

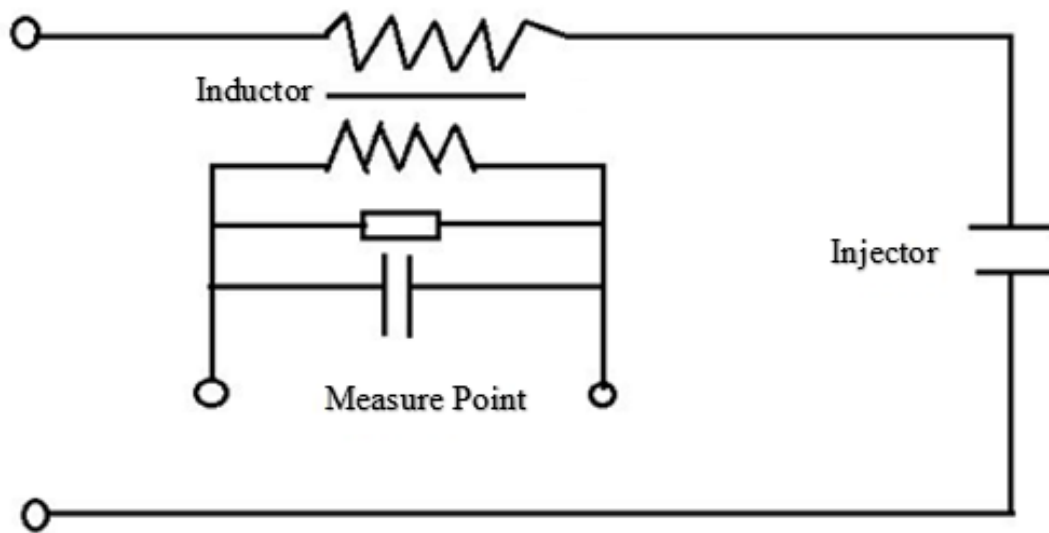


**Figure 12** Piezoelectric Injector Measurement Probe

A brushless DC motor was coupled to the rotary encoder shaft to externally drive the signal at a constant speed, triggering the injection commands from the engine controller. Two injection pulses were arbitrarily input into the controller interface at  $20^\circ$  BTDC and  $50^\circ$  ATDC, where the TDC signal is the index pulse of the rotary encoder as displayed in Figure 13. Five consecutive signals were located in a crank angle basis respect to the rotary encoder index signal. These locations were averaged for both the first and second injection, which were calculated to be  $18^\circ$  BTDC and  $52^\circ$  ATDC. The  $2^\circ$  difference from the manual inputs in the interface, are attributed to slight changes in the motor rpm during testing.

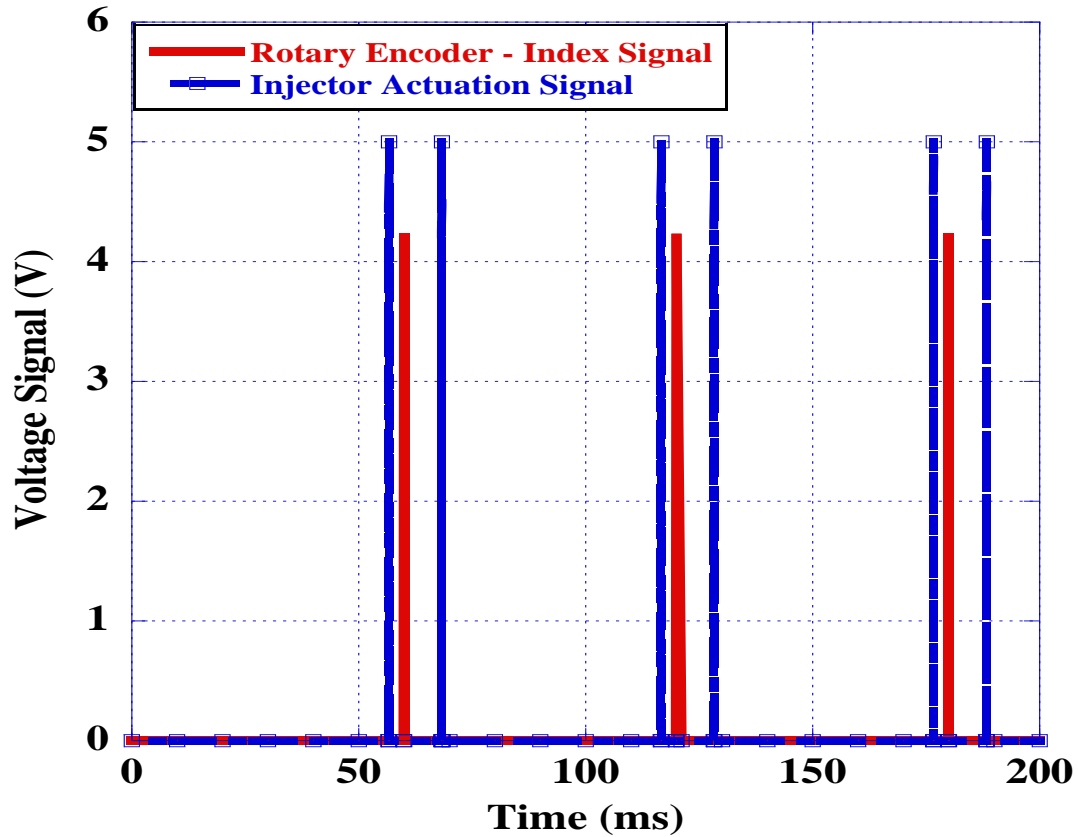


**Figure 13** Injection Timing Validation (Gaubert et al. 2017)

### ***3.2.7 Hardware-in-the-Loop Testing***

The common rail system was tested in a hardware-in-the-loop (HIL) environment in order to validate full operation with simulated engine dynamics. Figure 14 displays the flow diagram for HIL testing with various points for signal monitoring. The simulated plant was the engine and dynamometer based on physical parameters of the experimental engine such as BSFC, inertial forces, FMEP, and injection duration vs. injection amount. A single chip microcontroller was used for engine simulation in a mean effective value model, relating injection mass per cycle to IMEP, which was derived from physical engine data.

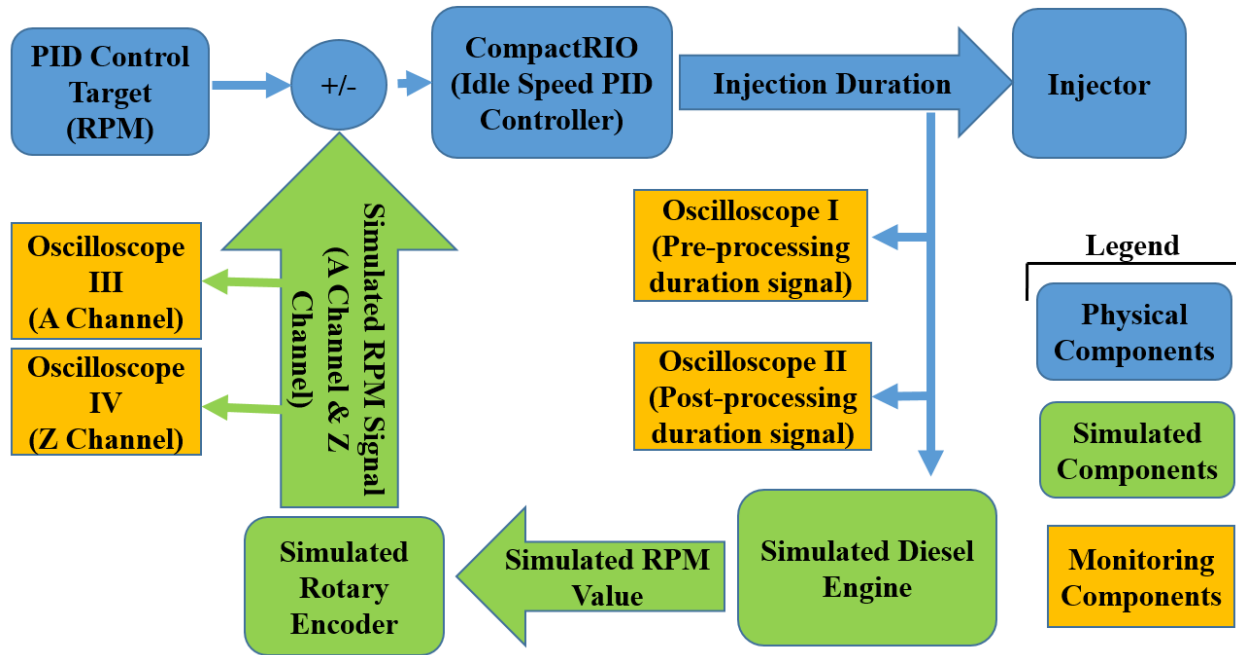


**Figure 14** HIL Testing System Configuration (Gaubert et al. 2017)

Two operating conditions were simulated to tune a PI controller for cruise control including: transient engine speed at constant load and transient load at constant speed. Figures 15 and 16 display the controller results respectively. The constant load simulation displays accurate control of the engine as the engine speed is adjusted. The dynamic load simulation switches engine load from 3.5 bar to 7.5 bar IMEP instantaneously, in a time equal to one engine cycle. Results of the engine controller display large overshoot and undershoot at these points of load changes in the simulation. In physical engine testing, the load changes gradually with the hydraulic dynamometer, in which the controller was determined to maintain engine speeds when fully integrated to the engine.



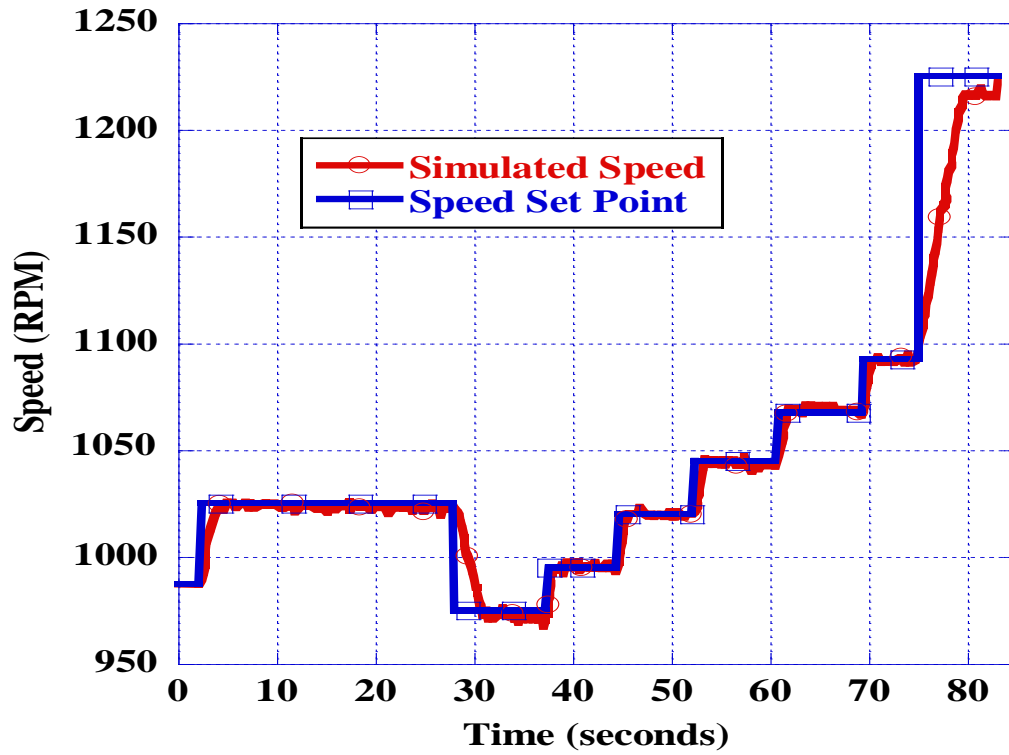


Figure 15 Constant Speed at Constant Load HIL Results (Gaubert et al. 2017)

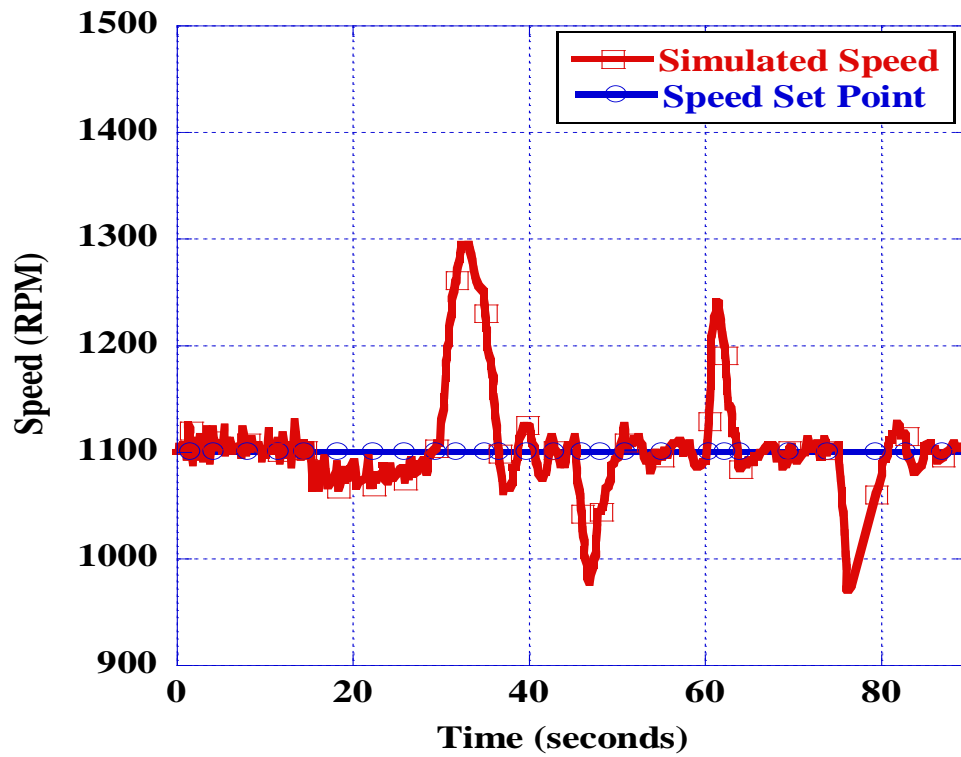
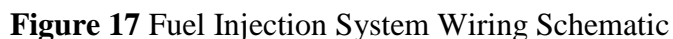
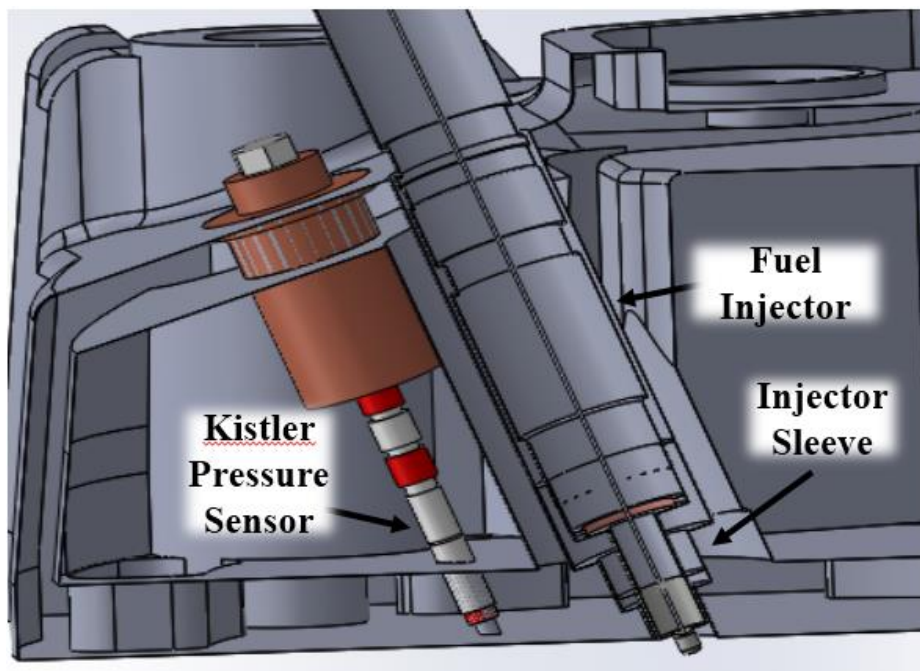


Figure 16 Transient Load at Constant Speed HIL Results (Gaubert et al. 2017)



A custom injector sleeve was designed and manufactured for the piezo-type injector to mount into the original equipment manufacturer (OEM) cylinder head. The piezoelectric fuel injector is much narrower than the OEM hydraulic injector, presenting the need of a sleeve to increase the diameter of the injector body to seal the injector to the combustion chamber without modifying the cylinder head. A 3-D cross section of the cylinder head with the mounted injector and injector sleeve is displayed in Figure 18 below. The inner diameter was designed to fit the injector nozzle with tolerance accounting for thermal expansion. Mounting of the injector and

sleeve assembly implement two copper crush washers: one between the injector body and sleeve and the other between the sleeve and cylinder head. The inner washer is to ensure the fuel injector is not over torqued, damaging the piezo stack, and the second is in contact with the cylinder head to ensure a proper seal to the combustion chamber.



**Figure 18** A 3-D Cross Section of a New Fuel Injector Adapted to the Original Cylinder Head  
(Gaubert et al. 2017)

A redesign of the injector nozzle was also created due to the  $70^\circ$  angle that the injector is mounted in the cylinder head. Figure 19 below displays the piezoelectric injectors original  $120^\circ$  symmetric spray pattern when mounted to the cylinder head. With a symmetric pattern, a high amount of wall wetting on the cylinder head occurs, resulting in excessively high levels of unburned hydrocarbons. Figure 20 displays the 4-hole OEM injector spray angle and the newly developed seven-hole spray angle for the piezoelectric injector. The custom injector nozzle was designed to replicate the  $135^\circ$  asymmetric spray angle of the OEM injector with more holes of a smaller diameter for increased spray distribution and improved fuel atomization.

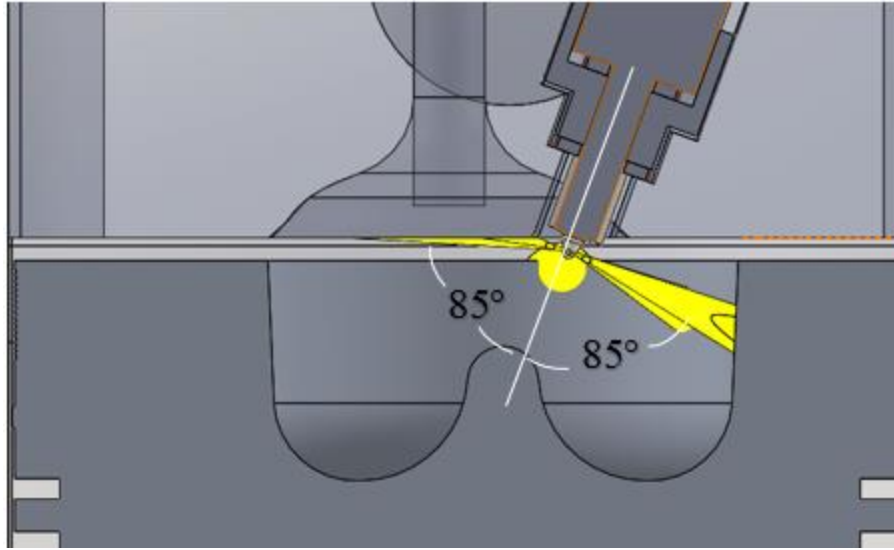


**Figure 19** Wall Wetting with the Piezoelectric Injector

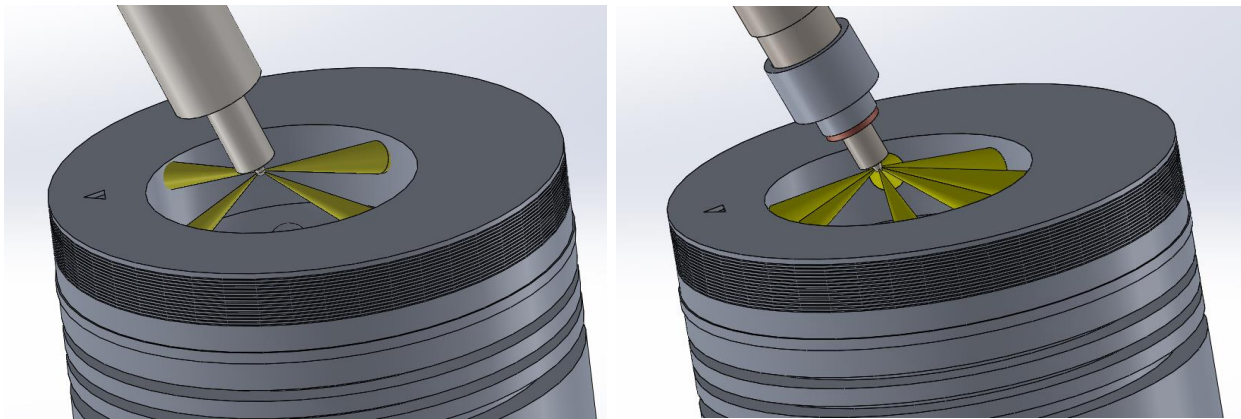


**Figure 20** (Left) Original Injector Spray Pattern; (Right) Custom Injector Spray Pattern (Gaubert et al. 2017)

The custom fuel injector nozzle calibration was outsourced and conducted by the supplier, as provided in Figure 21. This calibration curve displays linear relationship throughout the mapping conditions between injection duration and injector output, except for at 1200 bar rail pressure. At this rail pressure, there is a node at 1.25 ms injection duration, where the slope reduces. Volumetric output values and their corresponding percent standard deviation are provided in Table IV. Percent standard deviation for each point is below 1%, except at the injectors' minimum injection duration, 0.25 ms, ranging from 1.5% to 3.0%

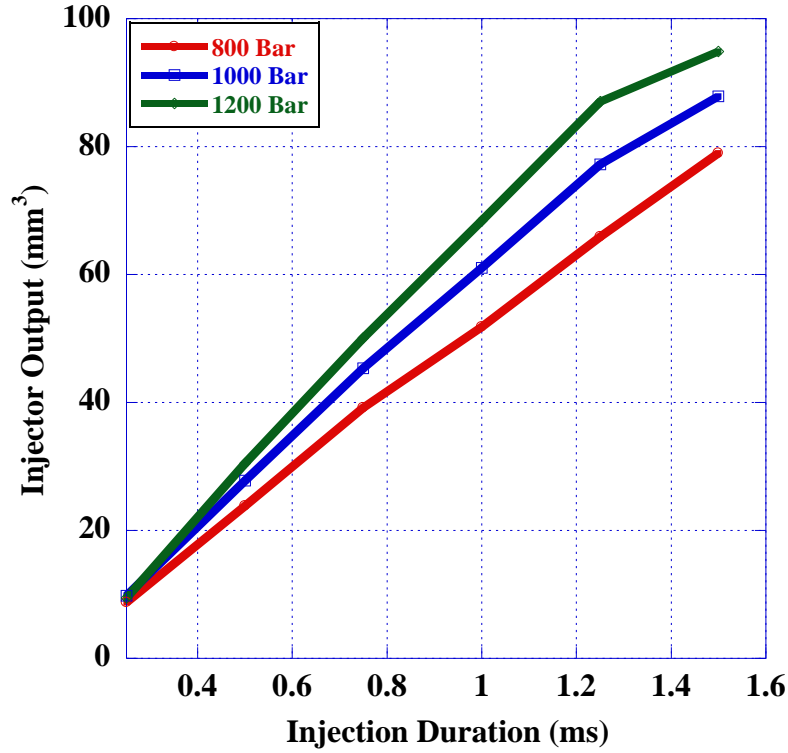


**Figure 21** Custom Nozzle Injector Calibration

**Table IV:** Flow Rate and Standard Deviation of Custom Nozzle Injector Calibration Curve

|         | 800 Bar                   |         | 1000 Bar                  |         | 1200 Bar                  |         |
|---------|---------------------------|---------|---------------------------|---------|---------------------------|---------|
| PW (ms) | Output (mm <sup>3</sup> ) | STD (%) | Output (mm <sup>3</sup> ) | STD (%) | Output (mm <sup>3</sup> ) | STD (%) |
| 0.25    | 8.75                      | 1.47%   | 9.78                      | 2.17%   | 9.44                      | 2.98%   |
| 0.5     | 23.85                     | 0.69%   | 27.78                     | 0.85%   | 30.52                     | 0.81%   |
| 0.75    | 39.21                     | 0.36%   | 45.37                     | 0.53%   | 50.12                     | 0.51%   |
| 1.00    | 51.84                     | 0.47%   | 61.03                     | 0.38%   | 68.44                     | 0.37%   |
| 1.25    | 65.94                     | 0.24%   | 77.22                     | 0.31%   | 87.05                     | 0.32%   |
| 1.50    | 78.99                     | 0.30%   | 87.84                     | 0.20%   | 94.87                     | 0.26%   |

### 3.3 Engine Specifications and Instrumentation

A 1.1L medium duty experimental engine with a proprietary electronic common rail fuel injection system was researched in dual fuel combustion. Engine specifications are provided in Table V. As discussed previously, the fuel injector nozzle is designed with an asymmetric spray pattern, creating an even distribution of fuel in the omega bowl piston. The spray angle with respect to the fuel injector axis, reduces from 85° to 50°. The engine is also equipped with additional auxiliary systems such as low-pressure EGR, port fuel injection, and intake boosting. EGR is

controlled with a backpressure valve before the exhaust outlet, to vary the pressure in the exhaust manifold at levels above that of the intake prior to the supercharger. An RC racing port fuel injector is mounted to the intake manifold, operating at a pressure of 2.76 bar. The supercharger is a centrifugal type A1 Procharger and is driven off of an external AC motor. Boost pressure is controlled by varying the output of a variable frequency drive to change the speed of the supercharger. The National Instruments Direct Injection Driver System was used to control the fueling ratio between PFI and DI, fuel rail pressure, and combustion phasing (CA50).

**Table V: Engine Specifications**

|                            |                      |
|----------------------------|----------------------|
| <b>Bore x Stroke</b>       | 112 mm x 115 mm      |
| <b>Number of Cylinders</b> | 1                    |
| <b>Compression ratio</b>   | 16:1                 |
| <b>Displacement</b>        | 1.132 L              |
| <b>Maximum Power</b>       | 17 kW @ 2200 rpm     |
| <b>Maximum Torque</b>      | 77.5 N·m at 1400 rpm |
| <b>Cooling System</b>      | Water                |
| <b>DI Injection Nozzle</b> | 7 x 0.115 mm         |
| <b>Rail Pressure</b>       | 800-1200 bar         |
| <b>PFI Pressure</b>        | 2.76 bar             |

A schematic of the engine instrumentation is provided in Figure 22. In-cylinder combustion pressure is measured with a Kistler 6053cc uncooled piezoelectric pressure transducer. Pressure measurements are recorded with respect to an Omron E6C3-CWZ3EH incremental rotary encoder for crank angle analysis. Cycle to cycle pressure data was averaged over 100 cycles for each research point with a resolution of 0.18 crank angle degree (CAD). Pressure sensor signal was conditioned with a Kistler 5010B dual mode amplifier and recorded with a Yokogawa DL850 high speed data acquisition at a sampling frequency of 45 kHz. Brake engine power of the experimental engine was measured with an Omega TQ513 model torque cell assembly, with the load supplied by a hydraulic dynamometer coupled to the crankshaft. The amplified pressure signal is also linked to an AVL Indicom v2.5 for real-time monitoring of indicated mean effective pressure, combustion phasing, coefficient of variation, and maximum pressure rise rates. These parameters allow for real-time engine control stability and to ensure both engine and operator safety. Supporting images of the AVL Indicom v2.5 interface are provided in Appendix C.

Air flow rates through the intake manifold were measured with a Meriam Z50MC-2 laminar flow meter, based on the differential pressure principle across the laminar filter element. Environmental conditions, such as temperature, pressure, and relative humidity, were measured in parallel and interfaced with a LFS-1 electronic measurement system for accurate volumetric flow measurements. EGR rates were varied by adjusting the position of a back-pressure valve on the exhaust manifold and routed through a shell and tube heat exchanger for temperature control. Two EMS Model 5002 exhaust gas analyzers were used to determine the ratio of CO<sub>2</sub> in the intake and exhaust for EGR percent in the intake. An exhaust pressure sensor was mounted upstream of the backpressure valve to ensure the exhaust sampling pressure was not above rated specifications for the AVL equipment.

Intake boost was measured with a Kulite ETL-175-190M pressure transducer at the intake port. Boost pressures were kept constant at 3 psi for all operating conditions. Heaters on the intake manifold were controlled with Omega CN4000 series temperature controllers to elevate temperatures for increased vaporization of the port fuel injection n-butanol. Fuel flow rates of the common rail system were measured with Max Machinery P213 piston flow meters on both the inlet and return lines and a Max Machinery P001 model piston flow meter measured the PFI flow rate. The fuel flow meters are designed with variable output transmitters for optimal resolution and, anti-dithering, and signal dampening. An NI 6251 data acquisition unit recorded the fuel flow measurements at a sampling rate of 1.25 mega samples per second. Appendix C includes additional supporting images of the LabVIEW block diagram and front panel for data acquisition of flow rate measurements. An AVL SESAM FTIR V4 measured gaseous emissions using a diesel exhaust recipe and an AVL 483 Micro Soot Sensor measured particulate matter. Exhaust samples were maintained at 191°C to avoid condensation and carbon deposits in the sampling lines and recorded at a frequency of 1 Hz and averaged over 2250 engine cycles. Figures 23 and 24 are images of the engine test cell and instrumented fuel flow meters respectively.



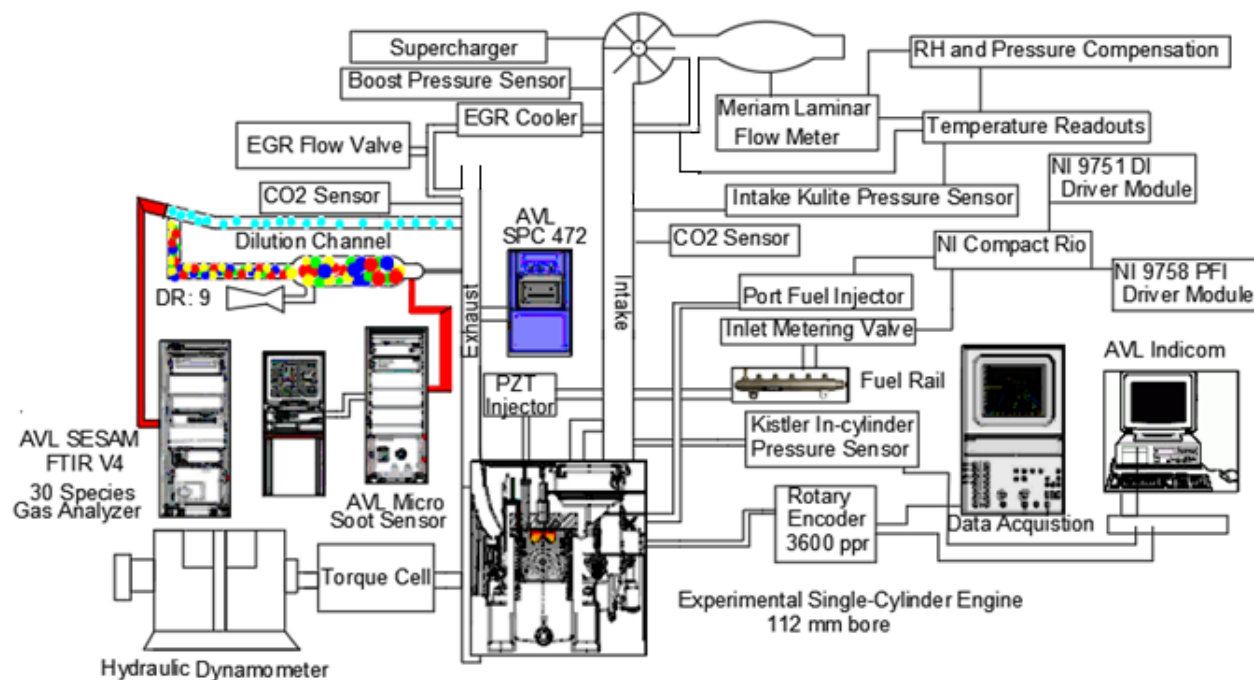


**Figure 22** Experimental Engine Setup

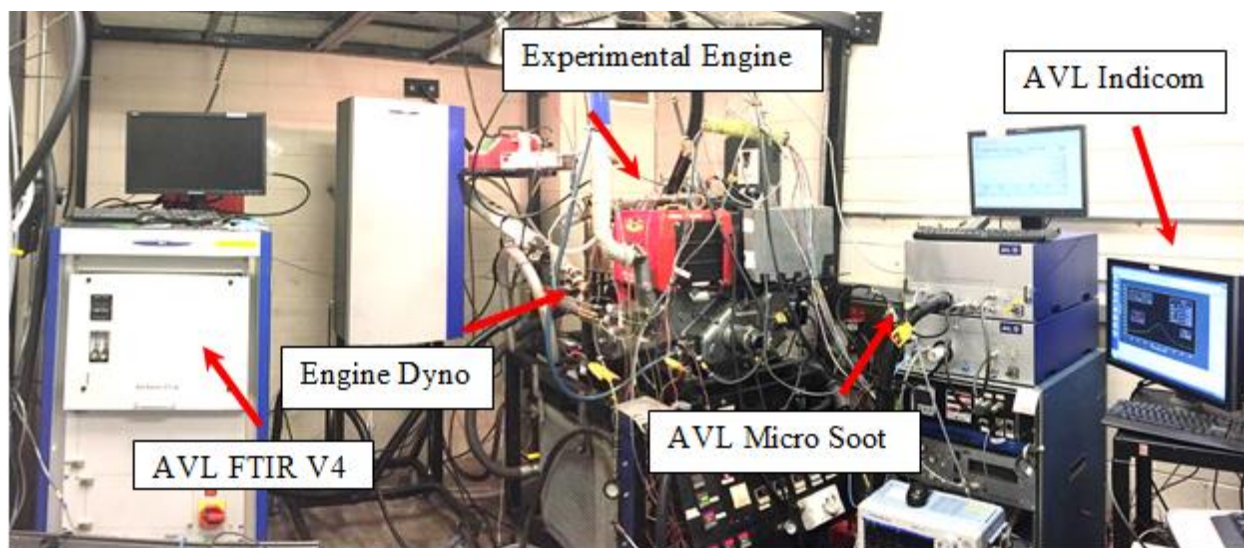


**Figure 23** Image of the Engine Test Cell



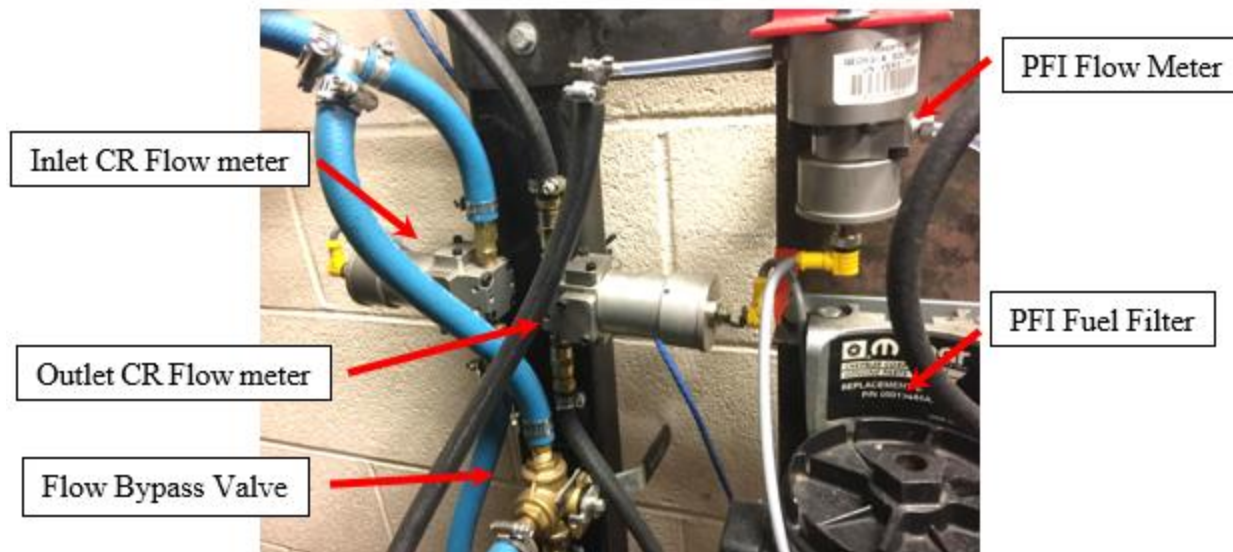


**Figure 24** Image of the Fuel Flow Meters

### 3.4 Fuel Analysis

Fuel tests were conducted prior to engine research in order to correlate the physical and chemical properties to the combustion process. Fuel chemistry results are used to accommodate necessary fuel injection strategies at different operating conditions and for a more in-depth analysis of the combustion and emissions results.

#### 3.4.1 Parr 1341 Constant Volume Calorimeter

The energy content of the fuels were measured with a Parr 6772 constant volume calorimeter. The apparatus is displayed in Figure 25, where the sample is placed in a pressurized chamber of  $O_2$  with a fuse wire (of known energy density) across the top of the sample and immersed in a bucket of water. Combustion is initiated by igniting the fuse and a thermocouple measures the change in water temperature from the heat released to determine the gross heating value. This calorific value represents the heat produced by both the burning sample and water vapor condensation. Water vapor is typically exhausted as unusable energy, and the net heating value ( $H_{net}$ ) is derived by subtracting the latent heat from the gross heat ( $H_c$ ) based on the standard ASTM D240 using Equation 5 (*1341 Plain Jacket Calorimeter Operating Instruction Manual 2014*). The equation requires the known hydrogen percentage of the sample. There are variances in fuel structures, however the hydrogen percent for ULSD, S8, and n-butanol were assumed to be 12.5%, 15.4%, and 13.5% respectively.

$$H_{net} = 1.8H_c - 91.23H$$

Equation 5

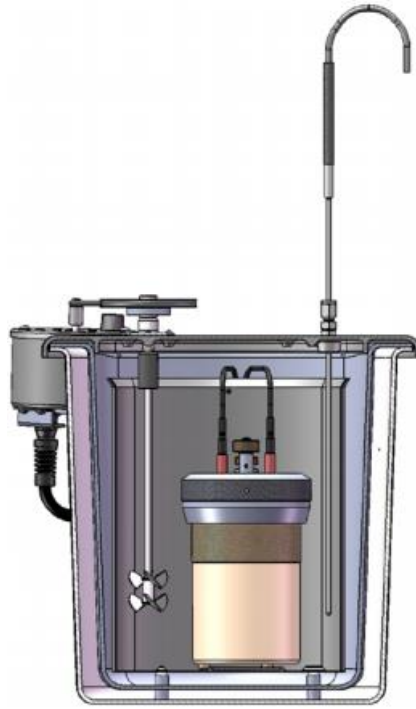


**Figure 25** 1341 Calorimeter Cross Section (*1341 Plain Jacket Calorimeter Operating Instruction Manual 2014*)

### 3.4.2 Brookfield DV II Pro Rotational Viscometer

Viscosity is a measure of a fuel's resistance to flow, which can be correlated to the wear on the fuel injector and pump along with the fuel's atomization quality. The test is conducted with a Brookfield Viscometer DV-II Pro Type measuring the torque of a motor rotating a cylindrical spindle in a fuel sample to derive the dynamic viscosity, as displayed in Figure 26. There are many different cylindrical shapes; however the spindle type (SC-18 for diesel like fuels) is of known geometry and rotating with a known angular velocity to determine the shear rate in Equation 6. Based on the geometry and torque of the motor, the shear stress at the surface of the spindle is determined. With the shear rate and stress, the dynamic viscosity can then be calculated with Equation 7, where  $\dot{\gamma}$  is the shear rate in  $s^{-1}$ ,  $\omega$  is the angular velocity in rad/s,  $R_c$  and  $R_b$  are the radii of the container and spindle in meters,  $L$  is the length of the cylinder in meters,  $M$  is the motor torque in Nm, and  $\tau$  is the shear stress in  $N/m^2$  (David Roylance 2000).

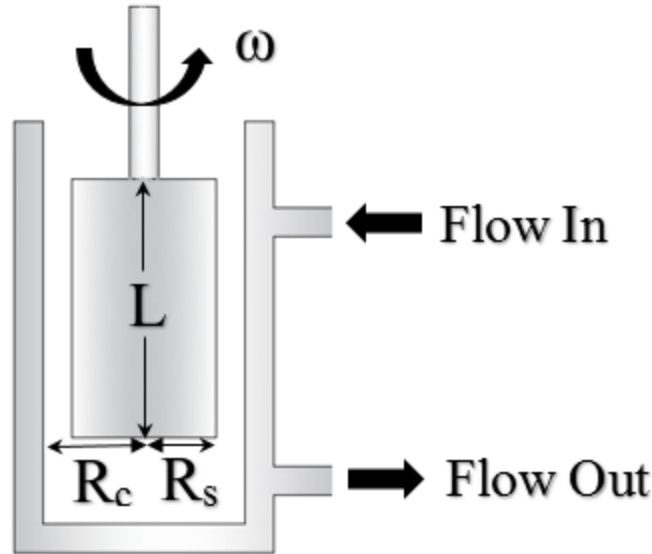


**Figure 26** Rotational Viscometer Schematic

$$\dot{\gamma} = \frac{2\omega R_c^2}{R_c^2 - R_s^2} \quad \text{Equation 6}$$

$$\tau = \frac{M}{2\pi R_s^2 L} \quad \text{Equation 7}$$

The experiment measures the torque of the motor with an attached spindle in a 7.0 mL fuel sample across a specified temperature range. Coolant is circulated through a heating chamber with a heating element, which is controlled with an Omega temperature controller, and routed to the jacket containing the fuel sample. The temperature is gradually increased and data is recorded with Rheocalc software at 2°C increments from 26°C to 90°C.

### 3.4.3 PAC CID510 CVCC

Autoignition quality, or cetane number (CN), of the fuels were analyzed in a PAC CID510 constant volume combustion chamber (CVCC). The instrument is designed with an electronic common rail fuel injection system with a solenoid fuel injector, simulating real world diesel engine systems. The solenoid injector has 6 orifices at diameters of 0.17 mm. This experiment followed ASTM method D7668-14a (2014), deriving the DCN provided in Equation 8. Operating parameters included a pre-conditioned combustion chamber maintaining a wall temperature of 595°C and initial chamber pressure of 20 bar. Fuel was injected at 1000 bar rail pressure, at a pulse width duration of 2.5 ms. Each experiment began with five pre-injection cycles and determination of the derived cetane number (DCN), ignition delay, and combustion delay were averaged over 15

combustion cycles. The ignition delay (ID) and combustion delay (Cd) are defined as the duration from start of injection, at time equals 0 ms, to the start of combustion (at 20.2 bar pressure) and to the mid-point of the combustion pressure curve respectively. Statistical analysis is conducted on the calculated ID and Cd of the 15 cycles according to Peirce's Criterion, to ensure accurate and repeatable results.

$$DCN = 13.028 - \frac{5.3378}{ID} + \frac{300.18}{Cd} + \frac{3415.32}{Cd^2} \quad \text{Equation 8}$$

A model of the fuel injection system and combustion chamber is illustrated in Figure 27. The labeled components include: (1) the solenoid actuated injector with high pressure common rail system, (2) the uniformly heated test chamber, (3) the chamber pressure sensor, and (4) the injection pressure sensor.

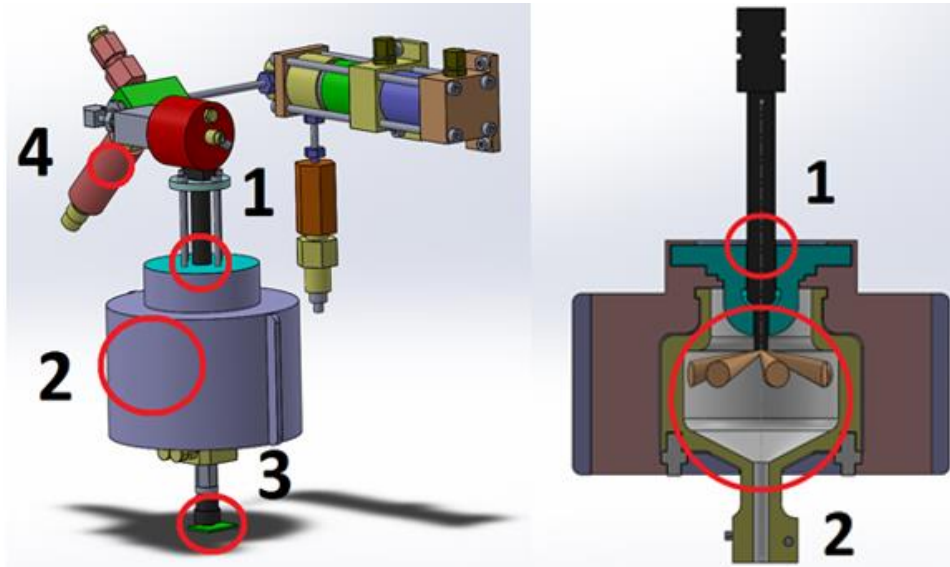


**Figure 27** Constant Volume Combustion Chamber Design

#### 3.4.4 Shimadzu DTG-60

Thermal gravimetric analysis (TGA) and differential thermal analysis (DTA) were conducted with a Shimadzu DTG-60, displayed in Figure 28, recording data with the TA-60WS thermal Analysis Workstation (accuracy of  $\pm 1.0^\circ\text{C}$  and  $\pm 1\%$  error). TGA evaluates the vaporization characteristics and the DTA evaluates the endothermic and exothermic reactions with respect to temperature. The instrument has a Roberval mechanism to resist changes in sensitivity from thermal expansion and incorporates a highly sensitive balance that is also resistant to vibrations. TGA/DTA tests were conducted over a temperature range from about  $23^\circ\text{C}$  to  $600^\circ\text{C}$ .

These are controlled tests with a constant rate of temperature change ( $20^{\circ}\text{C}/\text{min}$ ) and a constant purging of air ( $5\text{ml}/\text{min}$ ) to simulate the environment of an internal combustion engine.

TGA measures the mass of the fuel sample to determine its vaporization characteristics, correlating to the fuels volatility, affecting the fuels spray shape and penetration into a combustion chamber of an engine. DTA analysis is conducted by measuring the absorption and release of heat compared to a reference, alumina powder, which constantly increases in temperature as the device heats up. This measurement is related to the phase changes of the sample and its reaction temperature when in a heated environment.

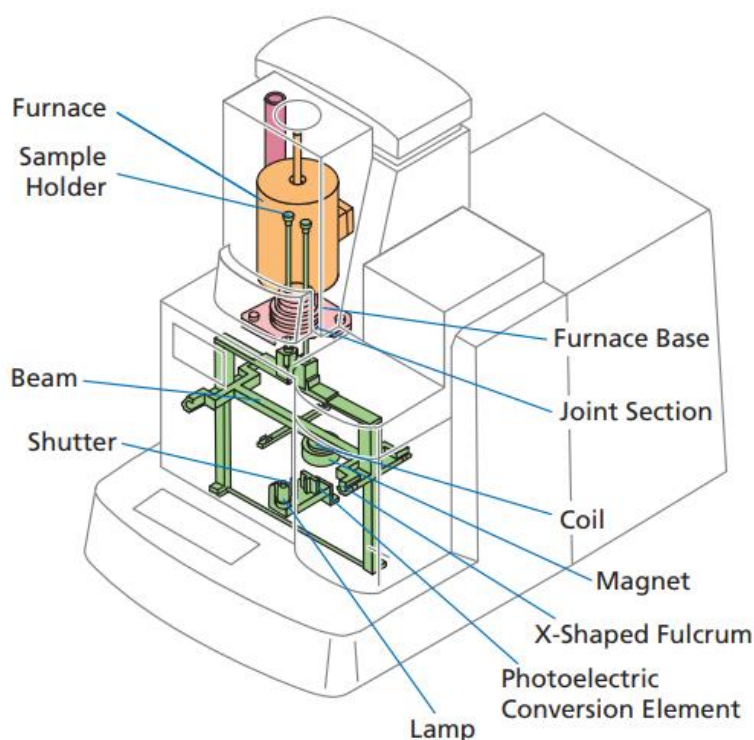


**Figure 28** DTG-60 Apparatus (Shimadzu Corporation 2012)

### ***3.4.5 Malvern Spraytec He-Ne laser***

The Malvern Spraytec He-Ne laser instrument measures the distribution of particle sizes within a spray, analyzing atomization characteristics of the experimented fuels. A schematic of the instrumental setup is displayed in Figure 29, with the primary components labeled as 1) the laser emitting transmitter, 2) collimating optics lens, 3) fuel spray droplets, 4) the focusing lens, and 5) the detector array. Atomization measurements are follow the standard BS 2955/1993 and are taken by delivering the spray through a reference pintle type fuel injector at 180 bar in between the

Transmitter and Receiver through the He-Ne laser. The detector array measures the magnitude and pattern of light that is diffracted from the spray and is processed to determine the Sauter mean diameter and droplet size distribution based on the Mie Scattering principle, assuming that the particles are perfect spheres. The Receiver lens is 300 mm consisting of 36 detectors and measures droplet sizes up to 900  $\mu\text{m}$ . Data processing is conducted in the Spraytec software, considering parameters such as the fuel density, the fuels refractive index, and properties of the surrounding environment (ambient air). Data sampling was collected at 10 kHz over a time of 5 ms, and data recording begins 0.1 ms before injection, when the transmission of light drops below 99%.

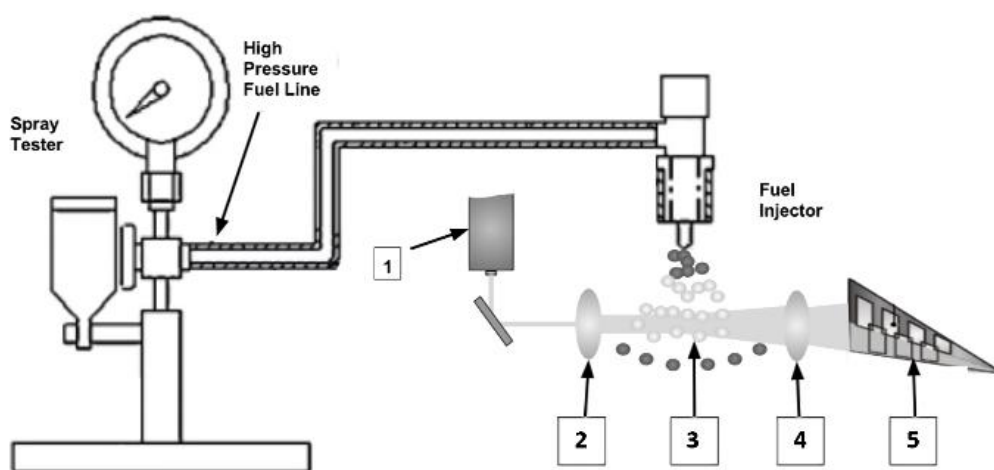


**Figure 29** Malvern Mie Scattering Setup

### 3.5 Engine Operating Procedures

Combustion research was conducted near maximum brake torque of the experimental engine at swept engine loads from 4 to 6 bar IMEP and constant speed of 1500 rpm, analyzing the effect of alternative fuels and fuel blends in RCCI mode compared to conventional diesel combustion and RCCI with standard ULSD. During engine operation, independent variables include the air/fuel ratio and volumetric efficiency through variable supercharger control and fueling strategies, and the dependent variable is in-cylinder pressure. The in-cylinder pressure data is collected for modelling of the combustion phenomena vs crank angle. Two high reactivity fuel blends were researched including a 50-50 wt-% blend of ULSD and butanol and a 50-50 wt-% blend of S8 and butanol. The blend ratio was selected to create a wide range of cetane fuels to compare in RCCI combustion. Butanol was port fuel injected at constant 60% by mass fraction across RCCI strategies.

With the fuel blends selected and engine operating conditions selected, a design of experiment was conducted for optimized NO<sub>x</sub> and soot emissions in ULSD RCCI mode. ULSD RCCI was experimented at each load for a range of fueling parameters, provided in Table VI, to determine the reference RCCI operating constraints. SOI-2 timing was chosen to vary around TDC from previous work reported in Soloiu et al. (2017), due to the low soot levels, and adjusted to maintain engine stability. PFI and SOI-1 timing were chosen based on their influence on pressure rise rates and combustion stability as well. Delaying both increased the pressure rise rates as a result of less mixing time, creating pockets of higher reactivity. The common rail pressure was investigated at a wide range, and was determined based on obtaining optimized NO<sub>x</sub>-soot tradeoff with the EGR rates.

**Table VI:** Design of Experiment for ULSD RCCI

| PFI Timing     | SOI-1 Timing | SOI-2 Timing      | Rail Pressure |
|----------------|--------------|-------------------|---------------|
| 345°-300° BTDC | 75°-40° BTDC | 5° BTDC - 5° ATDC | 400-1500 bar  |

The PFI timing was set at exhaust valve closing, 345° BTDC in combustion and the system ran at 2.76 bar. Injection timing at exhaust valve closing was chosen as it avoids scavenging of the butanol during valve overlap and offers the longest mixing time of butanol. This reduces local equivalence ratios to avoid premature ignition. Common rail injection pressures ranged from 800 to 1200 bar as load increased, mitigating the rising soot levels. DI events were split with a constant start of the first injection (SOI-1) at 60° BTDC in combustion and the start of the second injection (SOI-2) was varied around TDC at the respective loads to maintain engine stability, COV less than 5%. These parameters were initially determined for optimized emission reduction for ULSD RCCI, and maintained constant for the fuel blends to analyze the direct effects of physical and chemical fuel properties on the combustion and emissions results. With SOI-1 constant at 60° BTDC, the fuel fraction of the two DI events were adjusted to maintain constant combustion phasing for a CA50 at TDC (0° CAD), which was found to achieve low emissions and indicated thermal efficiencies up to 56%.

Boost pressures and temperatures were constant across the fuels and loads at 0.2 bar gage and 60°C respectively. With relatively low boost pressures, the intake temperature was raised to 60°C (with external heating elements) to induce higher oxidation rates of CO. EGR rates were

increased at the higher loads, starting at 20% EGR at the lowest load and 30% EGR at the two higher loads to address the direct relationship between load and NO<sub>x</sub>. A table of the selected operating parameters is provided in Table VII.

**Table VII:** Operating Parameters for CDC and RCCI

|               | <b>SOI CDC</b> | <b>SOI-1 RCCI</b> | <b>SOI-2 RCCI</b> | <b>EGR %</b> | <b>Rail Pressure</b> |
|---------------|----------------|-------------------|-------------------|--------------|----------------------|
| <b>4 IMEP</b> | 21° BTDC       | 60° BTDC          | 5° ATDC           | 20%          | 800 bar              |
| <b>5 IMEP</b> | 22° BTDC       | 60° BTDC          | 2° ATDC           | 30%          | 1000 bar             |
| <b>6 IMEP</b> | 24° BTDC       | 60° BTDC          | 1° BTDC           | 30%          | 1200 bar             |

### 3.6 Measurement Uncertainty

Uncertainty analysis of the derived output parameters of the experimental engine was calculated by determining the propagation of uncertainty of the indicated specific emissions and brake specific fuel consumption. These uncertainties arise due to equipment accuracy and calibration, and environmental conditions. Uncertainties of each measurement used to derive the indicated specific emissions and brake specific fuel consumption were evaluated and the root sum of squares of the combined measurements were calculated and averaged across the engine operating conditions. The combined uncertainty is determined with Equation 9 below where  $u_c(y)$  is the combined uncertainty,  $y$  is the computed parameter, and  $x_i$  is the measured variables. The measurement uncertainties for each parameter were around 3% and are provided in Table VIII, and the instrument accuracies are listed in Table IX.

$$u_c(y) = \sqrt{\sum_{i=1}^n \left[ \frac{\partial y}{\partial x_i} \Delta x_i \right]^2} \quad \text{Equation 9}$$

**Table VIII:** Measurement Uncertainties

| <b>NO<sub>x</sub></b> | <b>Soot</b> | <b>CO</b> | <b>UHC</b> | <b>HCHO</b> | <b>P<sub>effective</sub></b> | <b>BSFC</b> |
|-----------------------|-------------|-----------|------------|-------------|------------------------------|-------------|
| 3.13%                 | 3.35%       | 3.12%     | 3.32%      | 3.11%       | 2.90%                        | 2.89%       |



**Table IX:** Accuracy of Selected Sensor Measurements

| <b>Instrument</b>                                       | <b>Measured Parameter</b>      | <b>Accuracy</b> |
|---------------------------------------------------------|--------------------------------|-----------------|
| <b>TQ513 Torque Sensor</b>                              | Torque                         | $\pm 0.06\%$    |
| <b>Meriam Z50MC2-2 Laminar Flow Meter</b>               | Air Mass Flow Rate             | $\pm 0.72\%$    |
| <b>213 Max Flow Meter</b>                               | Common Rail Fuel Flow Rate     | $\pm 0.2\%$     |
| <b>P001 Max Flow Meter</b>                              | PFI Fuel Flow Rate             | $\pm 0.2\%$     |
| <b>Kistler 6053cc Piezoelectric Pressure Transducer</b> | In-Cylinder Pressure           | $\pm 0.19\%$    |
| <b>EMS Model 5002</b>                                   | Intake/Exhaust CO <sub>2</sub> | $\pm 0.3\%$     |
| <b>AVL SESAM FTIR V4</b>                                | NO <sub>x</sub> concentration  | $\pm 2.2\%$     |
|                                                         | CO <sub>2</sub> concentration  | $\pm 1.6\%$     |
|                                                         | CO concentration               | $\pm 1.6\%$     |
|                                                         | HC concentration               | $\pm 2.2\%$     |
|                                                         | HCHO concentration             | $\pm 2.2\%$     |
| <b>AVL 483 Micro Soot Sensor</b>                        | Soot Concentration             | $\pm 3.8\%$     |

### 3.7 Metrics for Success

The metrics for success are defined by reaching EPA regulation standards in dual fuel combustion for both NO<sub>x</sub> and soot emissions in a medium-duty non-road diesel engine. Engine out NO<sub>x</sub> emissions must be lower than 7.5 g/kWhr and particulate matter must be lower than 0.4 g/kWh without the need for exhaust aftertreatment systems.

## CHAPTER 4 ANALYSIS OF RESULTS

### 4.1 Fuel Analysis Characteristics

Various physical and chemical properties of the selected fuels investigated for this research were evaluated, providing increased understanding of the combustion and emissions characteristics. Selected fuel properties are displayed in Table X, where all were determined through experimental measurements in the lab (\*\*) except for the latent heat of vaporization (\*), which was found in literature (Lapuerta et al. 2010). Fuel analysis of the n-butanol blended fuels also included the 3% by volume biodiesel to accurately correlate these characteristics to the fuel experimented in the research engine.

The energy densities of the fuels were analyzed with a computerized Parr 1341 constant volume calorimeter providing a maximum error of 0.3%. Disregarding the energy release of steam, the lower heating value (LHV) of ULSD was the highest at 41.66 MJ/kg, and both the lower reactivity fuels had LHV values under 38 MJ/kg. The low reactivity fuel researched in this study, n-Butanol, has a LHV of 33.7 MJ/kg, which is about 20% higher than the more common alcohol based fuel ethanol, which improves fuel efficiency respectively (Alternative Fuels Data Center 2014).

**Table X:** Selected Fuel Properties [\*\*]

| Properties                                 | ULSD  | ULSD-Bu Blend | F-T S8 POSF 5109 | S8-Bu Blend | n-Butanol |
|--------------------------------------------|-------|---------------|------------------|-------------|-----------|
| <b>Density (g/cm<sup>3</sup>) @ 15°C</b>   | 0.83  | 0.82          | 0.755            | 0.783       | 0.807     |
| <b>LHV (MJ/kg)</b>                         | 41.66 | 37.94         | 41.5             | 37.84       | 33.7      |
| <b>Dynamic Viscosity @ 40°C (cP)</b>       | 2.5   | 1.77          | 1.09             | 1.45        | 2.0       |
| <b>Cetane Number (CN)</b>                  | 47.21 | 28.2          | 61.58            | 34.27       | 16.4      |
| <b>Ignition Delay (ms) (CVCC)</b>          | 3.47  | 7.97          | 2.73             | 5.71        | 40.16     |
| <b>Combustion Delay (ms) (CVCC)</b>        | 5.12  | 14.44         | 3.93             | 9.12        | 81.25     |
| <b>Latent Heat of Vaporization (kJ/kg)</b> | 233*  | -             | 339*             | -           | 595*      |

\*obtained from literature (Lapuerta et al. 2010), \*\* obtained by the authors of the study

#### 4.1.1 Fuel Viscosity

A computerized Brookfield DV II Pro rotational viscometer measured the dynamic viscosity of the fuels. The dynamic viscosity of fuel is reported as a measure of the fuels resistance to a pumping force. Measurements were conducted at a spindle speed of 200 rpm, recording the viscosity at 2°C increments from 26°C to 90°C, as displayed in Figure 30. This property influences the atomization quality, droplet velocity, and spray penetration from the fuel injector into the combustion chamber. Physical spray characteristics are especially important in reactivity controlled combustion analysis, as these properties effect fuel stratification in-cylinder. The S8-Bu fuel blend had the lowest viscosity, as neat S8 and n-butanol generally have low viscosity characteristics compared to conventional diesel. The ULSD-Bu blend and neat butanol resulted in viscosity trends that cross over at 38°C as result of synergistic effects (Lapuerta et al. 2010). From the ASTM D975 standard for ULSD#2, the viscosity at 40°C must be between 1.3-2.4 cP, which is satisfied by all fuels (Chevron Products Company 2007).

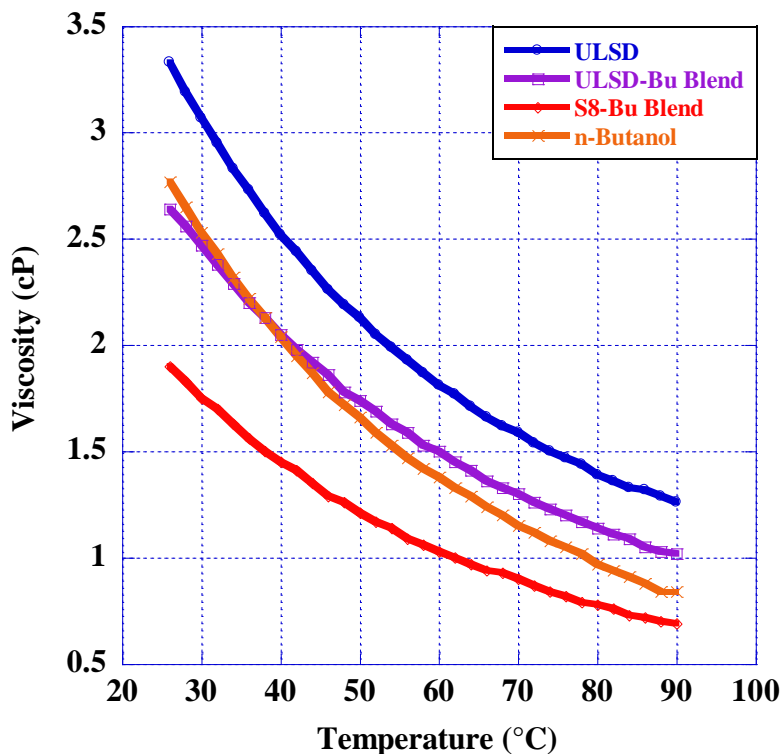
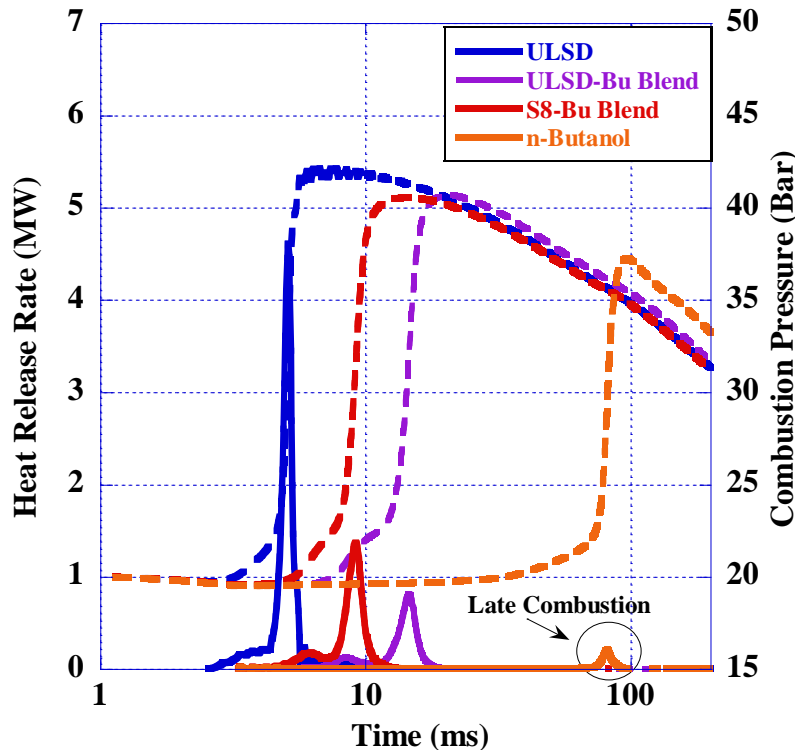


Figure 30 Dynamic Viscosity Measurements

#### 4.1.2 Ignition Quality and Negative Temperature Coefficient

The pressure and heat release rates in the constant volume combustion chamber are displayed in Figure 31 below. Neat ULSD had the highest peak pressure at 42 bar, and the two blends had the same maximum pressures at 40.5 bar due to the nearly identical energy density of the fuels. However, the peak heat release rate for the S8-Bu blend was 40% higher than the ULSD-Bu blend, even though peak pressures were the same. ULSD had the highest derived cetane number at 47.21 compared to the ULSD-Bu blend at 28.2 and the S8-Bu blend at 34.27 (S8 has a derived cetane no. of 64). The reduction in ignition quality for the fuel blends is due to the low cetane number of neat butanol, 16.4, which displays a drastically late combustion compared to the high reactivity fuels. Ignition delay and combustion delay was over two times longer for the ULSD-Bu blend and over 1.5 times longer for the S8-Bu blend compared to neat ULSD. Neat n-butanol has an extended ignition delay of 40.16 ms, which is a desirable characteristic for dual fuel combustion in the RCCI engine, as it prevents early ignition and the resulting knocking tendency and combustion instability.



**Figure 31** Pressure and Heat Release Rates in the CVCC

In the CVCC, heat release rates are exclusively dependent on the pressure rise rate. Blending butanol resulted in less rapid pressure rise rates compared to neat ULSD, reducing the peak heat release rates by 80% and 65% for the ULSD-Bu and S8-Bu blends respectively. The peak heat release rate for n-butanol is 95% lower than ULSD as a result of its resistance to autoignition. Early in the heat release rates, there is also low temperature heat release present, which is magnified in Figure 32. This low temperature heat release corresponds to a negative temperature coefficient (NTC) as a result of the intermediate temperature oxidation paths of the fuels. Depending on the molecular structure, the oxidation rate decreases at intermediate temperatures (700-900K). This NTC region displays correlations with the cetane number of the fuels, where the higher cetane number increases the NTC magnitude, but reduces the duration of this region. As a result of the extended NTC for the blended fuels, there is less fuel to ignite at the time of the HTHR, reducing peak energy release rates.

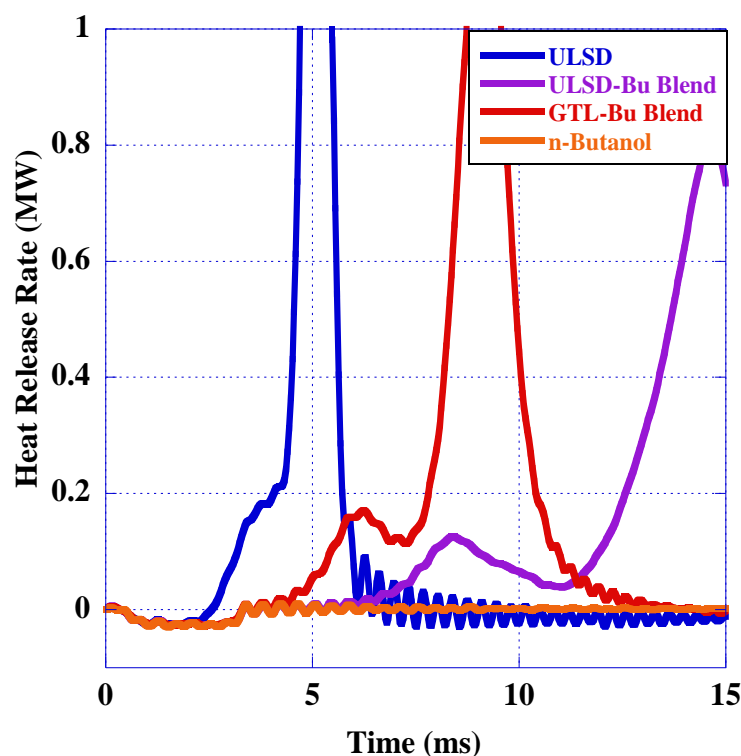


**Figure 32** Negative Temperature Coefficient Region in the CVCC

#### 4.1.3 Thermogravimetric and Differential Thermal Analysis

TGA results are displayed in Figure 33 and the characteristic temperatures at which 10%, 50%, and 90% of the fuel is vaporized (TA10, TA50, and TA90) are listed in Table XI below.

TGA analysis reflects the volatility of the fuel with respect to temperature, where liquid fuel does not start mixing with the surrounding air until it is in its gaseous state. ULSD is the least volatile, at which it does not start vaporizing (TA10) until 115°C and is almost completely vaporized (TA90) at 250°C. The butanol blended ULSD and S8 display a two stage TGA result; the butanol is initially vaporized followed by the vaporization of the high reactivity fuel. The lower vaporization temperatures of the blended fuels compared to ULSD are beneficial in the engine for earlier mixing of the fuel and air for reduced wall wetting in the chamber due to decreased spray penetration of the liquid jet.

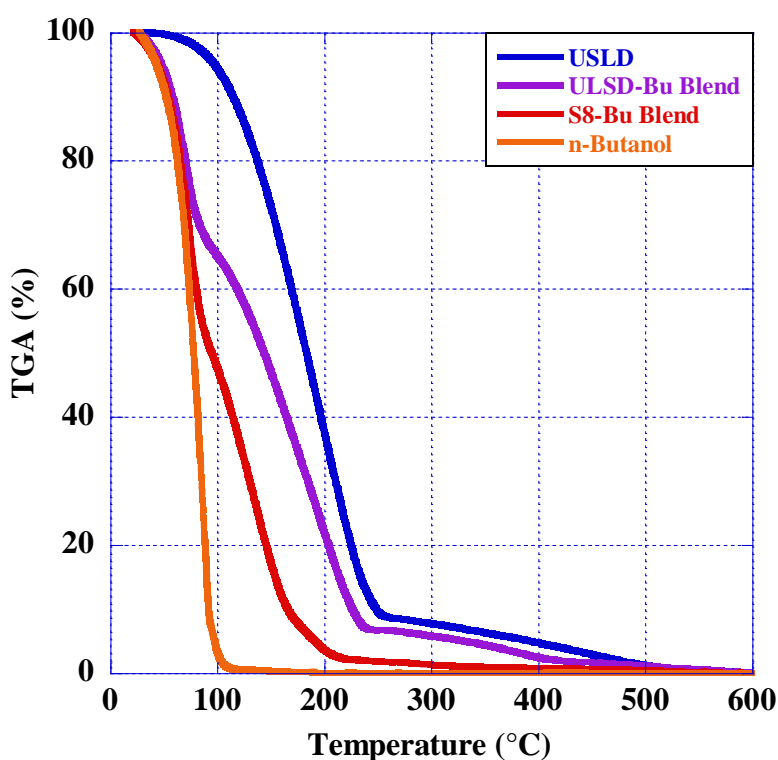


**Figure 33** Thermogravimetric Analysis

**Table XI:** Characteristic Vaporization Temperatures

|                      | TA10   | TA50   | TA90   |
|----------------------|--------|--------|--------|
| <b>ULSD</b>          | 115 °C | 185 °C | 250 °C |
| <b>ULSD-Bu Blend</b> | 58 °C  | 144 °C | 226 °C |
| <b>S8-Bu Blend</b>   | 54 °C  | 95 °C  | 166 °C |
| <b>n-Butanol</b>     | 52 °C  | 78 °C  | 92 °C  |

DTA analysis measures the energy release profile from low temperature heat release when exposed to increasing temperatures. The endothermic reactions are displayed by the negative slopes and exothermic reactions are reflected by the positive slopes presented in differences of microvolts per milligram, as displayed in Figure 34. The energy release of the fuels is split into two stages starting with the initial reaction due to oxidation and a high temperature reaction as a result of pyrolysis. The high latent heat of vaporization of butanol, 595 kJ/kg, is evident by the large initial endothermic reaction, which is then released when the fuel is almost completely vaporized (TA90). This property of n-butanol is beneficial for reducing in-cylinder gas temperatures in the experimental engine, absorbing a high amount of heat energy in order to vaporize. The initial endothermic reaction of the S8-Bu blend is larger than that of the ULSD-Bu blend because neat S8 has a higher latent heat of vaporization than ULSD, 340 kJ/kg. The concave minimum for the S8-Bu blend occurs 5°C before TA50, followed by a second energy release at TA90. The ULSD-Bu blend follows a similar trend; however it is more gradual due to the lower rate of vaporization compared to S8. The pyrolysis reaction for each fuel correlates to the remaining fuel vapor in the furnace at high temperatures.

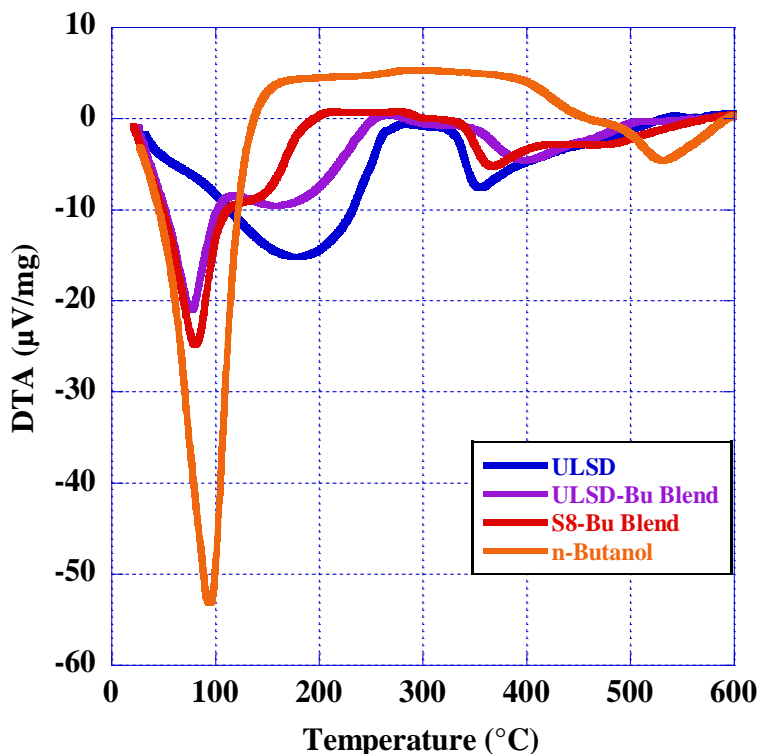


**Figure 34** Differential Thermal Analysis

#### ***4.1.4 MIE Scattering Spray Analysis***

Spray analysis was conducted for the high reactivity fuels used in the common rail fuel injection system and not n-Butanol because butanol is the exclusive fuel for indirect injection and these characteristics are less significant in port fuel injection systems. Figure 35 displays the Sauter Mean Diameter (SMD) over time and the volume frequency distribution of the droplet diameter of neat ULSD, and the two butanol blends. The atomization results for each fuel across time display similar results. This is assumed to be a result of the reduced butanol blend densities compared to neat ULSD, where the force exerted on the hydraulic injector is lowered causing a less atomized fuel spray. The average SMD for the S8-Bu blend was the lowest however. Peak volume frequency distributions indicate the droplet size that is the most prevalent. This peak is around 35  $\mu\text{m}$  at 8% for ULSD, 40  $\mu\text{m}$  at 7% for the ULSD-Bu blend, and 35  $\mu\text{m}$  at 7% for the S8-Bu blend. The higher percentage of lower droplet sizes for the S8-Bu blend is desirable, along with its high volatility and low viscosity, for reduced spray velocities and penetration in-cylinder directly from the injector nozzle. Table XII lists the particle size by volume including  $D_v(10, 50, \text{ and } 90)$ , which are the largest droplet SMD for 10%, 50%, and 90% of the spray volume and the percent spray volume under 10  $\mu\text{m}$ . The droplet distribution for the S8-Bu blend is lower than the other fuels, as its overall volatility is higher.



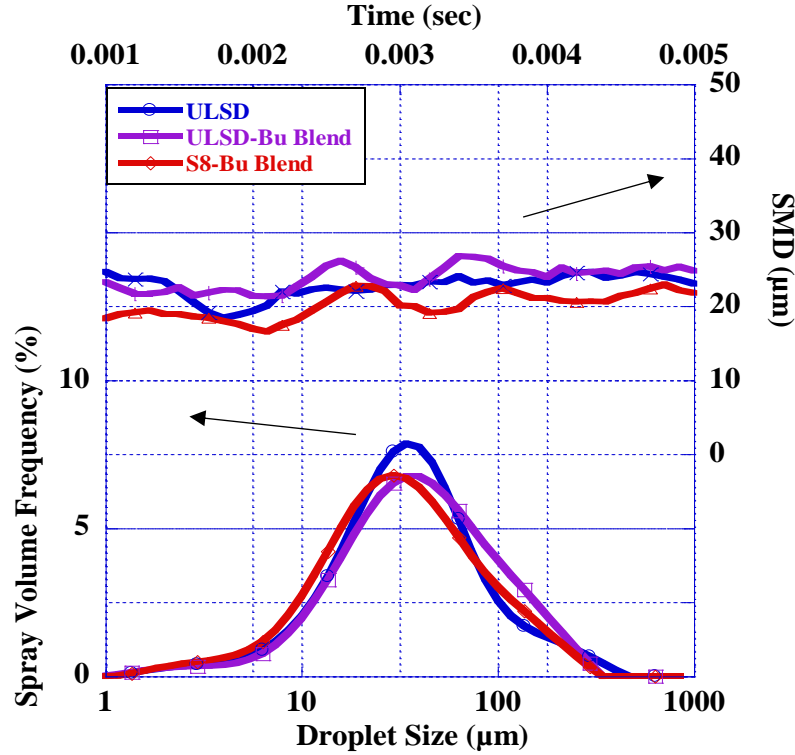


**Figure 35** Sauter Mean Diameter and Droplet Frequency Distribution

**Table XII:** Particle Size Distribution by Volume ( $\mu\text{m}$ )

|                      | Dv (10) | Dv (50) | Dv (90) | SMD  | %v < 10 $\mu\text{m}$ |
|----------------------|---------|---------|---------|------|-----------------------|
| <b>ULSD</b>          | 12.3    | 37.9    | 120.5   | 22.8 | 9.5                   |
| <b>ULSD-Bu Blend</b> | 12.9    | 42.2    | 135.1   | 24.3 | 8.6                   |
| <b>S8-Bu Blend</b>   | 10.5    | 34.4    | 116.6   | 20.8 | 12.2                  |

## 4.2 Thermodynamic Combustion Analysis

Engine operating conditions were chosen to be near maximum brake torque of the experimental engine, at 1500 rpm and loads from 4 to 6 bar IMEP. Split DI events were implemented to create reactivity and fuel concentration gradients in the combustion chamber. Table XIII lists the mass fraction and pulse width of the single injection event in CDC and the first direct injection event in RCCI, varying for each fuel at the respective load due to the differences in autoignition quality and energy density. The DI mass fractions in RCCI were chosen to maintain constant combustion phasing, CA50, with constant SOI-2 for each fuel at the respective load. The common rail injection patterns and pulse widths are presented in Figure 36, displaying the differences in injection durations for the three RCCI modes. Figure 37 displays the

global equivalence ratios ( $\Phi$ ), relative fuel/air ratio, before and after SOI-2 for the experimental research points. With nearly half of the combustion duration occurring prior to SOI-2, the global equivalence ratio during this time provides further correlations of the combustion characteristics.

**Table XIII:** Injection Duration (ms) and Mass Fraction of the First DI Event (%)

|                     | 4 IMEP      | 5 IMEP      | 6 IMEP      |
|---------------------|-------------|-------------|-------------|
| <b>CDC</b>          | 0.715 / -   | 0.760 / -   | 0.840 / -   |
| <b>ULSD RCCI</b>    | 0.275 / 58% | 0.250 / 51% | 0.235 / 45% |
| <b>ULSD-Bu RCCI</b> | 0.380 / 79% | 0.350 / 73% | 0.310 / 57% |
| <b>S8-Bu RCCI</b>   | 0.345 / 68% | 0.340 / 68% | 0.320 / 57% |

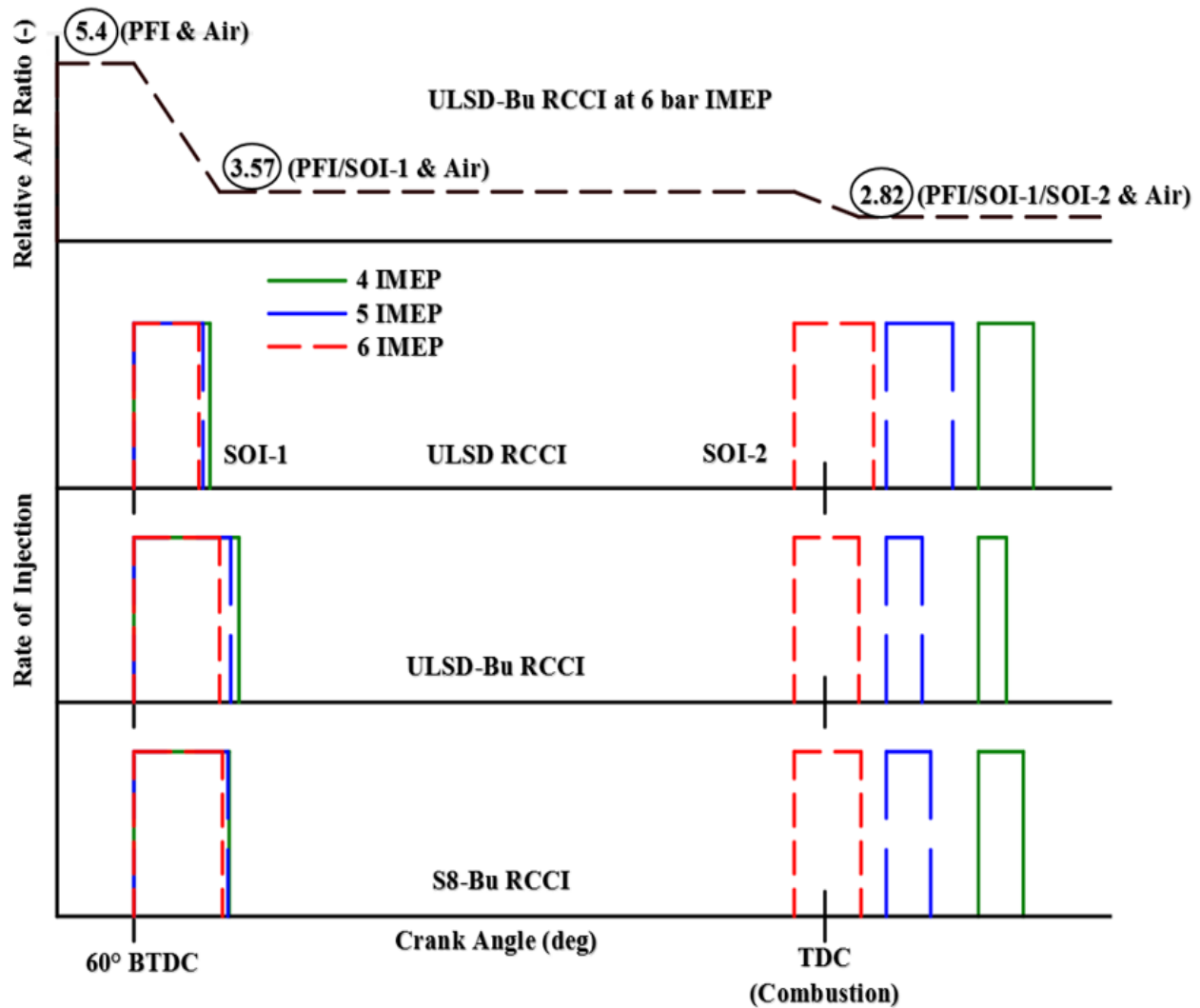


**Figure 36** Multi-Pulse Injection Pattern

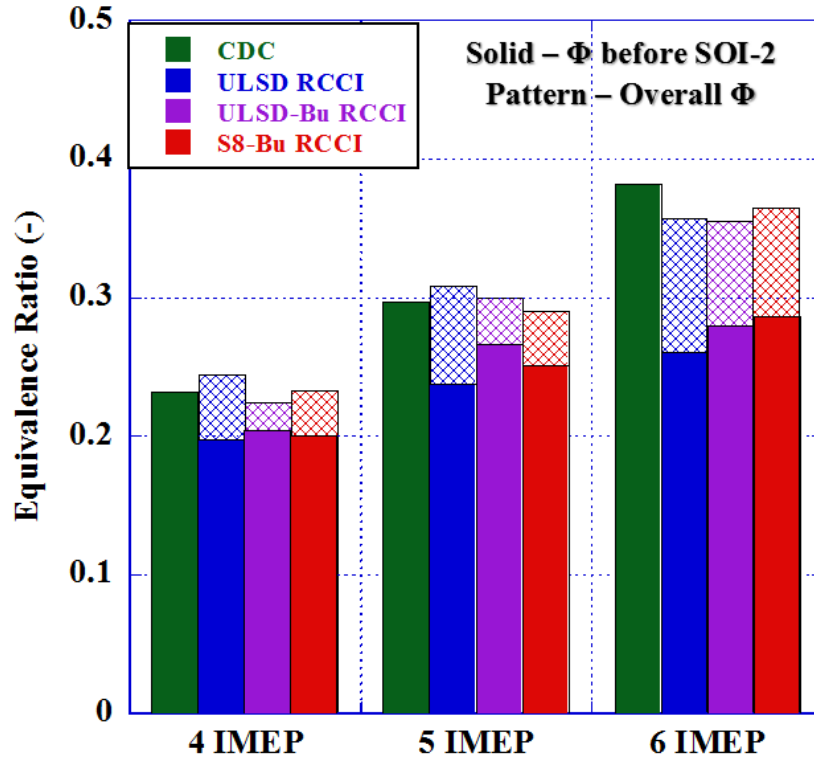


**Figure 37** Global Equivalence Ratio before and after SOI-2

#### 4.2.1 In-Cylinder Combustion Pressure

In-cylinder pressure traces are displayed in Figures 38 and 39. Dual fuel combustion was delayed compared to CDC from the 60% PFI fraction of n-butanol, as seen in the extended combustion delay for butanol in the CVCC. Peak pressures for ULSD RCCI were the same as CDC; however RCCI with the blended fuels increased peak pressures between 5 and 10 bar. The mass fraction of the first DI event for the blended fuels was 10% to 20% more compared to neat ULSD, increasing the global equivalence ratio in the cylinder at the time of premixed combustion. Similarities in the peak pressure for the fuel blends are also witnessed in the CVCC pressure data. At 6 bar IMEP, a slight inflection at peak pressure is present in ULSD-Bu and S8-Bu RCCI as a result of the higher fraction of the second injection compared to ULSD RCCI. This is observed in the butanol fuel blends because of the cooling effect taking place from the DI butanol fraction.

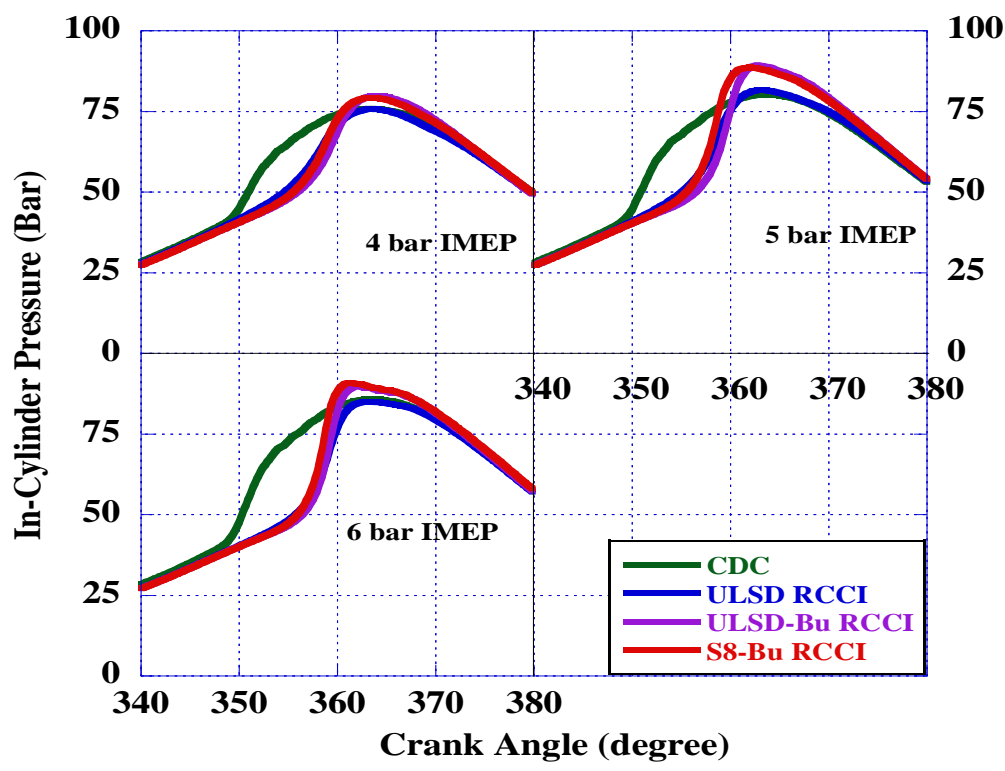


Figure 38 In-Cylinder Combustion Pressures

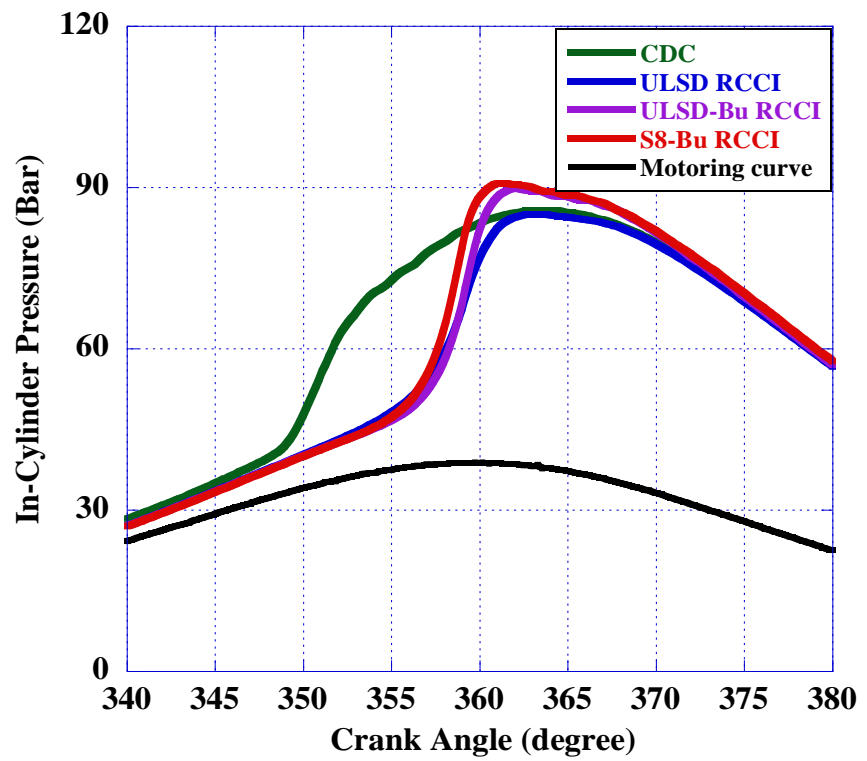
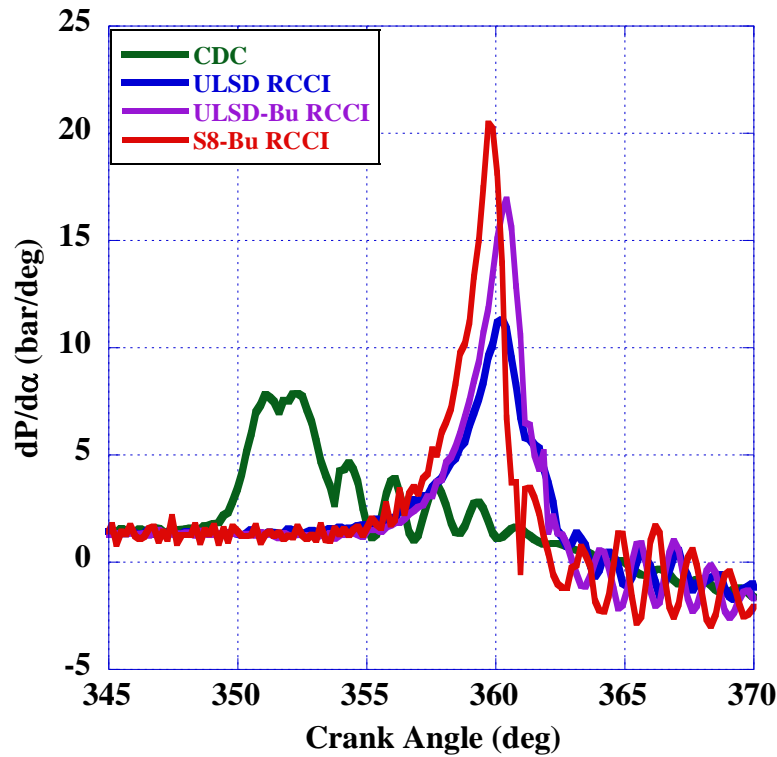


Figure 39 In-Cylinder Combustion Pressures at 6 Bar IMEP

Maximum pressure rise rates for RCCI combustion increased compared to CDC, as displayed in Figure 40. Butanol delayed the initial rise in pressure to near 3° BTDC, where there was a drastic rise in pressure to peak values. RCCI for the butanol blends increased MPRR between 30-40% compared to ULSD RCCI. MPRR reached 15 bar/deg and 20 bar/deg at 5 and 6 bar IMEP respectively for S8-Bu RCCI, surpassing the generally accepted limit of 15 bar/deg. The uncontrollable pressure rise rates are attributed to smaller reactivity gradients at the time of combustion with high fractions of SOI-1, as reported by Li et al. (2015). To achieve reductions in MPRR, later combustion phasing would be required through lower SOI-1 fractions or high EGR rates, however, to study the effects of different fuels, combustion phasing was used as a control variable.



**Figure 40**  $dP/d\alpha$  at 6 Bar IMEP

#### 4.2.2 Apparent Heat Release Rates

The apparent heat release rates (AHRR) were derived assuming a closed system after intake valve closing with the model given in Equation 10, where  $Q$  is energy in Joules,  $\Theta$  is crank angle degree,  $\gamma$  is the specific heat capacity of air,  $V$  is cylinder volume in liters, and  $P$  is combustion pressure in bar. The model assumed the working fluid is homogeneous and acts as an ideal gas and

has a constant average specific heat ratio during the compression and exhaust strokes. Crevice flow and blow by were disregarded, resulting in a 2% underestimation of the overall air/fuel mass. Net apparent heat release rates are displayed in Figures 37 and 38, which do not consider heat transfer to the cylinder liner, cylinder head, or piston.

$$\frac{dQ}{d\theta} = \frac{1}{(\gamma-1)} V \frac{dP}{d\theta} + \frac{\gamma}{(\gamma-1)} P \frac{dV}{d\theta} \quad \text{Equation 10}$$

Two stage heat release rates are observed for all fueling strategies across the three loads, as displayed in Figures 41 and 42. CDC displays a more rapid premixed heat release compared to RCCI, however, the magnitude is much lower, as also seen by Chen et al. (2013). CDC also burns with a much longer diffusion flame than the duel fuel modes from less mixing and more regions of high local equivalence ratios above the flammability limit. In-cylinder stratification of butanol delays the premixed flame by reducing the overall reactivity of the air/fuel mixture prior to the SOI-2 event, occurring around TDC. Peak apparent heat release rates for the butanol blends increased by 30% at 4 and 6 bar IMEP compared to ULSD RCCI. This is attributed to the lower ignition quality, requiring higher mass fractions of the first injection for the butanol blends to maintain combustion phasing. The larger SOI-1 fraction created richer fuel zones at the time of combustion, leading to high heat release rates and higher local temperatures as explained by Mikulski and Bekdemir (2017). In addition, butanol has high volatility, as seen in the TGA/DTA analysis previously discussed, increasing the amount of vaporized fuel conditioned for combustion at the time of the premixed flame. S8-Bu RCCI advanced the peak AHRR compared to ULSD-Bu RCCI from a higher cetane number. Peak AHRRs for S8-Bu RCCI were lower than ULSD-Bu RCCI at the two lower loads for the S8 blend, where it gradually increased with load and was 10% higher at 6 bar IMEP. This trend is seen to result from the mass fraction of the first DI event. As load increased, the  $\Phi_{\text{global}}$  prior to SOI-2 was higher for S8-Bu RCCI compared to ULSD-Bu RCCI, increasing the rate of heat release.

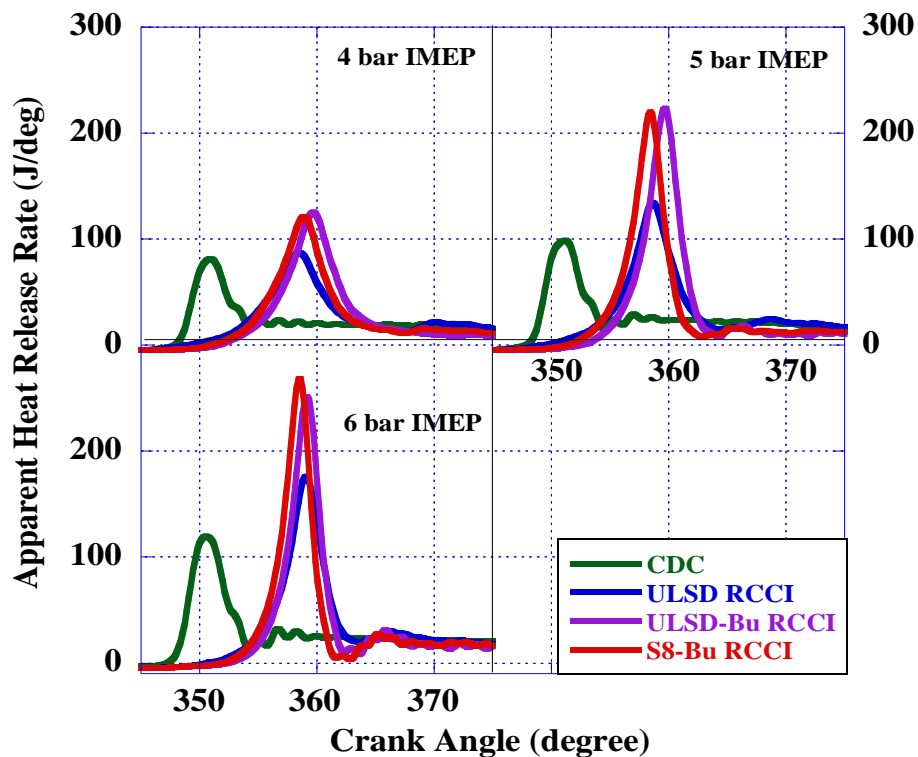


**Figure 41** Apparent Heat Release Rates

The mixing controlled diffusion flame is greatly shortened for the dual fuel modes compared to CDC. PFI of the low reactivity fuel delayed the heat release in dual fuel combustion, at which point more fuel was premixed with the charge air. The heat release from the second flame increased in magnitude with load, where larger fractions of fuel are injected in the second injection to maintain the power demand. For ULSD RCCI, the diffusion flame was noticeably larger at low load compared to the butanol blends; however at the highest load the magnitude was similar across the three RCCI modes and CDC. Both S8 and butanol have high latent heat of vaporization properties, causing the heat release to reach a lower concave minimum for S8-Bu RCCI and to a lesser extent for ULSD-Bu RCCI. For the fuel from the second DI event to vaporize, it must absorb this energy to produce the second flame.

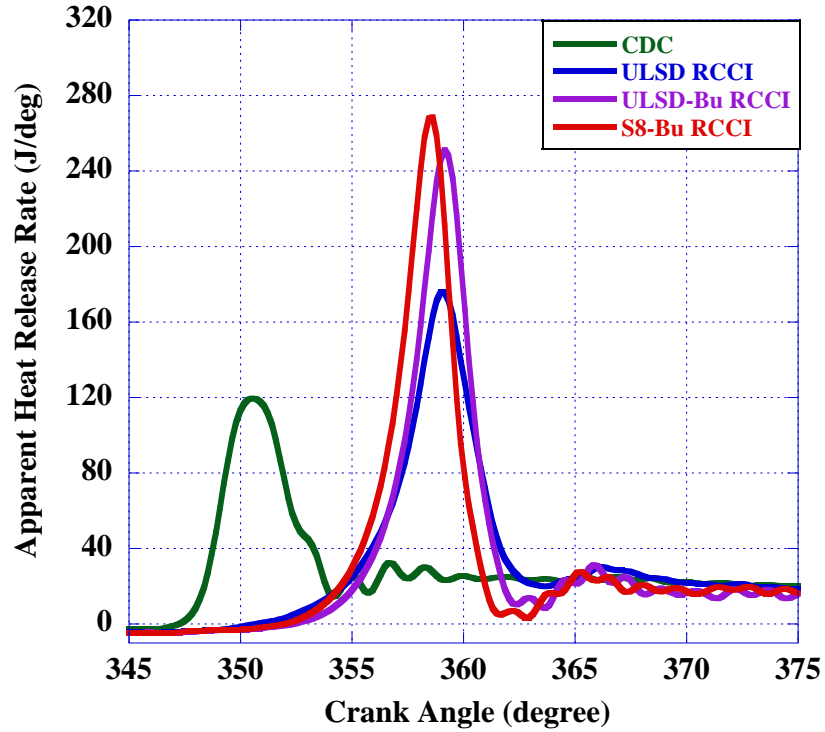


**Figure 42** Apparent Heat Release Rates at 6 Bar IMEP

#### ***4.2.3 Mass Fraction Burned***

The mass fraction burned results were derived from integrating the net heat release rates to analyze combustion phasing and duration. Figures 43 and 44 display the mass burned across engine loads and at the highest load respectively. Crank angle at which 10%, 50%, and 90% (CA10, CA50, and CA90) of the burned mass are used for defining ignition delay (ID), combustion phasing, and combustion duration (CD). In this paper, ignition delay is defined as the start of injection (at SOI-1) to CA10. Combustion phasing was maintained at  $360 \text{ CAD} \pm 2^\circ$ , and combustion duration is defined as the crank angle interval from CA10 to CA90.



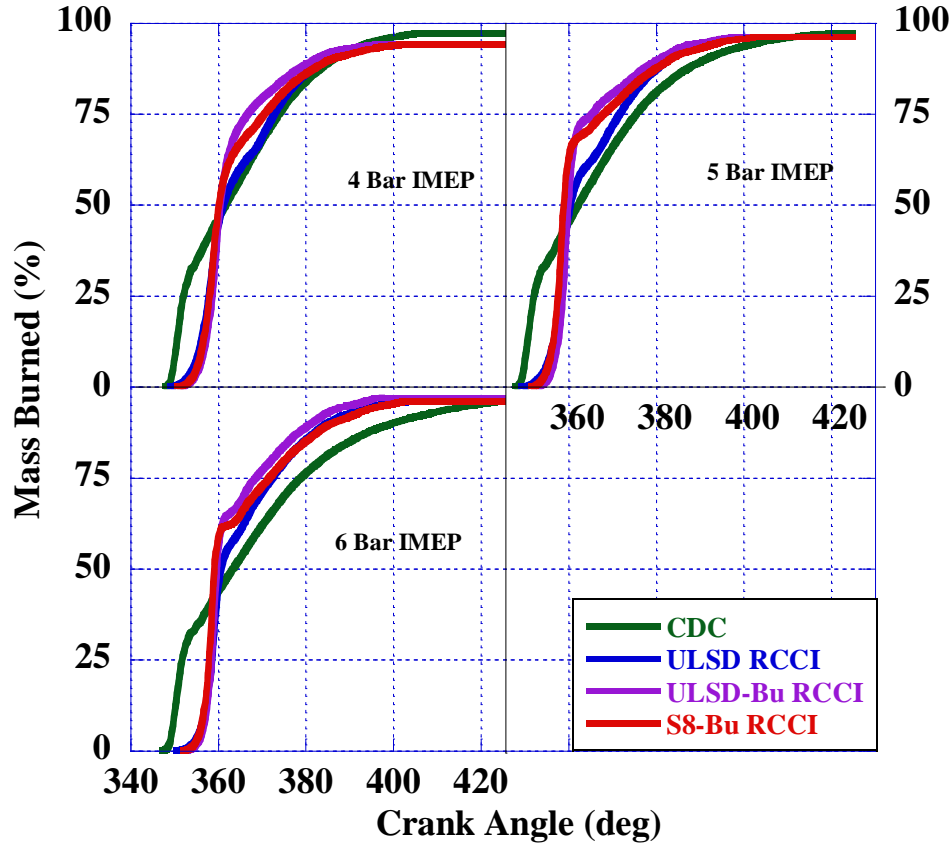


**Figure 43** Mass Burned Across Engine Loads

The given definition for ignition delay does not accurately represent a comparison between CDC and RCCI, where CA10 for CDC was reached  $7^\circ$  earlier than the dual fuel modes. Ignition delay and combustion duration for the research points are provided in Table XIV. Ignition delay for RCCI combustion was similar for each fuel at the three loads. The differences in cetane number for the high reactivity fuels did not have an effect on the ID, which is also evident in the heat release rates because of the constant PFI fraction and combustion phasing. Ignition for all three RCCI modes began at around the same time,  $\pm 0.1$  ms, where the premixed flame is initiated. An inflection in the mass burnt is present at SOI-2 for all dual fuel modes due to cooling of the liquid jet. The inflection is strongest for S8-Bu RCCI because of the high latent heat of vaporization of this fuel blend.

Combustion duration was reduced up to 2.5 ms for ULSD RCCI compared to CDC, and was further reduced with the ULSD-butanol blend. Lower cetane fuels are generally desired for premixed combustion to extend mixing time and induce shorter combustion durations. This was

achieved with ULSD-Bu RCCI, CN 28.2, with CD 15% shorter than ULSD RCCI at each load. S8-Bu RCCI has a 30% lower ignition quality than neat ULSD, however, combustion durations were the same at the two lower loads, and was extended by 0.2 ms at 6 bar IMEP for S8-Bu RCCI. The extended CD is a result of the higher volatility and smaller droplet sizes of S8-Bu RCCI compared to ULSD, creating lower reactivity gradients and promoting a less complete combustion (Mikulski and Bekdemir 2017).

**Table XIV:** Ignition Delay and Combustion Duration across Engine Loads

| ID / CD (ms)      | CDC       | ULSD RCCI  | ULSD-Bu RCCI | S8-Bu RCCI |
|-------------------|-----------|------------|--------------|------------|
| <b>4 Bar IMEP</b> | 1.3 / 4.0 | 6.2 / 3.25 | 6.3 / 2.8    | 6.25 / 3.3 |
| <b>5 Bar IMEP</b> | 1.4 / 4.6 | 6.25 / 3.0 | 6.4 / 2.6    | 6.25 / 3.0 |
| <b>6 Bar IMEP</b> | 1.6 / 5.6 | 6.3 / 3.1  | 6.4 / 2.7    | 6.3 / 3.3  |

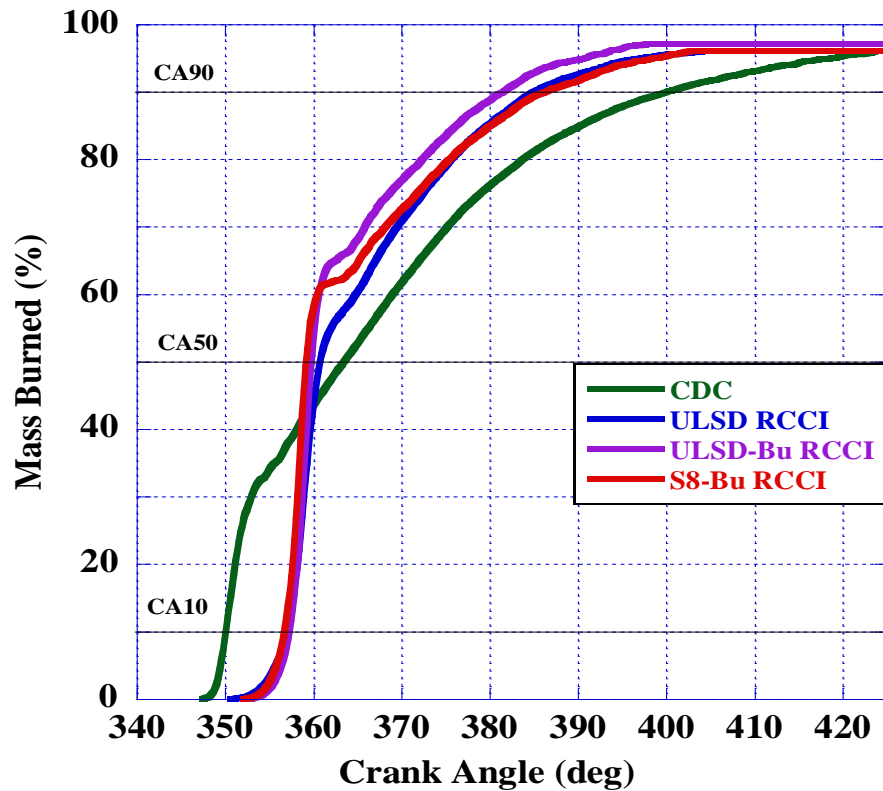


**Figure 44** Mass Burned at 6 Bar IMEP

#### 4.2.4 Instantaneous Volume-Averaged Gas Temperature

The instantaneous volume-averaged gas temperatures, Figures 45 and 46, were derived from the in-cylinder pressure and volumetric efficiency with respect to piston movement assuming

an ideal gas mixture. RCCI combustion results display operating characteristics in low temperature combustion regimes below  $1600^{\circ}\text{C}$  (Neely et al. 2005). ULSD RCCI had the lowest combustion temperatures compared to RCCI with the butanol blends, correlating to the lower peak heat release rates. Increases in peak temperatures for the butanol blends is attributed to the larger SOI-1 fractions, which increases the mixing time for a larger portion of the demanded fuel, increasing combustion temperatures. Peak temperatures for S8-Bu RCCI were  $25^{\circ}\text{C}$  lower than ULSD-Bu RCCI at 4 and 5 bar IMEP, and the same at 6 bar IMEP, reaching  $1560^{\circ}\text{C}$ . The higher latent heat of vaporization of S8 compared to ULSD is attributed to this trend, shifting the higher peak AHRR for S8-Bu RCCI at the highest load. The fuel characteristics of S8 along with the larger SOI-1 fraction reduces fuel stratification, creating richer combustion zones with higher heat release rates and combustion temperatures. An inflection at the highest load is also present for the butanol blends near TDC, which is consistent with the combustion pressures and mass burned results. The liquid jet of butanol blends initially cools the cylinder during the second DI event, followed by the reinitialized diffusion flame and continued rise in temperature.

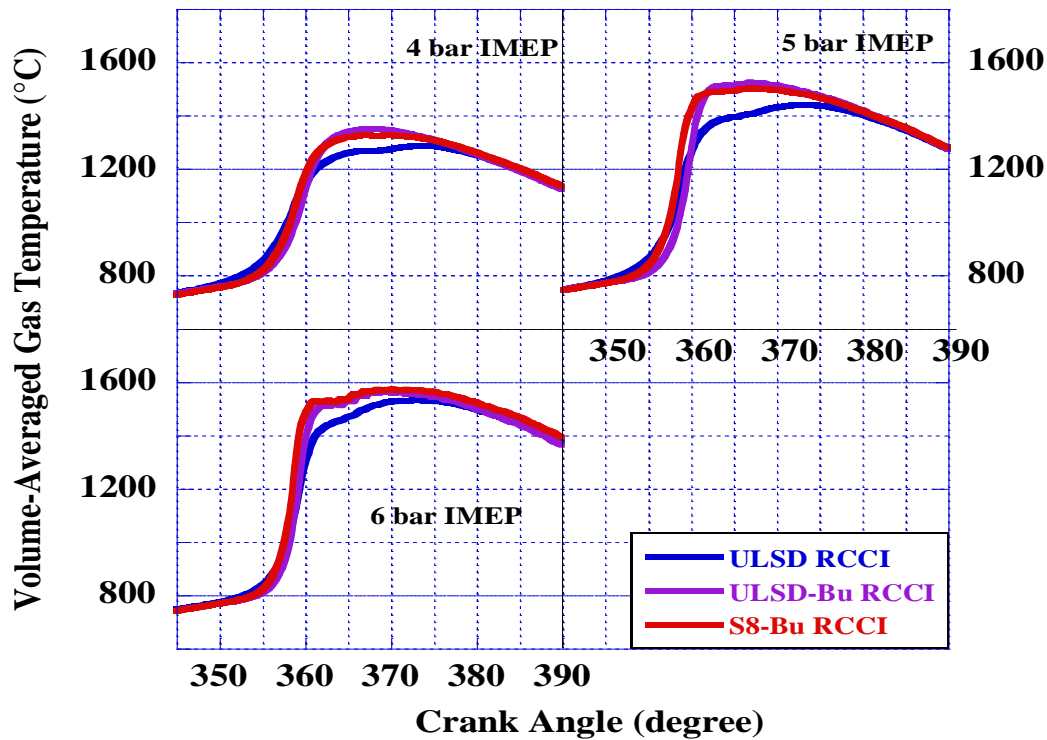


**Figure 45** Instantaneous Volume-Averaged Gas Temperatures

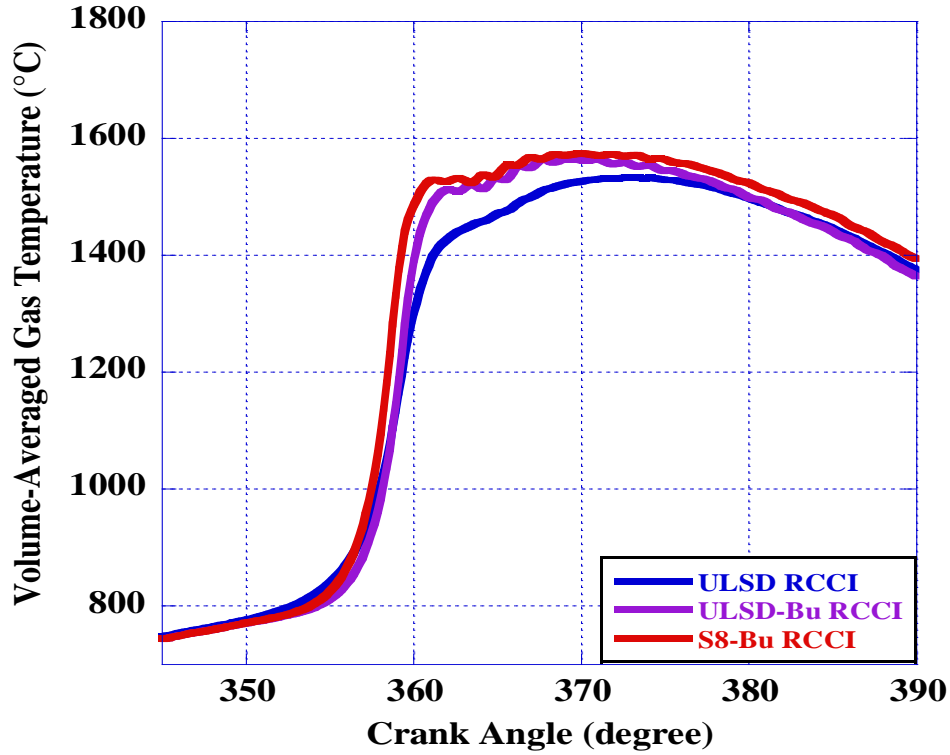


**Figure 46** Instantaneous Volume-Averaged Gas Temperatures at 6 Bar IMEP

#### 4.2.5 Ringing Intensity

Combustion ringing intensity was calculated with Equation 11 using the derived peak cylinder temperatures, MPRR, and the empirical constant  $\beta = 0.05$ , commonly used in various combustion studies (J.A. Eng 2002) relating the amplitude of pressure oscillations.

$$RI = \frac{\left(\beta \left(\frac{dP}{dt}\right)_{\max}\right)^2}{2\gamma P_{\max}} \sqrt{\gamma R T_{\max}} \quad \text{Equation 11}$$

Ringing intensity is displayed in Figure 47. At the lowest load, RI for ULSD RCCI was 30% lower compared to CDC and 55% higher at 6 bar IMEP. At the lower load, the pressure rise rate was much more gradual for this RCCI mode, as seen in the pressure traces and apparent heat release rates. This is due to the smaller fuel demand, creating an over-lean mixture. The butanol blends increased ringing intensity drastically at the higher loads, with increases of up to 80% and 85% for ULSD-Bu RCCI and S8-Bu RCCI respectively compared to CDC. Increases in ringing intensity are a result of reductions in reactivity gradients and fuel stratification due to PFI of n-butanol and larger mass fractions of SOI-1 compared to ULSD RCCI (Xiao et al. 2018). Soloiu et

al. (2015) also observed increases in ringing intensity as the ratio of blended butanol in ULSD increased due to the more homogeneous mixture induced.

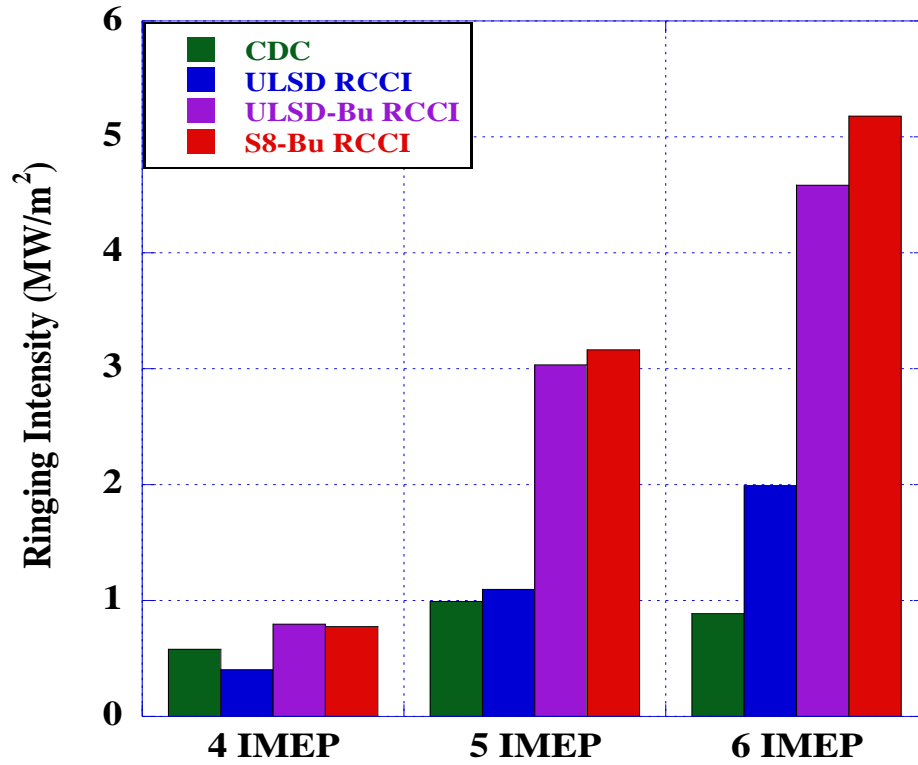


**Figure 47** Combustion Ringing Intensity

#### 4.2.6 Heat Flux and Heat Losses

Combustion heat fluxes and heat losses were derived to evaluate the interaction of the combustion gases and flames in dual fuel mode with the combustion chamber walls. Heat fluxes were model based on work by Borman and Nishiwaki (1987), with further revisions by Soloiu et al. (2013). The heat flux model is provided in Equation 12, where  $\lambda_A$  an empirically calculated thermal conductivity value on a crank angle basis,  $T_A$  is the calculated combustion temperature,  $T_W$  is an assumed uniform wall temperature of 500°C,  $\sigma$  is the Stefan Boltzmann constant, and  $\epsilon$  is emissivity of a blackbody. The derived Reynolds number (Re) is provided in Equation 13, where  $\mu(\alpha)$  the instantaneous air velocity,  $\rho$  is the gas density, and  $S$  is the engine speed. Calculations used an empirically calculated thermal conductivity of air ( $\lambda_A$ ) and assumed an average uniform wall temperature ( $T_W$ ) of 500°C.

$$\mathbf{q}(\alpha) = A \frac{\lambda_A(\alpha)}{D} \mathbf{Re}^{0.7} (T_A(\alpha) - T_w) + \sigma * \epsilon (T_A^4(\alpha) - T_w^4) \quad \text{Equation 12}$$

$$\mathbf{Re}(\alpha) = \rho(\alpha) \frac{S * N * D}{30\mu(\alpha)} \quad \text{Equation 13}$$

Heat fluxes for CDC and the three RCCI modes at 6 bar IMEP are displayed in Figure 48. Total flux (solid line) is a combination of the convection flux (dashed lines) caused by direct contact of the in-cylinder gas and combustion chamber and the radiation flux (dotted lines) due to high temperature burned gases and particulate matter (Benajes et al. 2015). Peak convection flux was 10% higher for the n-butanol blends compared to CDC and 7% higher compared to ULSD RCCI. The increase is attributed to the high mass fraction of SOI-1 creating homogenous air/fuel mixtures and high heat release rates. High heat release rates coupled with high local temperatures are the main reasons for heat transfer losses (Mikulski and Bekdemir 2017). The high vaporization rate of n-butanol also increased this convection flux, causing higher droplet temperatures and vapor pressures, especially for the DI of butanol blend cases. Radiation flux correlates to the intensity of the diffusion burn. From the apparent heat release, ULSD-Bu RCCI and S8-Bu RCCI had the deepest inflections between the premixed and mixing-controlled phases, rising to similar magnitudes. Soot radiation in RCCI has been found to increase in magnitude with respect to the fuel rich locations prior to ignition (Tang et al. 2017), such as the case for the butanol blends with higher SOI-1 fractions producing richer pockets. Dual fuel combustion with the butanol blends increased the radiation flux by 10% and 22% compared to ULSD RCCI and CDC respectively.

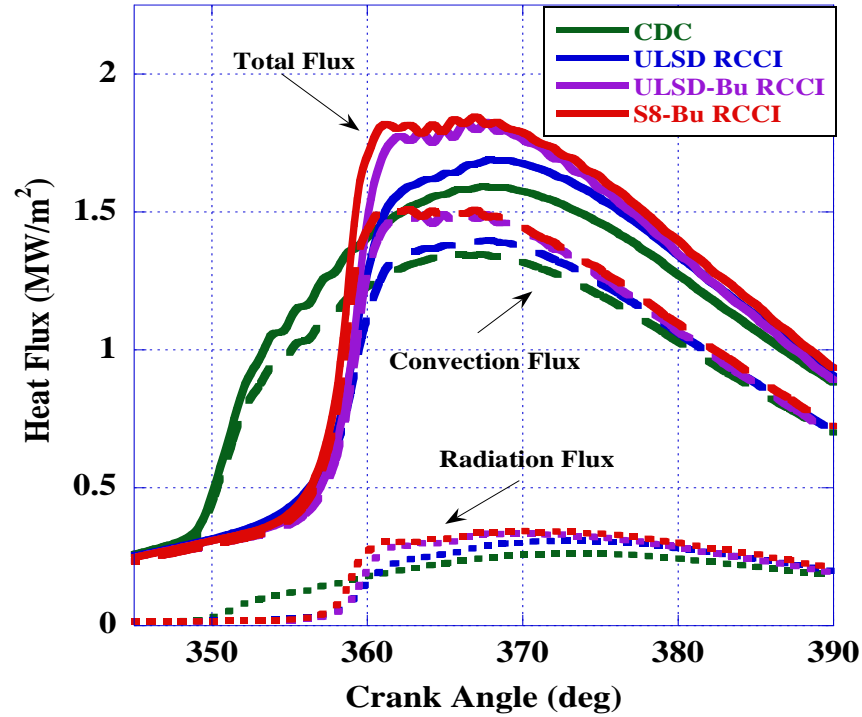


**Figure 48** Heat Flux at 6 Bar IMEP

Figure 49 represents the allocation of the total fuel energy at 6 bar IMEP regarding net heat release, crevice effects, convection and radiation for RCCI combustion. Crevice effects are estimated to be 2% of the net heat release due to gas flows in and out of these volumes. Combustion efficiency was highest for ULSD-Bu RCCI at 97% due to more optimal fuel stratification with the respective parameters and the shortest combustion durations. The used net heat release for ULSD-Bu RCCI was highest compared to the other RCCI modes due to the much higher heat release rates compared to ULSD RCCI and less rapid and shifted heat release rate compared to S8-Bu RCCI. Convective heat losses for S8-Bu RCCI is 2% higher compared to the diesel RCCI modes, in which the injection durations are longer due to the lower density, increasing spray penetration and wall impingement.

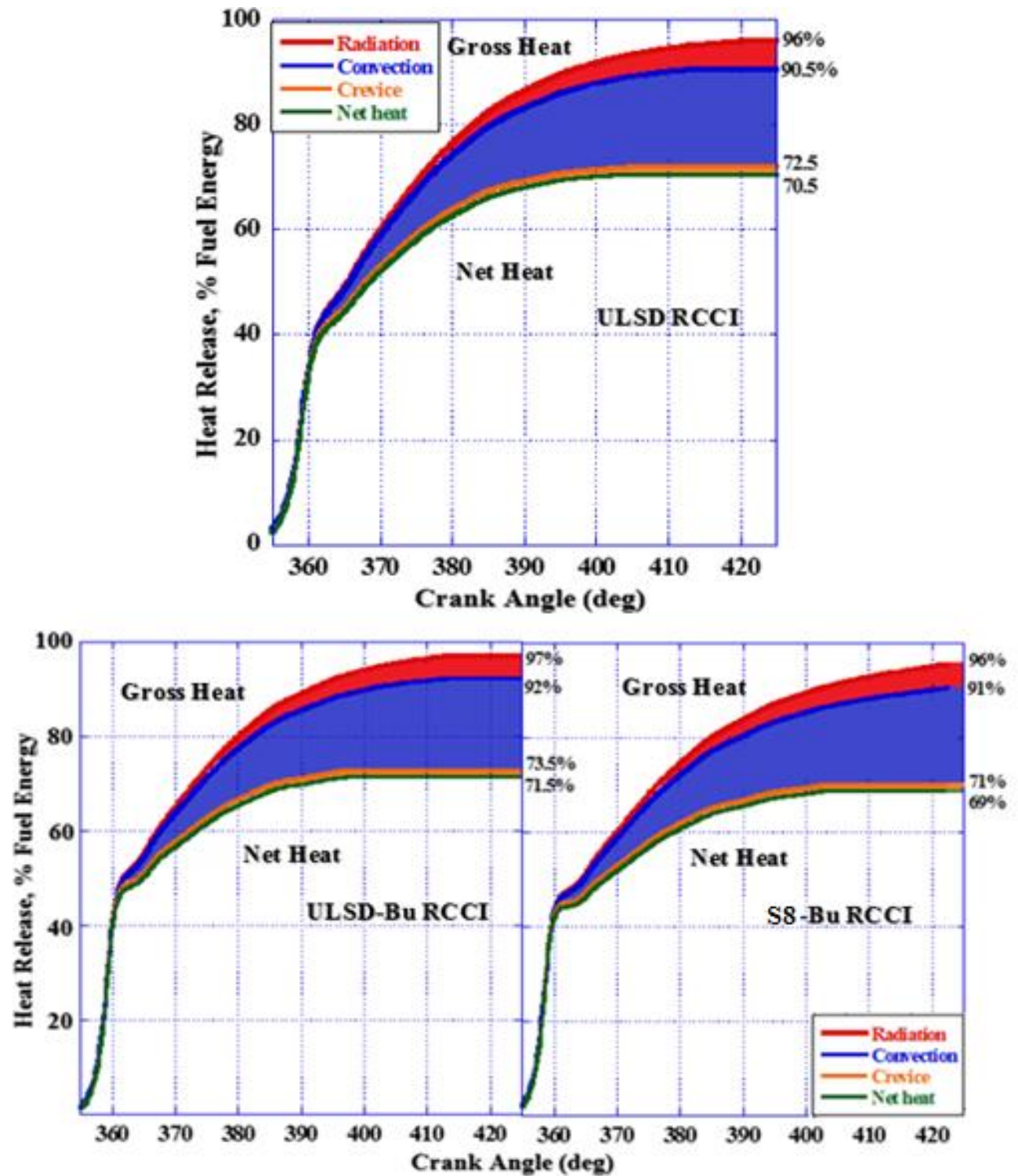


Figure 49 Heat Losses Based on Energy Balance



### 4.3 Exhaust Emissions and Efficiencies

#### 4.3.1 Nitrogen Oxides and Soot

Indicated specific gaseous and smoke emissions were analyzed for the effect of dual fuel combustion compared to CDC and the effect of reduced cetane fuels compared to ULSD in RCCI. The emissions analysis focuses on the NO<sub>x</sub>-soot tradeoff, carbon monoxide, unburned hydrocarbons, and aldehydes. Trends in NO<sub>x</sub> emissions, as displayed in Figure 50, changed with the n-butanol content in the blends compared to neat ULSD. NO<sub>x</sub> levels decreased with increasing load in CDC and ULSD RCCI, however, NO<sub>x</sub> levels increased with load for the butanol blends in RCCI. Change in the NO<sub>x</sub> trend for the butanol blends is attributed to the increases in the premixed peak heat release rates, 30-40% larger than for ULSD RCCI. NO<sub>x</sub> levels reduced by 90% and 70% with ULSD RCCI compared to CDC at 4 and 6 bar IMEP respectively. S8-Bu RCCI had 62% higher NO<sub>x</sub> levels at 4 bar and 4% higher at 6 bar compared to ULSD-Bu RCCI. As load increased, the mass fraction of SOI-1 for both ULSD-Bu RCCI and S8-Bu RCCI start to converge, where the equivalence ratio at the time of ignition is higher for ULSD-Bu RCCI at 4 and 5 bar IMEP and lower at 6 bar. The lower equivalence ratios increase the rate of NO formation, increasing the total NO<sub>x</sub> formation for S8-Bu RCCI at these loads.

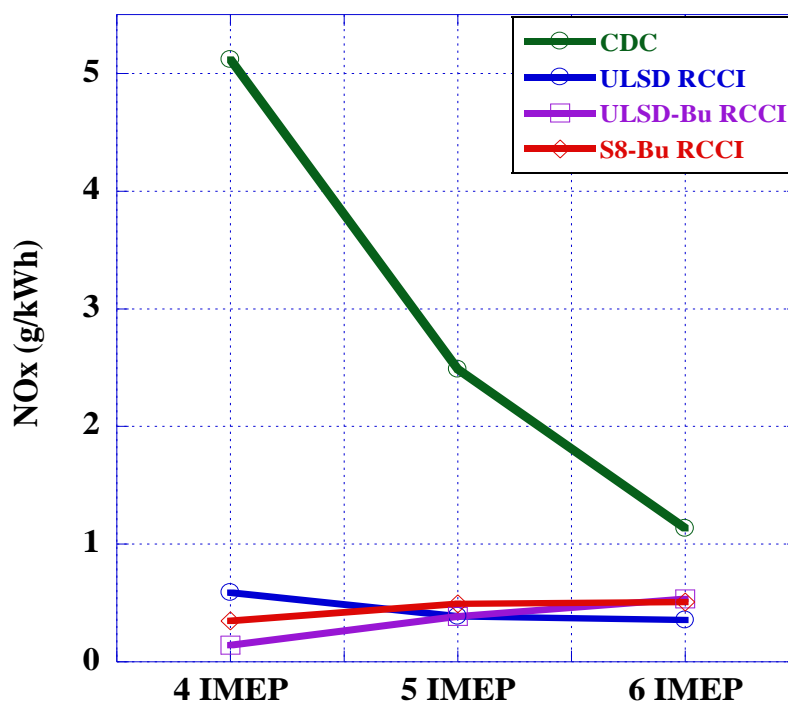
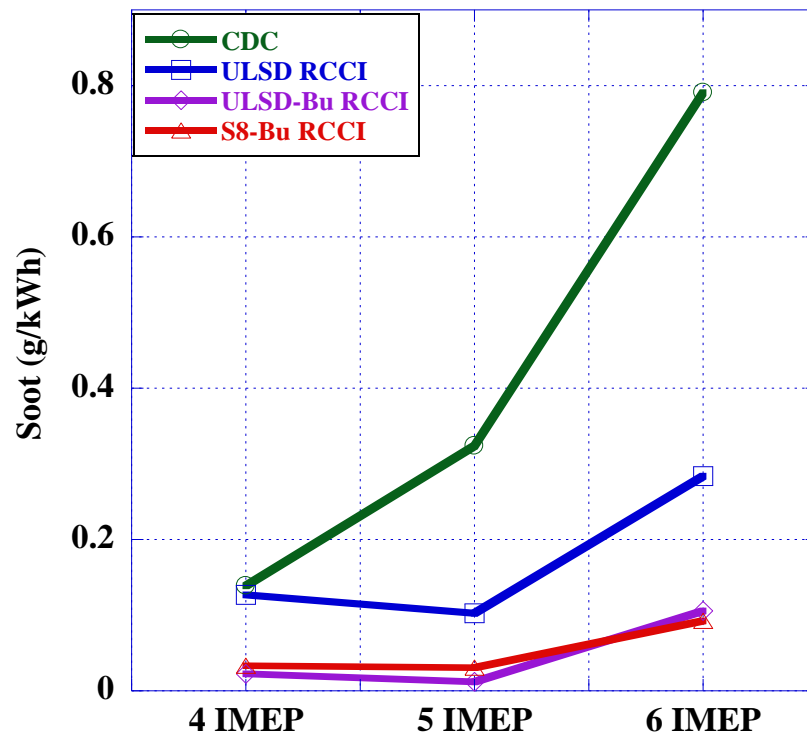


Figure 50 NO<sub>x</sub> Emissions across Engine Loads

Soot emissions are displayed in Figure 51, RCCI combustion reduced soot levels at the highest load by 65% for ULSD and 90% for both butanol blends compared to CDC. Early PFI and split DI events induce a homogeneous charge mixture in-cylinder, reducing areas of rich equivalence ratios with the increased mixing times. The reduction in soot for ULSD-Bu RCCI compared to ULSD RCCI is a result of the blended butanol and higher oxygen content for a more complete combustion. Lower cetane fuels are also beneficial by extending the ignition delay for a more homogeneous mixture prior to ignition. These reductions in soot for the butanol blends are also associated with butanol's high volatility, inducing higher mixing rates and increasing the carbon recession rate (Amann et al. 1980). Soot levels for S8-Bu RCCI are 40-60% higher than ULSD-Bu RCCI at the two lower loads. This corresponds to trends in the premixed phase of the AHRR, where soot levels are found to reduce with less rapid heat release rates (Li et al. 2015). Soot emissions increased with load for all combustion strategies as a result of constant engine rpms and increased fueling.



**Figure 51** Soot Emissions across Engine Loads

### 4.3.2 Carbon Monoxide, Unburned Hydrocarbons, & Formaldehydes

Figure 52 displays trends in carbon monoxide and unburned hydrocarbons. CO levels reduced with increasing load for RCCI. CO levels were highest for RCCI at 4 bar IMEP, due to the high relative air/fuel ratio (4.3) and low combustion temperatures. While in the LTC regime, this condition creates over-lean regions that are unable to oxidize CO (Wissink and Reitz 2015), where at the higher loads the higher fuel demand avoids over-leaning. The butanol blends reduced CO emissions by about 25% at each load compared to ULSD RCCI. The additional butanol in the DI fuel increases the volatility of the fuel, creating a more homogeneous mixture. CO levels for ULSD-Bu RCCI and S8-Bu RCCI nearly overlay each other, insinuating that the butanol is the influencing factor on CO reduction when compared to neat ULSD.

UHC emissions decreased as load increased for CDC and the three RCCI modes. CDC had 55-70% lower UHC emissions due to the lack of crevice effects and wall wetting with the early injections. ULSD-Bu RCCI increased UHC emissions 10-20% compared to RCCI with neat ULSD. This is attributed to higher mass fractions and longer durations of the first DI event for ULSD-Bu RCCI increasing wall wetting and crevice effects. UHC levels for S8-Bu RCCI were slightly lower than ULSD-Bu RCCI at the two lower loads, and higher at the highest load. At 4 and 5 bar IMEP, the injection duration for S8-Bu RCCI was shorter than that for ULSD-Bu RCCI. However, at the highest load, the injection duration for S8-Bu RCCI was longer. Injection duration had a direct relationship with UHC, corresponding to spray penetration and wall wetting.

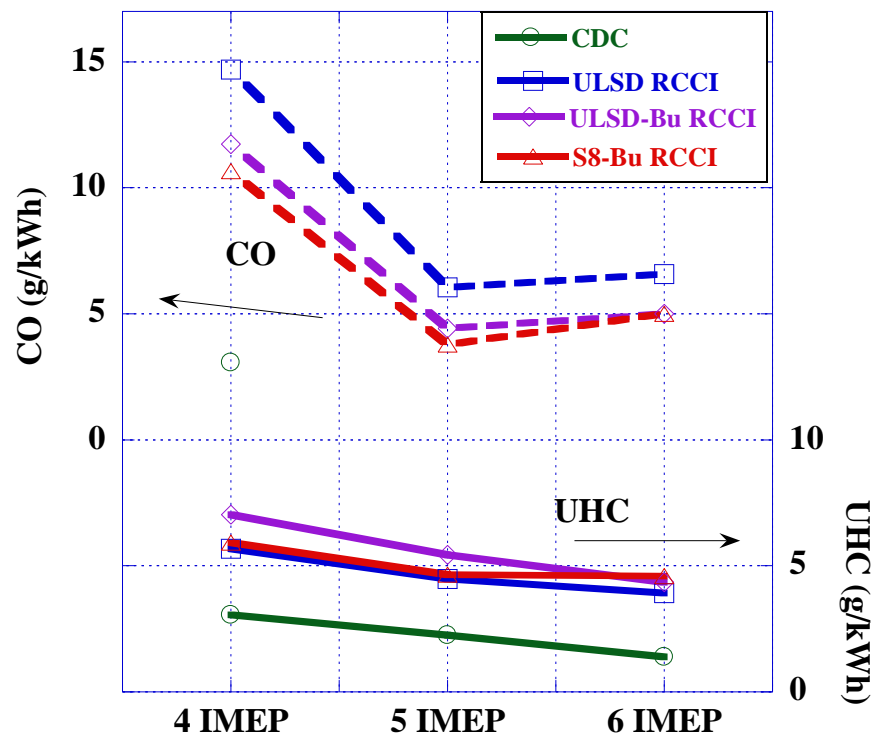


**Figure 52** CO and UHC Emissions across Engine Loads

Aldehyde emissions are displayed in Figure 53 below, including acetaldehydes and formaldehydes. Dual fuel combustion increases formaldehyde emissions, which is attributed to the addition of port fuel injection and also oxygenated butanol in the blended fuels. ULSD RCCI combustion increased formaldehyde emissions 75-80% compared to CDC, and an even larger increase is observed with the fuel blends, also found from Choi et al. (2015). S8-Bu RCCI had the highest levels of formaldehydes at 5 and 6 bar IMEP. This is a result of quenching effects and trapped mass in the piston fireland and crevice areas leading to unburned formaldehydes (CIMAC WG 17). From the heat flux and heat loss section, there is an increase in convection heat transfer for the S8-Bu blend compared to the ULSD-Bu blend at the highest load, which is recognized as an increase in the quenching effect and aldehyde emissions.

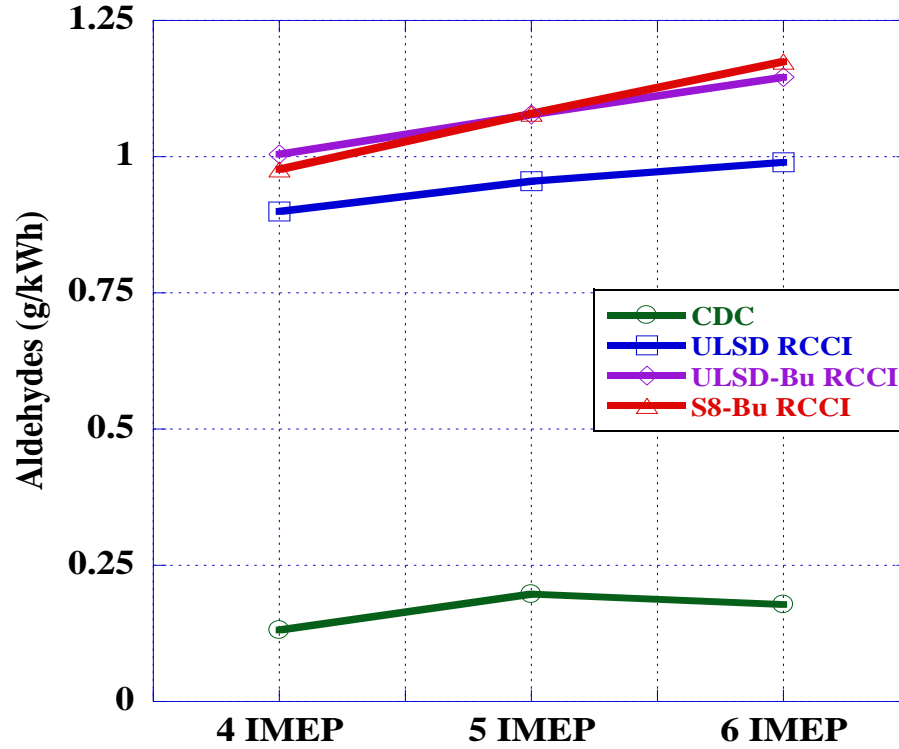


**Figure 53** Formaldehyde Emissions across Engine Loads

#### 4.3.3 Engine Efficiencies

Mechanical and net indicated thermal efficiencies (ITE) are displayed in Figure 54. Mechanical efficiency is defined as the ratio BMEP over IMEP and indicated thermal efficiency is the ratio of the indicated power over fuel energy. ULSD and ULSD-Bu RCCI have 3-4% higher mechanical efficiencies across the loads compared to CDC and S8-Bu RCCI. At constant IMEP, peak pressures for ULSD-Bu RCCI and S8-Bu RCCI were highest; however ULSD-Bu RCCI has a shorter combustion duration, increasing the useful energy due to reductions in heat transfer losses. The lower mechanical efficiency for S8-Bu RCCI compared to the two other RCCI modes is due to the earlier onset of combustion, decreasing the amount of the energy release during the expansion stroke. S8-Bu RCCI also had increased heat transfer losses as displayed previously. ULSD-Bu RCCI increased the mechanical efficiency compared to ULSD RCCI as a result of higher combustion pressures and heat release rates.

Indicated thermal efficiencies were above 50% for all fueling strategies. High ITE results are attributed to externally driving both the high pressure common rail pump and supercharger, reducing pumping losses. S8-Bu RCCI had the highest ITE at each load reaching 58% at 5 bar

IMEP. Increases in ITE for the S8-Bu blend compared to the ULSD-Bu blend is a result of longer combustion durations extending into the power stroke with similar heat transfer losses.

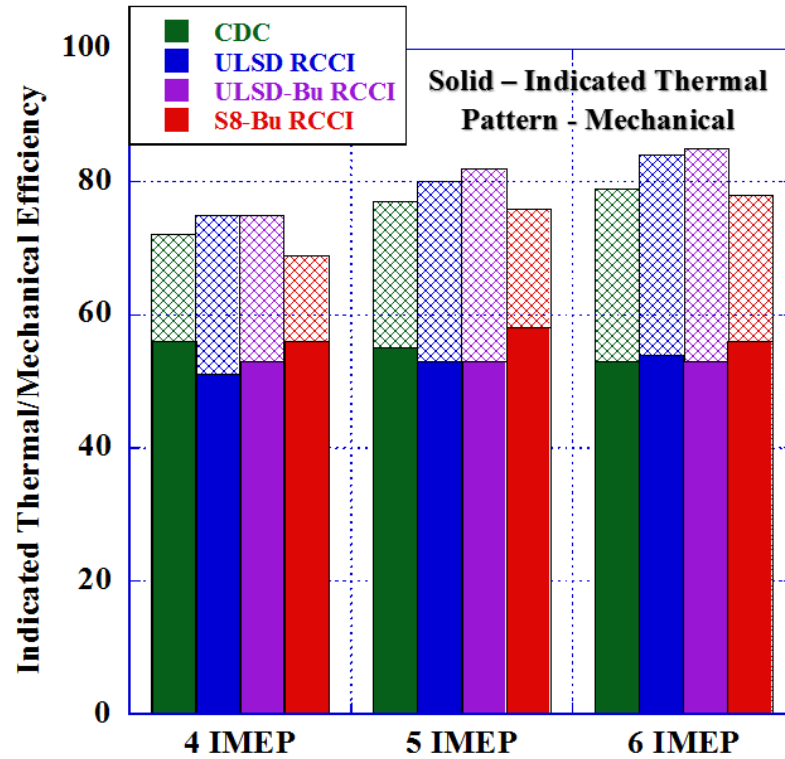


**Figure 54** Indicated Thermal and Mechanical Efficiency

The diesel equivalent brake specific fuel consumption is displayed in Figure 55 below. Derivation of the diesel equivalent BSFC was calculated by taking the proportional differences in both the energy and fuel densities compared to conventional ULSD. CDC maintained relatively constant BSFC across loads and decreased across loads in RCCI combustion. BSFC increased between 23% and 33% for the dual fuel modes compared to CDC due to the 60% mass fraction of butanol, which has a lower energy density than ULSD. ULSD-Bu RCCI and S8-Bu RCCI resulted in higher BSFC compared to ULSD RCCI where the energy densities are 10% lower for the butanol blended fuels, increasing the fuel demand to maintain engine load. Mechanical efficiencies were lowest for S8-Bu RCCI, requiring higher combustion pressures for the same IMEP, where the brake mean effective pressure is reduced.

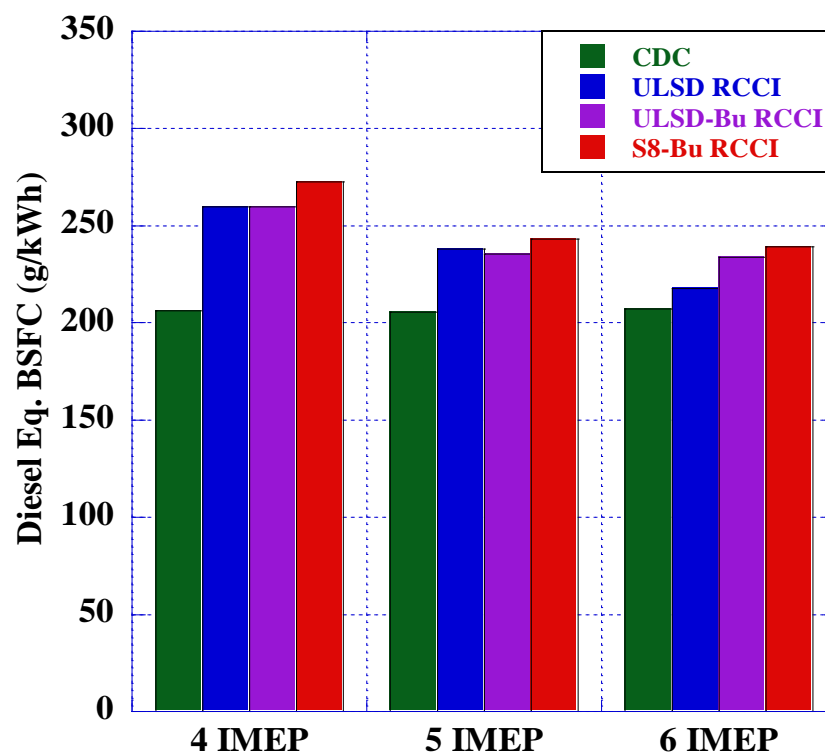


**Figure 55** Diesel Equivalent Brake Specific Fuel Consumption

## CHAPTER 5 CONCLUSION

### 5.1 Conclusion

Dual fuel combustion in RCCI mode was researched to study diesel combustion characteristics and exhaust emissions in low temperature combustion regimes. The experimental engine was initially optimized for low emissions in RCCI with conventional diesel as the high reactivity fuel. Diesel fuel was then replaced with two fuel blends of reduced ignition quality, including 1) ULSD and n-butanol, and 2) Fischer Tropsch S8 and n-butanol.

The hypothesis for this research states: *If fuel reactivity gradients with two fuels of low and high reactivity, are created in-cylinder in a Tier 0 diesel engine, then the engine out emissions can meet EPA Tier 4 levels for medium duty off-road diesel engines using reactivity controlled compression ignition modes.* RCCI combustion results validate the stated hypothesis with principle diesel emissions below regulated levels. NO<sub>x</sub> was under 1 g/kWh and NO<sub>x</sub> combined with non-methane hydrocarbons was a maximum of 7.6 g/kWh at 4 bar IMEP and PM under 0.4 g/kWh. Experimental engine testing was successful as all fueling strategies maintained stable engine conditions with a COV under 5% and reductions in exhaust emissions were found with dual fuel combustion.

Combustion pressure results display small increases in peak pressure for the RCCI modes compared to conventional diesel combustion, however sharp increases in pressure rise rates were induced due to the preconditioned air/butanol mixture. The butanol blends caused 30-40% increases in pressure rise rates compared to ULSD RCCI, surpassing the accepted limit of 15 bar/deg. Increases for the blends are due to the larger mass fraction of the first DI event, causing an HCCI like combustion with smaller reactivity gradients. All combustion modes displayed two stage apparent heat release rates. RCCI exhibited delayed combustion and over 30% higher peak heat release rates compared to CDC. Both ULSD-Bu RCCI and S8-Bu RCCI had similar peak values, where the variances are attributed to the equivalence ratio at the time of ignition. The RCCI strategies reduced the combustion duration compared to CDC by 50% at the highest load. ULSD RCCI and S8-Bu RCCI had nearly identical ignition delays and combustion durations across loads. ULSD-Bu RCCI extended the ignition delay by 2% and reduced combustion durations by 15% compared to the other fuels in RCCI. Low temperature combustion was achieved with peak temperatures below 1600°C for all fuels. Peak temperatures for the butanol blends were about



100°C higher than ULSD RCCI. At 6 bar IMEP, an inflection in the temperature trace is present at a crank angle a few degrees after the second DI event. This displays the high latent heat of vaporization of butanol in the fuel blend, creating a cooling effect. Ringing intensity for RCCI compared to CDC were similar at low load, but increased significantly as load increased. RI increased from under 1 MW/m<sup>2</sup> at 3 bar IMEP to 5 MW/m<sup>2</sup> at 6 bar IMEP for the butanol blends. The heat flux was increased in RCCI compared to CDC from the early injections and high heat release rates. Butanol blends increased the heat flux from the high vaporization rate of the fuel, causing higher droplet temperatures and vapor pressures. ULSD-Bu RCCI had the highest combustion efficiency at 97%, indicating that fuel stratification was more optimal at the operating parameters. Large reductions in harmful emissions were reached with simultaneous reductions of both NO<sub>x</sub> and soot up to 90%. NO<sub>x</sub> emissions were similar for the three RCCI modes; with levels less than 1 g/kWh at all loads. Differences in NO<sub>x</sub> emissions for RCCI are related to differences in heat release rates. Soot levels for the butanol blends resulted in reductions by up to 25% compared to conventional ULSD in RCCI. These reductions are attributed to the additional oxygen molecule in butanol, longer mixing times, and fuel stratification inducing reactivity gradients and a more complete combustion. Carbon monoxide emissions were nearly identical for the two fuel blends in RCCI and 25% lower compared to ULSD RCCI, insisting that the butanol is the driving factor. Unburned hydrocarbons increased from 55-70% compared to CDC due to crevice effects that correspond with early fuel injection methods. UHC levels were lowest with neat ULSD RCCI compared to the fuel blends. This was found to be directly related to the injection duration of the first injection event. Mechanical efficiencies for ULSD and ULSD-Bu RCCI had 3-4% higher mechanical efficiencies compared to CDC and S8-Bu RCCI. Increases are attributed to reductions in combustion durations and heat losses. Indicated thermal efficiencies were highest for S8-Bu RCCI due to the high ignition quality of S8. The diesel equivalent brake specific fuel consumption increased for RCCI modes compared to CDC. The largest contributor to this result is the large mass fraction of port fuel injected butanol, which has a lower energy density than diesel. The combustion and emissions characteristics for dual fuel combustion displayed promising results with potential to improve diesel exhaust emissions without the use of aftertreatment systems and reduce the demand for petroleum oil with the use of alternative fuels.

## **5.2 Future Work**

Continuous development of optimized combustion strategies are to be researched with alternative fuels. There are many variables involved in RCCI research including rail pressure, fuel injection pattern (number of pulses, pulse timing, and fuel ratio of each pulse), EGR rates, boost pressure, and air intake temperature. A newly developed boosting system will increase the allowable intake boost pressure and volumetric flow rate, which will induce higher CO oxidation for improved combustion efficiency in both conventional diesel combustion and dual fuel combustion. Optimizing these parameters with resulting heat release curves of Gaussian shape are desired in RCCI to control pressure rise rates and ringing intensities along with nearly zero smoke emissions.

## REFERENCES

- Alleman, Teresa, and Robert McCormick; (2003); “Fischer-Tropsch Diesel Fuels – Properties and Exhaust Emissions: A Literature Review.” SAE World Congress 2003; Detroit, MI; March 3-6, 2003; Accessed June 8, 2016.
- Alternative Fuels Data Center – Fuel Properties Comparison [dataset]. October 29, 2014; 2014, Oct 29 [cited 2017 Nov 5]. Available from: [www.afdc.energy.gov](http://www.afdc.energy.gov).
- Amann, C, Stivender, D, Plee, S, and J. MacDonald; (1980); “Some Rudiments of Diesel Particulate Emissions.” SAE Technical paper 800251, 1980; <https://doi.org/10.4271/800251>.
- Andrew Norman; (2016). *Diesel Technology Fundamentals, Service, Repair Eight Edition*. Tinley Park, IL: Goodheart-Willcox Co., Inc.
- ASTM D7668-14a; (2014); *Standard Test Method for Determination of Derived Cetane Number (DCN) of Diesel Fuel Oils—Ignition Delay and Combustion Delay Using a Constant Volume Combustion Chamber Method*; ed. West Conshohocken, PA: ASTM International, 2014.
- Babu, Vinod, Murthy, Madhu, and Amba Prasad Rao; (2017); “Butanol and Pentanol: The Promising Biofuels for CI Engines – A Review.” *Renewable and Sustainable Energy Reviews* 78(2017):1068-1088. Accessed February 28, 2018.
- Bae, Choongsik, and Jaeheun Kim; (2016); “Alternative Fuels for Internal Combustion Engines.” *Proceedings of the Combustion Institute* 36 (2017):3389-3413; Accessed February 27, 2018.
- Benajes, Jesus, Martin, Jaime, Garcia, Antonio, et al; (2015); “In-Cylinder Soot Radiation Heat Transfer in Direct Injection Diesel Engines.” *Energy Conversion and Management* 106 (2015): 414-427.
- Blocking, Wolfgang, and Klaus Wenzlawski; (2016); *Internal Combustion Engine Handbook*; Edited by Richard van Basshuysen and Fred Schäfer; Translated by TechTrans; 2<sup>nd</sup> Edition; Warrendale, PA; SAE International.

- Borman, Gary, and Kazuie Nishiwaki; (1987); "Internal-Combustion Heat Transfer." *Progress in Energy and Combustion Science* 1 (1987): 1-46.
- Bression, Guillaume, Soleri, Dominique, Savy, Sylvain et al; (2008); "A Study of Methods to Lower HC and CO Emissions in Diesel HCCI." *SAE Int. J. Fuels Lubr.* 1 (2008): 37-49; Accessed January 30, 2018.
- Buratti, Riccardo, Imarisio, Roberto, and Bruce Peters; (2004); "Experiences with Common Rail, a Technology Changing the Image of Diesels in Europe." *SAE Technical Paper 2004-28-0072*, 2004; doi:10.4271/2004-28-0072.
- C. Lyle, Jr. Cummins; (1976a); *Internal Fire*; Carnot Press, Lake Oswego, Oregon 1976.
- C. Lyle, Jr. Cummins; (1976b); "Early IC and Automotive Engines." *SAE Technical Paper 760604*; 1976.
- Center for Disease Control and Prevention; (2017); "Carbon Monoxide Poisoning." U.S. Department of Health & Human Services; Last modified October 26, 2016; Accessed January 28, 2018; 2018; <https://ephtracking.cdc.gov/showCoRisk.action>.
- Chadwell, Christopher, Alger, Terrence, and Charles Roberts; (2011); "Boosting Simulation of High Efficiency Alternative Combustion Mode Engines," *SAE Int. J. Engines* 4 (2011): 375-393.
- Chen, Zheng, Liu, Jingping, Wu, Zhenkuo, and Chiafon Lee; (2013); "Effects of Port Fuel Injection (PFI) of n-Butanol and EGR on Combustion and Emissions of a Direct Injection Diesel Engine." *Energy Conversion and Management* 76 (2013): 725-731.
- Chevron Products Company; (2007); "Diesel Fuels Technical Review." Chevron Corporation.
- Choi, Byungchul, Jiang, Xiaolong, Kwon Kim, Young, et al; (2015); "Effect of Diesel Fuel Blend with n-Butanol on the Emission of a Turbocharged Common Rail Direct Injection Diesel Engine." *Applied Energy* 146 (2015): 20-28.
- CIMAC WG 17, Gas Engines. Methane and Formaldehyde Emissions of Gas Engines. CIMAC Position Paper WG 17, 2014-04.

Clifford A. Moses; (2008); “Comparative Evaluation of Semi-Synthetic Jet Fuels.” CRC Project No. AV-2-04a.

Control Soft Inc; (2016); “PID Loop Tuning Pocket Guide Version 2.0.” Accessed July 20, 2015. <https://www.controlglobal.com>.

David Roylance; (2000); *Shear and Torsion*; Massachusetts Institute of Technology; Cambridge, MA; Accessed February 23, 2018.

Dempsey, Adam, Curran, Scott, and Rolf Reitz; (2015); “Characterization of Reactivity Controlled compression Ignition (RCCI) Using Premixed Gasoline and Direct-Injected Gasoline with a Cetane Improver on a Multi-Cylinder Engine.” SAE Int. J. Engines 8:2 (2015): 859-877; Accessed February 26, 2018.

Derek Splitter; (2012); “High Efficiency RCCI Combustion.” PhD Thesis; University of Wisconsin; Accessed August 15, 2017; ResearchGate.

DieselNet; (1997); “Emissions Standards.” Accessed January 25, 2018. <https://www.dieselnets.com/standards/>.

Dieter Leckel; (2009); “Diesel Production from Fischer-Tropsch: The Past, the Present, and New Concepts.” Energy & Fuels 2009, 23, 2342-2358; Accessed March 2, 2018.

Ekholm, Kent, Karlsson, Maria, Tunestål et al; (2008); “Ethanol-Diesel Fumigation in a Multi-Cylinder Engine.” SAE Int. J. Fuels Lubr. 1 (2008): 26-36; Accessed January 30, 2018.

Environmental Protection Agency; (1999); “Technical Bulletin: Nitrogen Oxides (NO<sub>x</sub>), Why and How They are Controlled,” Office of Air Quality Planning and Standards EPA 456/F-99-006R.

Environmental Protection Agency; (2003); “Particle Pollution and Your Health” Office of Air Quality Planning and Standards EPA-452/F-03-001.

Environmental Protection Agency; (2016); *Nonroad Compression-Ignition Engines: Exhaust Emissions Standards*; Office of Transportation and Air Quality; EPA-420-B-16-022; March 2016.

- Gaubert, Remi, Soloiu, Valentin, Muinos, Martin, et al; (2017); "Development and Implementation of a Common Rail Fuel Injection System for Flexible Combustion for an Experimental Medium Duty Diesel Engine." SAE Technical Paper 2017-01-0790.
- Gaubert, Remi, Soloiu, Valentin, Moncada, Jose, et al; (2018); "Reactivity Controlled Compression Ignition and Low Temperature Combustion of Fischer-Tropsch Fuel Blended with n-Butanol." Renewable Energy Ref. No.: RENE-D-18-00738; Submitted for Review.
- Gross, Christopher, and Rolf Reitz; (2017); "Investigation of Steady-State RCCI Operation in a Light-Duty Multi-Cylinder Engine Using "Dieseline." SAE Technical Paper 2017-01-0761, 2017, doi:10.4271/2017-01-0761. Accessed September 15, 2017.
- H. Burtscher; (2005); "Physical characterization of particulate emissions from diesel engines: a review." *Aerosol Science* 36 (2015): 896–932; Accessed January 28, 2018; doi:10.1016/j.jaerosci.2004.12.001.
- Han, Xiaoye, Zheng, Ming, Tjong, Jimi, and Tie Li; (2015); "Suitability Study of n-Butanol for Enabling PCCI and HCCI and RCCI Combustion on a High Compression-ratio Diesel Engine." SAE Technical Paper 2015-01-1816, 2015, <https://doi.org/10.4271/2015-01-1816>.
- Hedge, Swati, Lodge, Jeffery, and Thomas Trabold; (2018); "Characteristics of Food Processing Wastes and their Use in Sustainable Alcohol Production." *Renewable and Sustainable Energy Reviews* 81 (2018):510-523. Accessed February 28, 2018.
- Han, Xiaoye, Zheng, Ming, Tjong, Jimi, and Tie Li; (2015); "Suitability Study of n-Butanol for Enabling PCCI and HCCI and RCCI Combustion on a High Compression-ratio Diesel Engine." SAE Technical Paper 2015-01-1816, 2015; Accessed January 28, 2018; <https://doi.org/10.4271/2015-01-1816>.
- Inagaki, Kazuhisa, Fuyuto, Takayuki, Nishikawa, Kazuaki, Nakakita, Kiyomi, and Ichiro Sakata; (2006); "Dual-fuel PCI combustion controlled by in-cylinder stratification of ignitability." SAE Technical Paper 2006-01-0028, 2006; <https://doi.org/10.4271/2006-01-0028>.

- International Energy Agency – Advanced Motor Fuels; “Fuel Information: Bio/Synthetic Diesel (Paraffins).” Accessed March 4, 2018. [http://www.iea-amf.org/content/fuel\\_information/paraffins](http://www.iea-amf.org/content/fuel_information/paraffins).
- J.A. Eng; (2002); “Characterization of Pressure Waves in HCCI Combustion.” SAE Technical Paper 2002-01-2859, 2002; <https://doi.org/10.4271/2002-01-2859>.
- Jääskeläinen, Hannu, and Magdi K. Khair; (2015); “Diesel Fuel Injection – Common Rail Fuel Injection.” DieselNet; Last modified May, 2015; Accessed January 26, 2018; [https://www.dieselnets.com/tech/diesel\\_fi\\_common-rail.php](https://www.dieselnets.com/tech/diesel_fi_common-rail.php).
- J.B. Heywood; (1988); *Internal Combustion Engine Fundamentals*. New York, NY: McGrawHill, Inc.
- J.B. Heywood; (1981); Automotive Engines and Fuels: A Review of Future Options.” *Progress in Energy and Combustion Science* 7 (1981):155–184.
- Jia, Ming, Li, Yaopeng, Xie, Maozhao, et al; (2015); “The effect of injection timing and intake valve close timing on performance and emissions of diesel PCCI engine with a full engine cycle CFD simulation.” *Energy Procedia* 66 (2015): 33-36; Accessed January 31, 2018; doi: 10.1016/j.egypro.2015.02.018.
- Jin, Chao, Yao, Mingfa, Liu, Haifeng, Lee, et al; (2011); “Progress in the Production and Application of n-Butanol as a Biofuel.” *Renewable and Sustainable Energy Reviews* 15(2011):4080-4106. Accessed February 26, 2018.
- Kokjohn, Sage, Hanson, Reed, Splitter, Derek, and Rolf Reitz; (2009); “Experiments and Modeling of Dual-Fuel HCCI and PCCI Combustion Using In-Cylinder Fuel Blending.” *SAE Int. J. Engines* 2 (2009): 24-39; Accessed January 30, 2018.
- Kokjohn, Sage, Hanson, Reed, Splitter, Derek, et al; (2011); “Fuel Reactivity Controlled Compression Ignition (RCCI) Combustion in Light- and Heavy-Duty Engines.” *SAE Int. J. Engines* 4 (2011): 360-74; Accessed January 30, 2018.
- Lapuerta, Magin, Garcia-Contreras, Reyes, Campos-Fernandez, Javier, and M. Pilar Dorado; (2010); “Stability, Lubricity, Viscosity, and Cold-Flow Properties of Alcohol – Diesel Blends.” *Energy & Fuels* (24) (2010): 4497-4502; Accessed March 6, 2018.

- Levin Institute – State University of New York; (2016); “Globalization 101: Fossil Fuels.” Accessed January 25, 2018; <http://www.globalization101.org/fossil-fuels/>.
- Li, J., Yang, W.M., An, A., et al; (2015); “Numerical Investigation on the Effect of Reactivity Gradient in an RCCI Engine Fueled with Gasoline and Diesel.” *Energy Conversion and Management* 92 (2015): 342-352. Accessed February 27, 2018.
- Li, Yaopeng, Jia, Ming, Chang, Yachao, et al; (2018); “Principle of Determining the Optimal Operating Parameters Based on Fuel Properties and Initial Conditions for RCCI Engines;” *Fuel* 216 (2018) 284-295. Accessed February 27, 2018.
- Majewski, W. Addy, and Magdi Khair; (2006); *Diesel emissions and their control*. Warrendale, PA: SAE International; ISBN: 978-0-7680-0674-2.
- Mikulski, Maciej, and Cemil Bekdemir; (2017); “Understanding the Role of Low Reactivity Fuel Stratification in a Dual Fuel RCCI Engine – A Simulation Study.” *Applied Energy* 191 (2017): 689-708.
- Mohebbi, Mostafa, Reyhanian, Masoud, Hosseini, Vahid, et al; (2018); “Performance and Emissions of a Reactivity Controlled Light-Duty Diesel Engine Fueled with n-Butanol-Diesel and Gasoline.” *Applied Thermal Engineering* 134 (2018) 214-228.
- National Instruments Corp; (2014); *National Instruments Direct Injection Driver System Manual*. Instruction Manual; National Instruments 2013.
- Nazemi, M., and M. Shahbakhti; (2016); “Modeling and Analysis of Fuel Injection Parameters for Combustion and Performance of an RCCI Engine.” *Applied Energy* 165 (2016): 135-150. Accessed February 27, 2018.
- Neely, Gary, Sasaki, Shizuo, Huang, Yiqun, et al; (2005); “New Diesel Emission Control Strategy to Meet US Tier 2 Emissions Regulations.” *SAE World Congress 2005*; Detroit, MI; April 11-14, 2005; Accessed February 20, 2018.
- Nieman, Derek, Dempsey, Adam, and Rolf Reitz; (2012); “Heavy-Duty RCCI Operation Using Natural Gas and Diesel.” *SAE Int. J. Engines* 5(2):270-285; Accessed October 10, 2016; doi:10.4271/2012-01-0379.



- Oki, Mamoru, Matsumoto, Shuichi, Toyoshima, Yoshio, et al; (2006); “180MPa Piezo Common Rail System.” SAE World Congress 2006; Detroit, MI; April 3-6, 2006; Accessed March 26, 2015.
- Okude, Keiichi, Mori, Kazutoshi, Shiino, Shiroh, and Takeshi Moriya; (2004); “Premixed compression ignition (PCI) combustion for simultaneous reduction of NO<sub>x</sub> and soot in diesel engine.’ SAE Fuels & Lubr 2004; Toulouse, France; June 8-10, 2004; Accessed January 31, 2018.
- Resitoğlu, Ibrahim, and Kemal Altinisik; (2015); “The Pollutant Emissions from Diesel-Engine Vehicles and Exhaust Aftertreatment Systems.” *Clean Technology Environmental Policy* 17 (2015): 15-27; Accessed January 28, 2018; DOI 10.1007/s10098-014-0793-9.
- Ronald L. Graves; (1999); “Review of Diesel Exhaust Aftertreatment Programs.” SAE Government/Industry Meeting 1999; Washington, D.C.; April 26-28, 1999; Accessed March 5, 2018.
- Scherm, Peter, Beutel, Tilman, Mayer, Andreas, Kasper, Markus, and Heinz Burtscher; (2016); *Internal Combustion Engine Handbook*; Edited by Richard van Basshuysen and Fred Schäfer; Translated by TechTrans; 2<sup>nd</sup> Edition; Warrendale, PA; SAE International.
- Shimadzu Corporation; (2012); *Thermal Analysis Instruments: 60 Series*; Japan; 2012.
- Sjöberg, Magnus, and John E. Dec; (2008); “Influence of Fuel Autoignition Reactivity on the High-Load Limits of HCCI Engines.” *SAE Int. J. Engines* 1 (2008): 39-58; Accessed January 30, 2018.
- Soloiu, Valentin, Duggan, Marvin, Harp, Spencer, et al; (2013); “PFI (Port Fuel Injection) of n-Butanol and Direct Injection of Biodiesel to Attain LTC (Low Temperature Combustion) for Low-Emissions Idling in a Compression Ignition Engine.” *Energy* 52 (2013): 143-154.
- Soloiu, Valentin, Muinos, Martin, and Spencer Harp; (2015); “Investigation of Dual Fuel PCCI (PFI of n-Butanol and DI-ULSD) Compared with DI of Binary Mixtures of the Same Fuels in an Omnivorous Diesel Engine.” SAE Technical paper 2015-01-0857, 2015; <https://doi.org/10.4271/2015-01-0857>.

- Soloiu, Valentin, Gaubert, Remi, Moncada, Jose, et al; (2017); "Partially Premixed Compression Ignition of Fischer Tropsch Synthetic Paraffinic Kerosene (S8) with PFI of n-Butnaol." ASME ICEF 3674, 2017.
- Splitter, Derek, Kokjohn, Sage, Rein, Keith, Hanson, Reed et al; (2010); "An Optical Investigation of Ignition Processes in Fuel Reactivity Controlled PCCI Combustion," SAE Int. J. Engines 3(1):142-162, 2010, doi:10.4271/2010-01-0345.
- Splitter, Derek, Hanson, Reed, Kokjohn, Sage, and Rolf Reitz; (2011); "Reactivity Controlled Compression Ignition (RCCI) Heavy-Duty Engine Operation at Mid-and High-Loads with Conventional and Alternative Fuels." SAE Technical Paper 2011-01-0363, 2011; doi:10.4271/2011-01-0363.
- Syed Yousufuddin; (2016); "Effect of Combustion duration on the Operating and Performance Characteristics of a Hydrogen-Ethanol Dual Fueled Engine: An Experimental Analysis." Int. J. Advances in Automotive and Technology 1 (1): 36-45.
- Tang, Qinglong, Liu, Haifeng, Li, Mingkun, et al; (2017); "Multiple Optical Diagnostics on Effect of Fuel Stratification Degree on Reactivity Controlled Compression Ignition." Fuel 202 (2017): 688-698.
- Tonetti, Marco, Rustici, Giorgio, Buscema, Massimo, and Luca Ferraris; (2017); "Diesel Engine Technologies Evolution for Future Challenges." SAE Technical Paper 2017-24-0179, 2017; doi:10.4271/2017-24-0179.
- Torregrosa, A.J, Broatch, A., García, A., and L.F. Mónico; (2013); "Sensitivity of Combustion Noise and NO<sub>x</sub> and Soot Emissions to Pilot Injection in PCCI Diesel Engines." Applied Energy 104 (2013): 149-157; Accessed January 31, 2018; <http://dx.doi.org/10.1016/j.apenergy.2012.11.040>.
- U.S. Department of Energy; "Fossil." Accessed January 25, 2018, <https://energy.gov/science-innovation/energy-sources/fossil>.
- U.S. Department of Energy; "Alternative Fuel Definition." Accessed February 27, 2018. <https://www.afdc.energy.gov/laws/391>.

- Walker, Ryan, Dempsey, Adam, Andrie, Michael, and Rolf Reitz; (2013); “Use of Low-Pressure Direct-Injection for Reactivity Controlled Compression Ignition (RCCI) Light-Duty Engine Operation.” SAE Technical Paper (2013); Accessed January 10, 2018.
- Wissink, Martin, and Rolf Reitz; (2015); “Direct Dual Fuel Stratification, a Path to Combine the Benefits of RCCI and PPC.” SAE Int. J. Engines 8 (2) (2015): 878-889.
- Worthington Biochemical Corporation; (1972); *Manual of Clinical Enzyme Measurements*; Worthington Diagnostics; 1972.
- Xiao, Junhua, Jia, Ming, Chang, Yachao, et al; (2018); “Numerical Optimization and Comparative Study of n-Butanol/Diesel Reactivity Stratification Combustion for Advanced Compression Ignition (CI) Engine.” Fuel 213 (2018):83-97. Accessed March 6, 2018.
- Yang, Yi, Dec, John, Dronniou, Nicolas, et al; (2011); “Partial Fuel Stratification to Control HCCI Heat Release Rates: Fuel Composition and Other Factors Affecting Pre-Ignition Reactions of Two-Stage Ignition Fuels.” SAE Int. J. Engines 4 (2011): 1903-20; Accessed January 31, 2018.

### Appendix A – 3D Model of the Experimental Engine with Common Rail fuel Injection System

Figures A1 and A2 are 3D models of the experimental engine setup. Figure A1 is a top view with the primary mechanical components of the common rail system listed, and Figure A2 is a side view of the entire engine with the exhaust system.

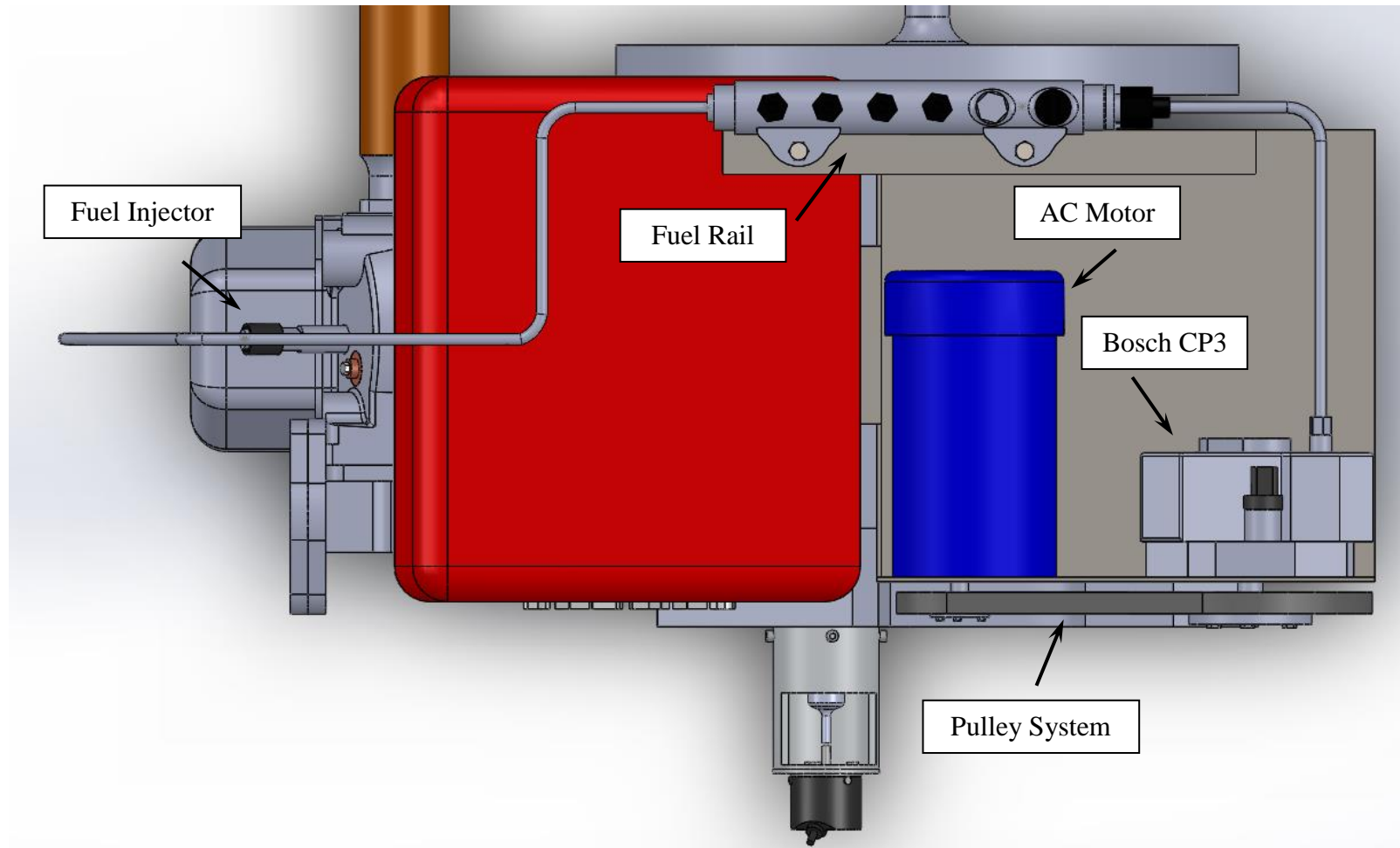


**Figure A1** Top View of the Engine Configured with the Common Rail Fuel Injection System

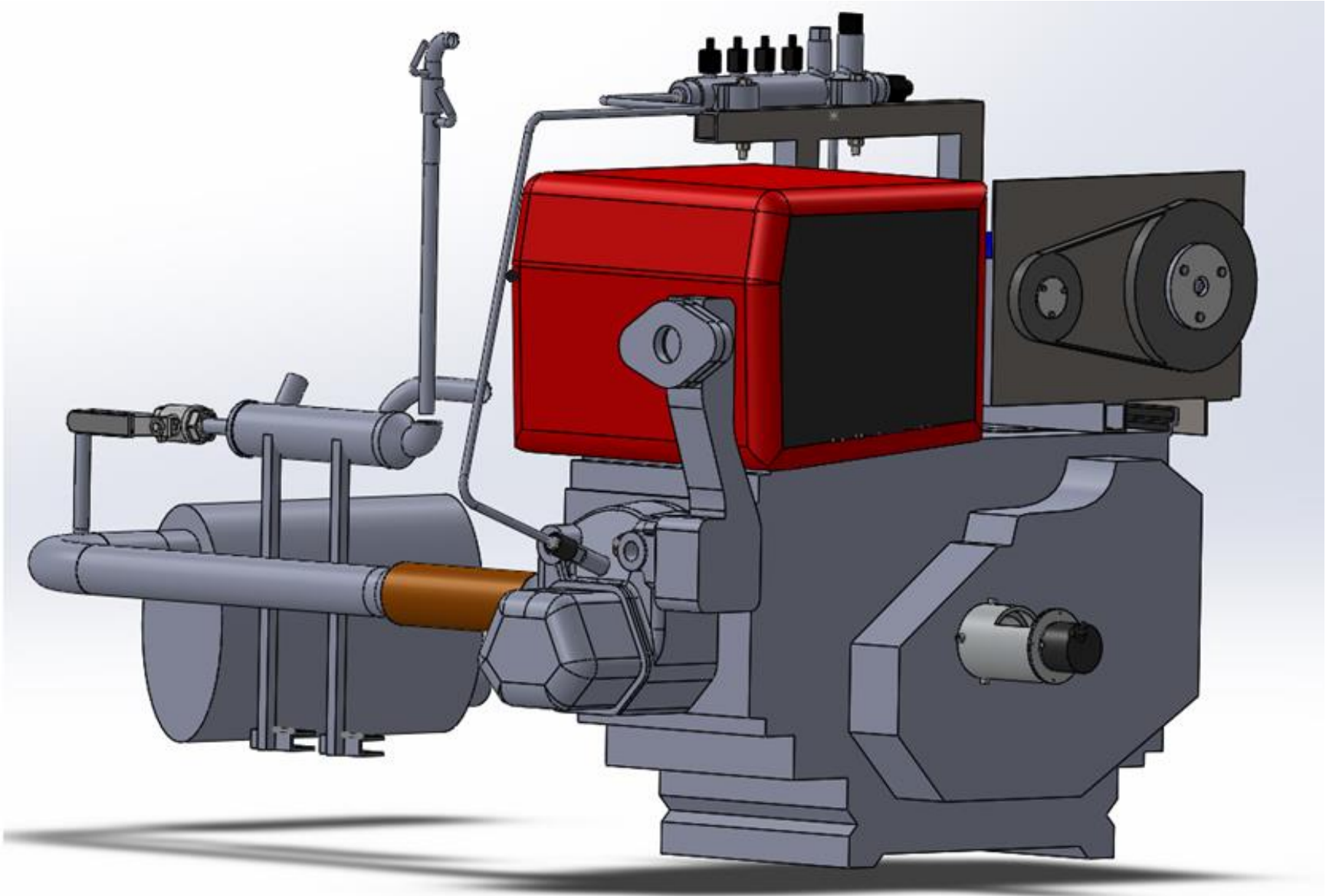


**Figure A2** 3D Model of the Experimental Engine

## Appendix B – Common Rail Fuel Injection Control Interface

Figures B1 through B4 are the primary control screens involved in the National Instruments Direct Injection Driver interface. Figure B1 is the DI Driver Setup window, which includes specifications of the piezoelectric injector parameters along with diagnostic error displays on the right hand side of the image. An example of the on board injector scope is provided in Figure B2. Figure B3 is used for setting up the Port Fuel Injection Module, which also includes additional diagnostic error displays. The rail pressure control interface is provided in Figure B4. With this screen, selection of using an electronic inlet metering valve or high pressure valve is input, along with the PID control parameters.

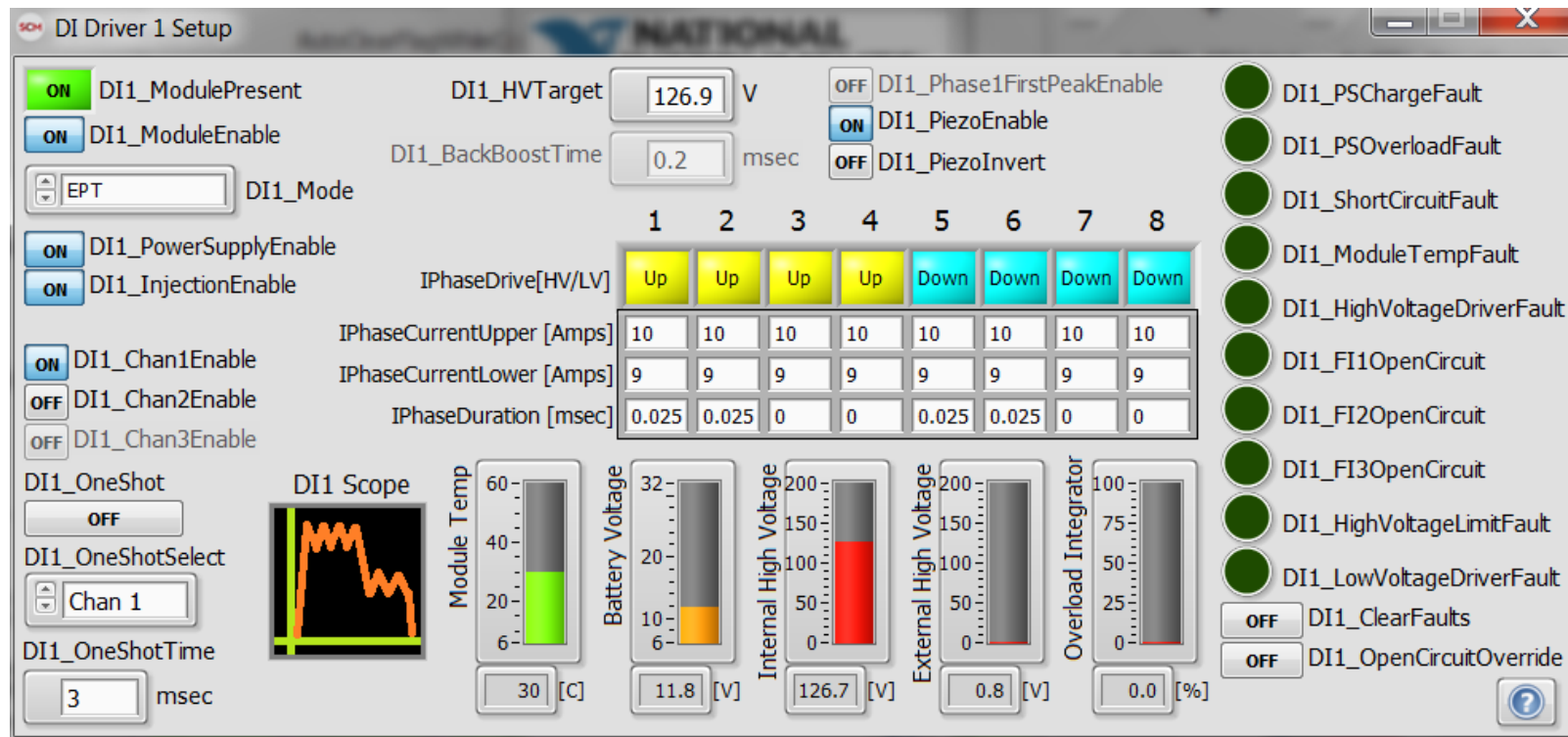
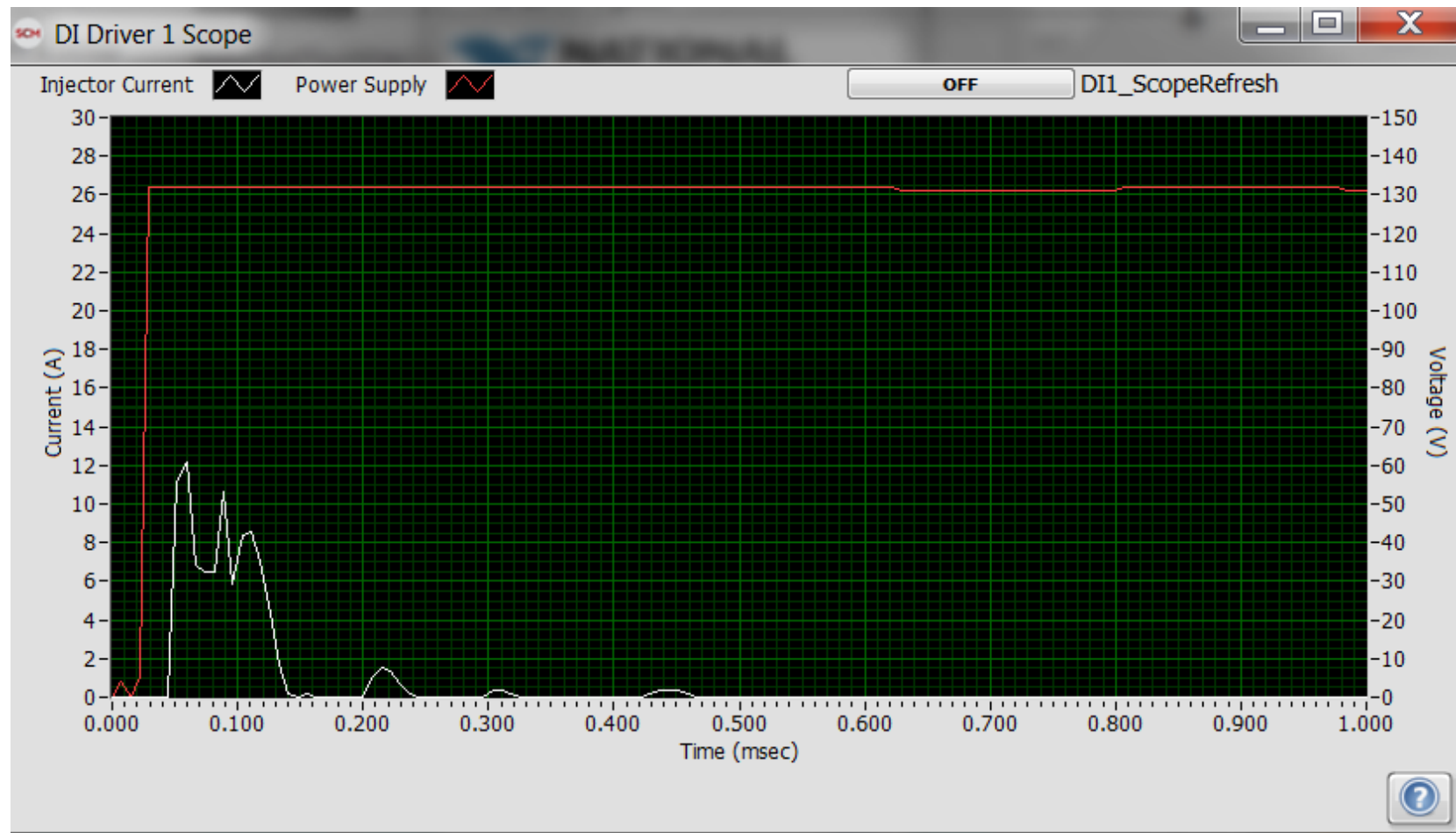
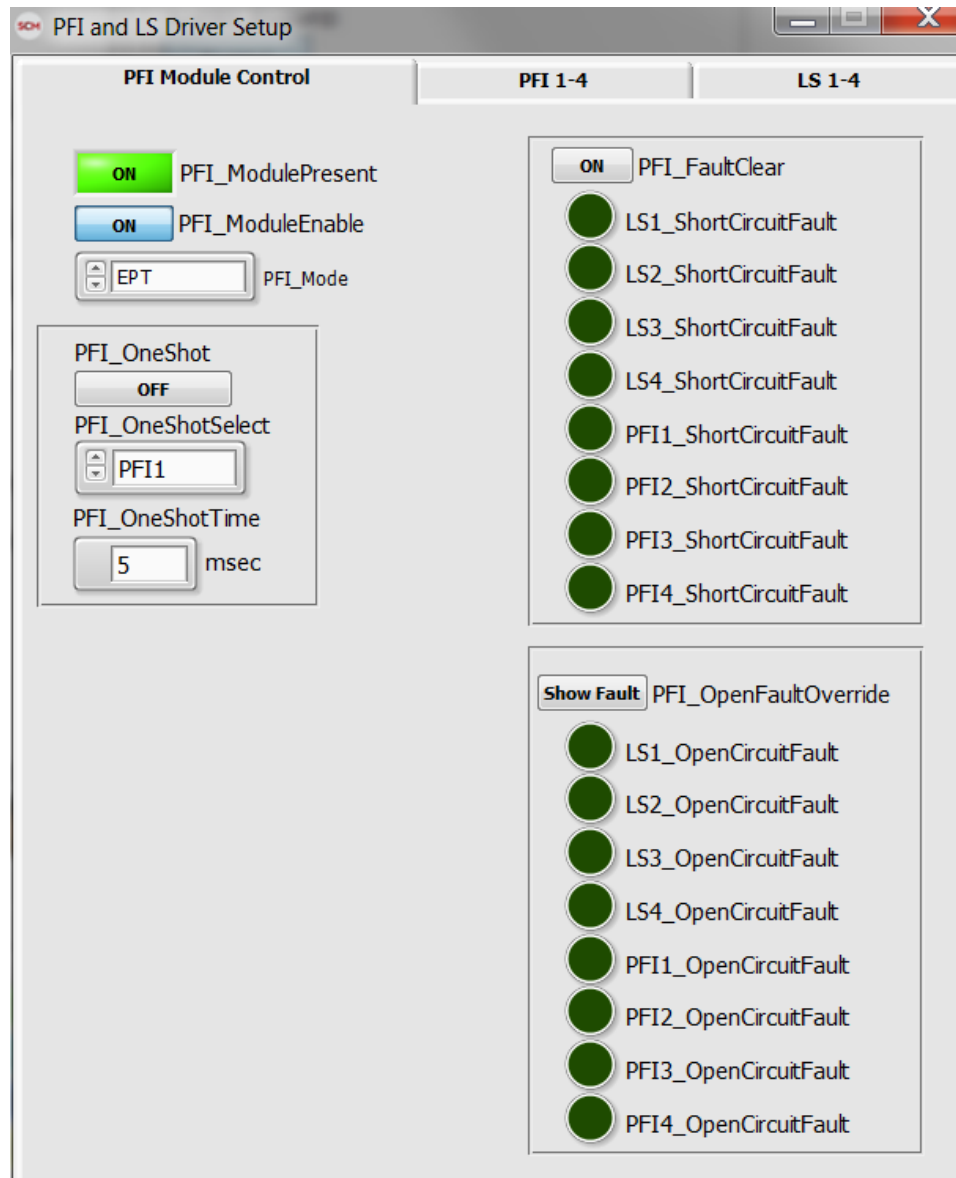


Figure B1 DI Driver Setup Window



**Figure B2** Example of a Piezoelectric Actuation Signal from the DID Scope



**Figure B3** Port Fuel Injector and Low Side Driver Window



**Rail Pressure Control Setup**

|                                |                         |                                   |                                |                     |
|--------------------------------|-------------------------|-----------------------------------|--------------------------------|---------------------|
| PFI_ModulePresent<br><b>ON</b> | RailP_Channel<br>AI0    | RailP_Max_Thresh<br>1800 [bar]    | RailP_Fault<br><b>No Fault</b> | BattV<br>11.769 [V] |
| RailP_Setpoint<br>1000 [bar]   | RailP<br>1019.971 [bar] | RailP_ControlMode<br>IMV PID MODE | <b>Clear RailP Fault</b>       | RPC Plot<br>        |

|                              |                           |                      |                          |                   |                       |
|------------------------------|---------------------------|----------------------|--------------------------|-------------------|-----------------------|
| IMV_Enable<br><b>ENABLED</b> | IMV_LSChanAsn<br>LS1, LS2 | IMV_Freq<br>175 [Hz] | HPV_Enable<br><b>OFF</b> | HPV_LSChanAsn<br> | HPV_Freq<br>1000 [Hz] |
|------------------------------|---------------------------|----------------------|--------------------------|-------------------|-----------------------|

|                         |               |                     |                         |               |                      |
|-------------------------|---------------|---------------------|-------------------------|---------------|----------------------|
| IMV_Kc<br>-0.03 [%/bar] | IMV_Kp_Action | IMV_PIDMax<br>3 [%] | HPV_Kc<br>0.001 [%/bar] | HPV_Kp_Action | HPV_PIDMax<br>20 [%] |
| IMV_Ti<br>1.45 [min]    | IMV_Ti_Action | IMV_PIDMin          | HPV_Ti<br>0 [min]       | HPV_Ti_Action | HPV_PIDMin           |
| IMV_Td<br>0 [min]       | IMV_Td_Action | -4 [%]              | HPV_Td<br>0 [min]       | HPV_Td_Action | -20 [%]              |

|                          |                          |                                  |                          |                       |                                  |
|--------------------------|--------------------------|----------------------------------|--------------------------|-----------------------|----------------------------------|
| IMV_PIDFF<br>42 [%]      | IMV_PID<br>0.623199 [%]  | IMV_ManualOverride<br><b>OFF</b> | HPV_PIDFF<br>20 [%]      | HPV_PID<br>0 [%]      | HPV_ManualOverride<br><b>OFF</b> |
| IMV_NonPIDFF +<br>20 [%] | IMV_ManualDC<br>36.5 [%] |                                  | HPV_NonPIDFF +<br>40 [%] | HPV_ManualDC<br>0 [%] |                                  |

|                            |                              |                        |                            |
|----------------------------|------------------------------|------------------------|----------------------------|
| IMV_MaxDCCalc<br>79.02 [%] | IMV_DC<br>42.623 [%]         | HPV_MaxDCCalc<br>0 [%] | HPV_DC<br>0 [%]            |
| IMV_MaxDC<br>80 [%]        | IMV_NomResistance<br>3.1 [Ω] | HPV_MaxDC<br>0 [%]     | HPV_NomResistance<br>3 [Ω] |
| IMV_MinDC<br>0 [%]         | IMV_Current<br>1.618 [A]     | HPV_MinDC<br>0 [%]     | HPV_Current<br>0 [A]       |

**Figure B4** Rail Pressure Control Setup Window

### **Appendix C – User Interface of the Data Acquisition and Real-Time Monitoring Systems**

The following images are examples of the real time data acquisition systems including the AVL Indicom v2.5 and NI 6251 interfaces. Figure C1 is an in-cylinder combustion cycle pressure trace with calculated values for engine rpm, pressure rise rates, indicated mean effective pressure, and the coefficient of variation. Figure C2 includes examples of the heat flux in the top two graphs and the apparent heat release rate in the bottom left graph. Figure C3 displays the pressure trace and resulting mass burned curve. The boxes in the top left of the image include values for CA10, 50, and 90 (AI10, 50, 90). These are used to control combustion phasing at the various operating conditions. Figures C4 through C6 display the NI data acquisition user interface and block diagram. The front panel includes the various input parameters for calculations, along with air flow rate inputs from the Meriam Laminar flow meter to be averaged throughout the testing interval. The last two images are portions of the block diagrams including the collection of the various data arrays for averaging of each individual signal and the conversion from a voltage signal to a physical parameter.

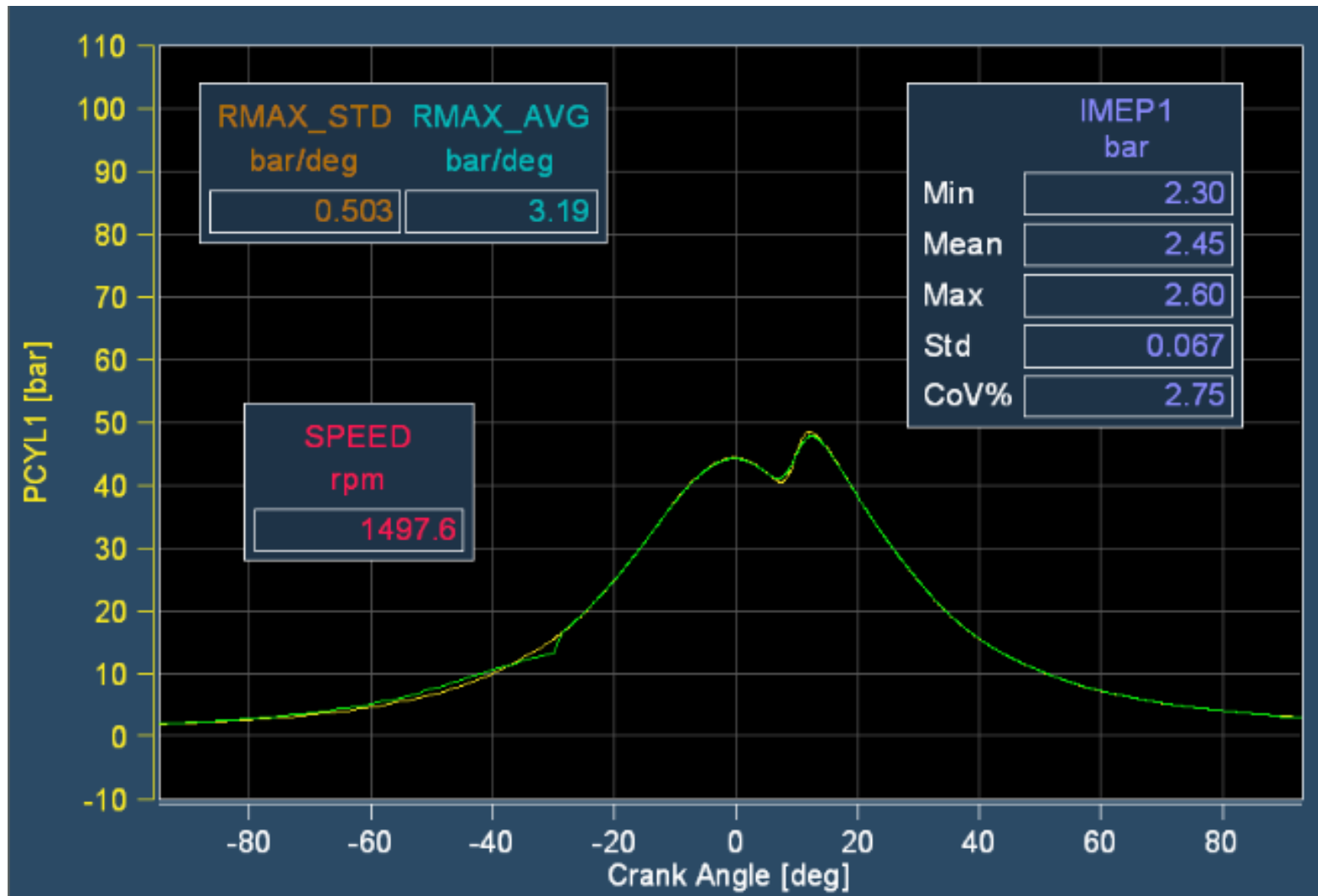


Figure C1 User Interface – In-Cylinder Pressure

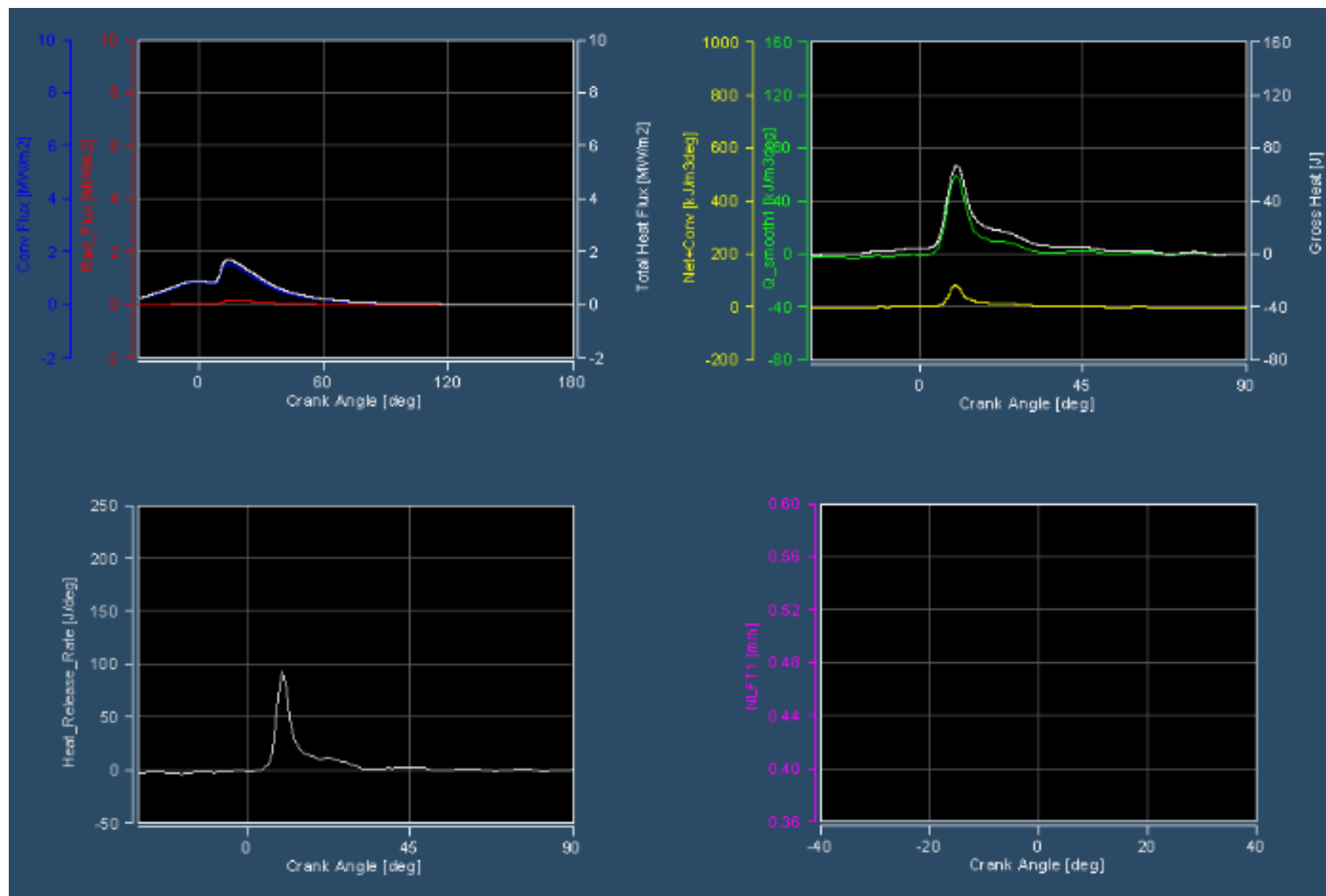
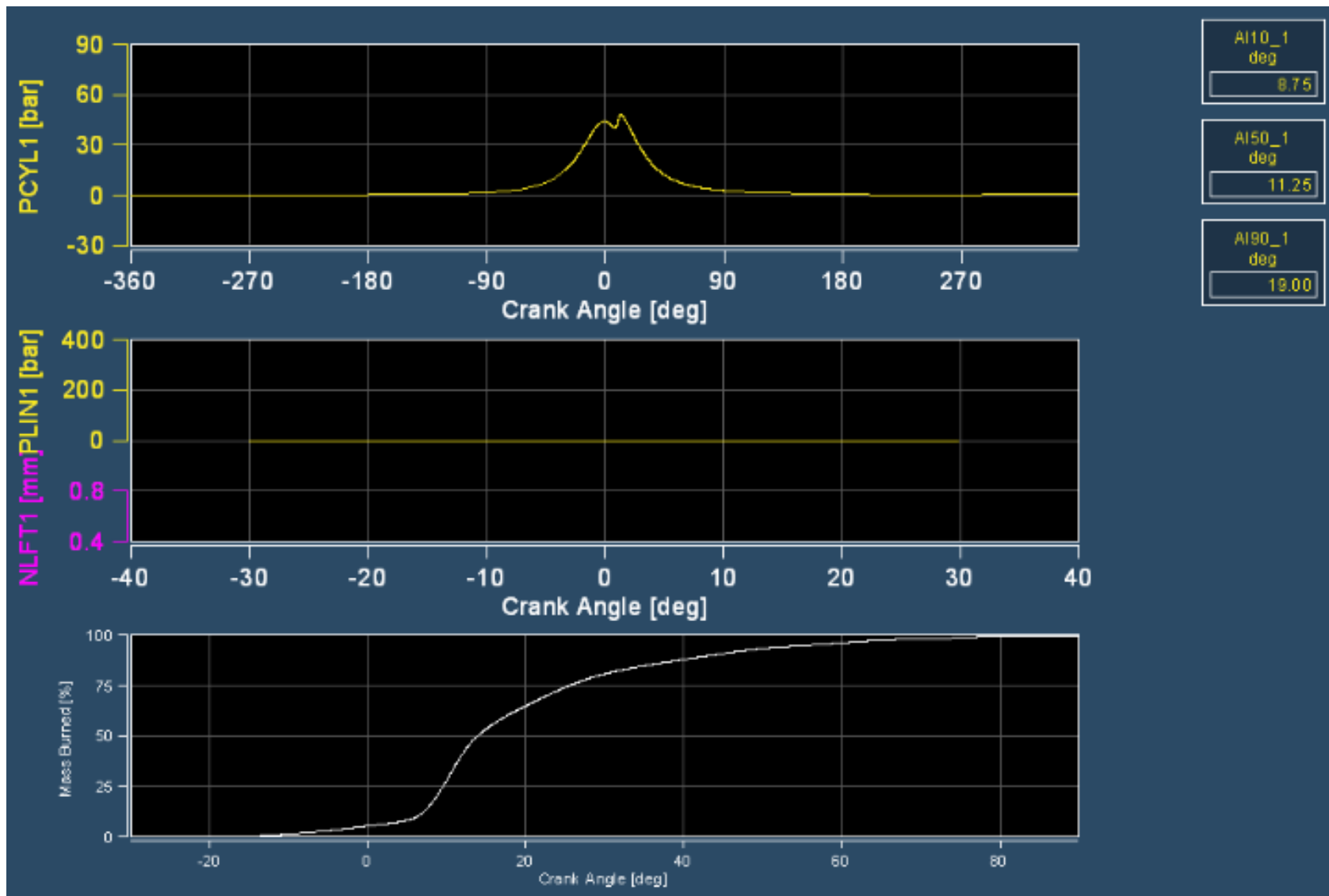


Figure C2 User Interface – Heat Flux and Heat Release



**Figure C3** User Interface – Pressure and Mass Burnt

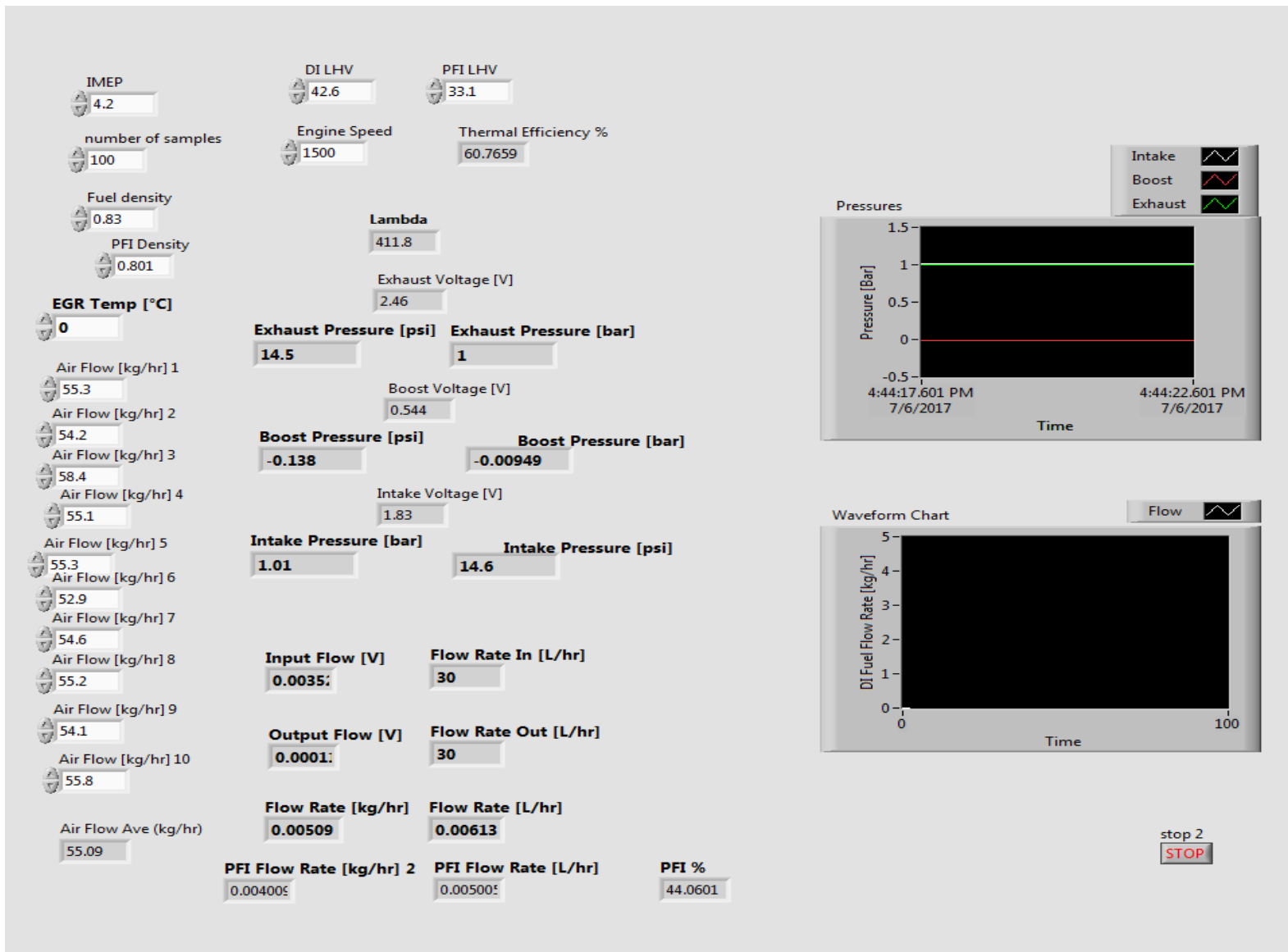
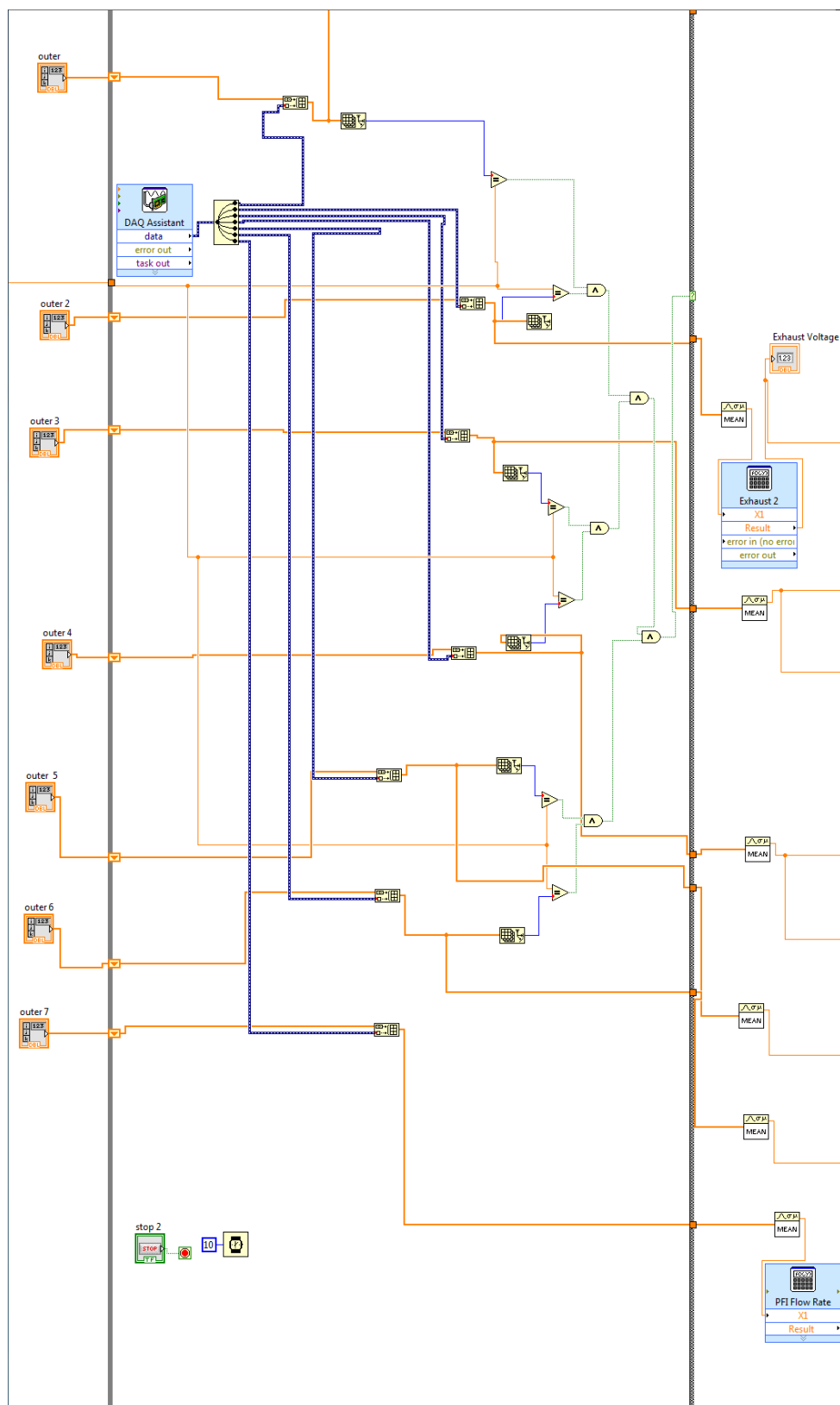
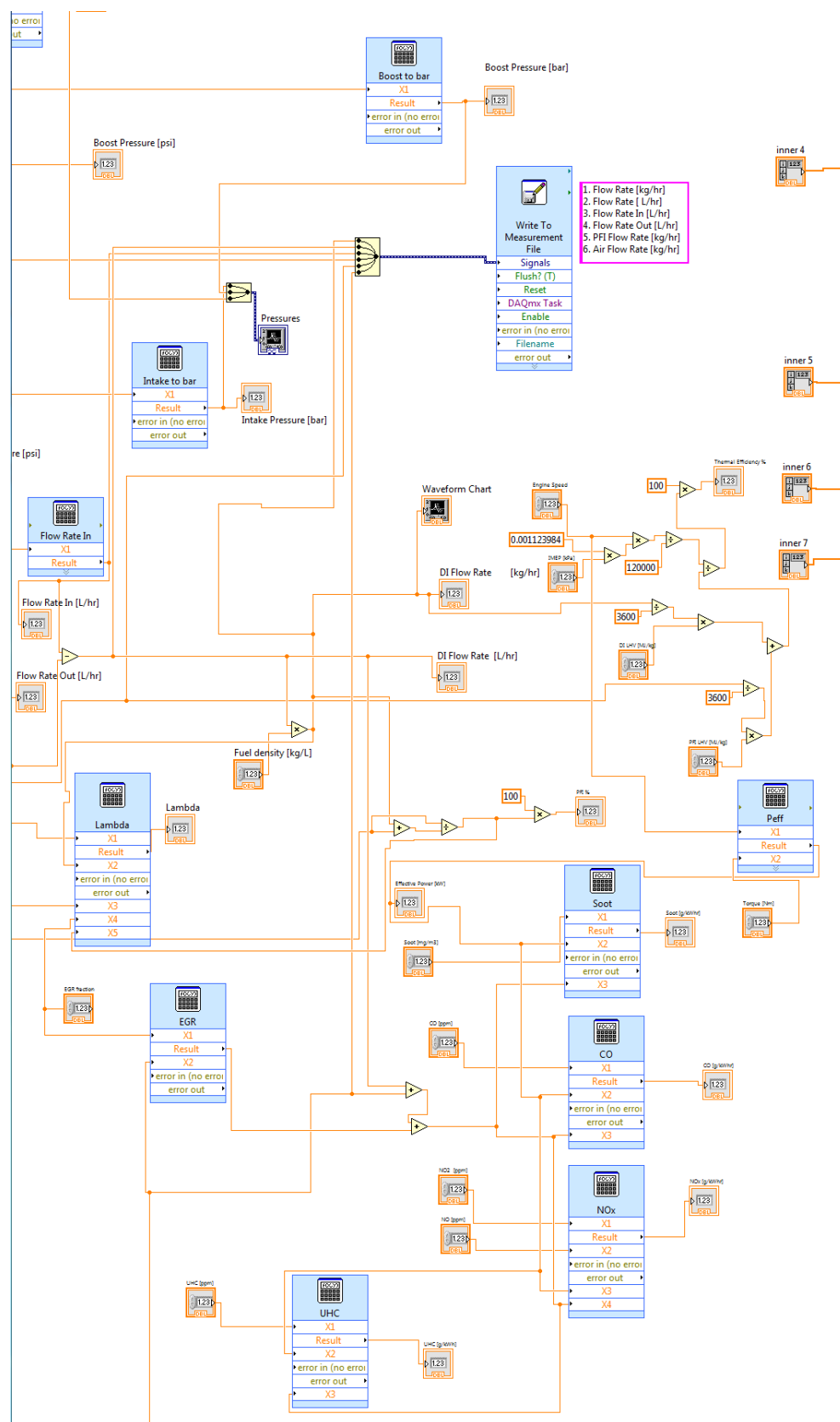


Figure C4 User Interface for Flow Rate Data Acquisition



**Figure C5** LabVIEW Block Diagram – Creating Data Arrays



**Figure C6** LabVIEW Block Diagram – Signal Conversion